




## Topological superconductivity induced by magnetic texture crystals

Daniel Steffensen <sup>1</sup>, Morten H. Christensen <sup>1,2</sup>, Brian M. Andersen,<sup>1</sup> and Panagiotis Kotetes <sup>3,1,\*</sup>

<sup>1</sup>*Niels Bohr Institute, University of Copenhagen, Jagtvej 128, DK-2200 Copenhagen, Denmark*

<sup>2</sup>*School of Physics and Astronomy, University of Minnesota, Minneapolis, Minnesota 55455, USA*

<sup>3</sup>*CAS Key Laboratory of Theoretical Physics, Institute of Theoretical Physics, Chinese Academy of Sciences, Beijing 100190, China*



(Received 7 January 2021; revised 23 December 2021; accepted 16 February 2022; published 24 March 2022)

We present a detailed investigation of the topological phases and Majorana fermion (MF) excitations that arise from the bulk interplay between (un)conventional one- and two-band spin-singlet superconductivity and a number of magnetic texture crystals. The latter define inhomogeneous magnetization profiles which consist of a periodically repeating primitive cell. Here we focus on magnetic texture crystals with a primitive cell of the helix, whirl, and skyrmion types, which feature distinct symmetry properties. We identify a multitude of accessible topological phases which harbor flat, unidirectional, bidirectional, (quasi)helical, or chiral MF edge modes. This rich variety originates from the interplay between topological phases with gapped and nodal bulk energy spectra. The types of the emerging topological superconducting phases and the features of the arising MFs are solely determined by the properties and compatibility of the so-called magnetic and pairing point and space groups. Our analysis is general and does not rely on specific parameters of the models employed here to exemplify the topological scenarios which become accessible. Therefore, our results can be extended to systems with multiple bands, are relevant for a wide range of layered materials and hybrid devices, and provide predictions for strong, weak, and crystalline topological phases.

DOI: [10.1103/PhysRevResearch.4.013225](https://doi.org/10.1103/PhysRevResearch.4.013225)

### I. INTRODUCTION

Since its discovery, superconductivity has served as an inspiration for countless new concepts and applications. A recent development in the field concerns the material discovery and synthetic engineering of topological superconductors (TSCs) [1–13], which harbor charge-neutral Majorana fermion (MF) quasiparticles [14–25]. Remarkably, zero-dimensional (0D) defects can trap zero-energy MFs [21–25], i.e., the so-called Majorana zero modes (MZMs), which adhere to non-Abelian exchange statistics [18,26–28] and open perspectives for cutting-edge quantum manipulations [26–34]. MZMs are sought after in a variety of systems, such as those containing singular defects, e.g., vortices [16–18,20,35–44], disclinations [45,46], hedgehogs [47], and nonsingular defects unfolding in one direction, e.g., termination edges [19,45,46,48], domain walls [20,36], and isolated magnetic skyrmions [49–54].

In the majority of the most prominent engineered quasi-one-dimensional (quasi-1D) TSCs, where fingerprints of MZMs appear to have been experimentally recorded [55–74], the presence of an inversion-symmetry-breaking (ISB) spin-orbit coupling (SOC) is crucial. Its role is to split the initially

degenerate spin bands, with the only remaining degeneracies surviving at inversion-symmetric points (ISPs)  $k_{\mathcal{I}}$ , which satisfy  $k_{\mathcal{I}} \equiv -k_{\mathcal{I}}$ . In superconductor-semiconductor nanowires [75–77] and collinear magnetic chains [58,78–81], the additional presence of a Zeeman or exchange field lifts the residual Kramers degeneracies, as sketched in Figs. 1(a)–1(d). The inclusion of spin-singlet pairing gaps out the remnant Fermi surface (FS) and compensates the magnetic gaps at  $k_{\mathcal{I}}$ , thus effecting the transition to a topological superconducting phase.

However, there are still a large number of proposals for engineered quasi-1D TSCs which instead rely on a synthetic SOC, which is either induced by a magnetic texture [82–102], or alternatively, by antiferromagnetism [103] or ferromagnetism [104] in the presence of currents and external or stray Zeeman fields. When it comes to magnetic textures, a magnetic helix crystal (MHC) is the minimal profile that can induce topological superconductivity since it simultaneously generates the required ISB SOC and the perpendicular exchange field mentioned above [105]. This is sketched in Figs. 1(e)–1(h). While a MHC is sufficient to guarantee the occurrence of topological superconductivity in 1D, engineering strong TSCs with a fully gapped bulk energy spectrum in  $d > 1$  dimensions requires a magnetic profile which winds in all  $d$  directions. Thus, while a MHC leads to spinless  $p$ -wave pairing in 1D, a spin skyrmion crystal (SSC) phase is necessary to generate an effective spinless chiral  $p + ip$  TSC in 2D [87]. Remarkably, the key role of magnetic textures in TSCs has been recently highlighted by the experimental observations of Refs. [69,72,106–108] where textures were shown to be pivotal for stabilizing topological

\*kotetes@itp.ac.cn

Published by the American Physical Society under the terms of the [Creative Commons Attribution 4.0 International license](https://creativecommons.org/licenses/by/4.0/). Further distribution of this work must maintain attribution to the author(s) and the published article's title, journal citation, and DOI.

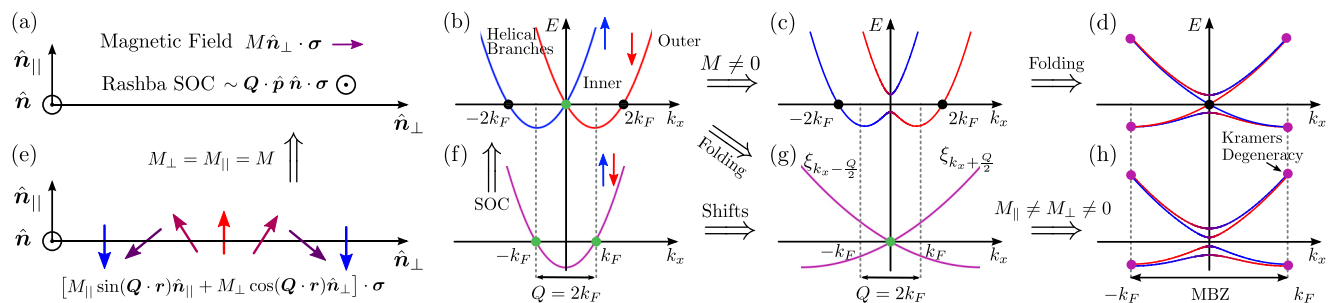


FIG. 1. (a)–(d) Standard mechanism to achieve 1D topological superconducting phases, which relies on Rashba-type spin-orbit coupling (SOC). (e)–(f) Reconstruction of the bulk spectrum of a spin-degenerate electron gas due to a magnetic helix crystal (MHC) which possesses a spatially varying magnetic moment for  $M_{\parallel} \neq M_{\perp}$ . (a) Schematic illustration of ISB SOC pointing in the  $\hat{n} = \hat{n}_{\perp} \times \hat{n}_{\parallel}$  spin direction, in the presence of a homogeneous magnetic field pointing in the  $\hat{n}_{\perp}$  direction. (b) Spin-split bands of an electron gas in the absence of a Zeeman and exchange field, resulting in a degeneracy at the ISP  $k_{\mathcal{I}} = 0$ . (c) The combination of SOC and a Zeeman and exchange field perpendicular to it lifts all spin degeneracies in (b). (d) Equivalent description of (c) after downfolding to the magnetic Brillouin zone (MBZ) of (e), where we depict the profile of a MHC with wave vector  $\mathbf{Q} = Q\hat{n}_{\perp}$ , winding in the plane spanned by  $\hat{n}_{\parallel}$  and  $\hat{n}_{\perp}$ . Note that (a) and (e) map to each other for  $M_{\parallel} = M_{\perp}$ . (f) Shows the two Fermi points which become magnetically scattered in the presence of the MHC. Here, the magnetic wave number  $Q$  coincides with the FS nesting wave number  $Q_N$ . (g) Equivalent description of (f) in the MBZ. (h) The MHC opens a full gap at the intersecting point in (g) [green dot in (g)]. In this work, we focus on topological superconducting phases induced by various magnetic textures in 1D and 2D, by means of mechanisms similar to the one described in (f)–(h).

superconductivity. This is also the case in Ref. [71], where the possible involvement of a skyrmion defect was invoked to explain the appearance of a pair of MZMs in topological magnetic-island heterostructures.

In this paper, we provide an in-depth exploration of the various 1D and 2D TSCs which emerge from the coexistence of (un)conventional one- and two-band spin-singlet superconductivity with a set of representative magnetic texture crystals. Our starting point is the synthetic SOC mechanism displayed in Figs. 1(f)–1(h), which opens the door to new and interesting topologically nontrivial phases. In fact, depending on the type of the texture and the strengths of the magnetic and superconducting gaps, we find either a fully gapped or a nodal bulk energy spectrum, which give rise to a diversity of MF edge modes. We present a comprehensive classification for each type of topological band structure, and account for both strong and weak topological superconducting phases, as well as possible strong topological crystalline phases stabilized by additional magnetic point- and space-group symmetries.

This work aims at setting a paradigmatic and general framework to study the topological properties arising from the interplay between magnetic texture crystals and spin-singlet superconductivity. Since our analysis relies on the symmetry properties of the magnetic and pairing terms, and not on particular details of the models employed for the concrete demonstration, it is applicable to a broad range of materials and hybrid devices, including platforms involving magnetic adatoms deposited on top of superconductors, alongside intrinsic TSCs that do not rely on ISB SOC. Our analysis naturally addresses topological superconducting phases in which magnetism and superconductivity are assumed to originate from the same electronic degrees of freedom. Such a scenario may be of direct relevance to iron-based superconductors (FeSCs), which feature coexistence of various magnetic phases and superconductivity [109–124]. Among the experimentally discovered phases, one is of yet-unresolved nature [122], and does not match with any of the three well-established commensurate magnetic phases

known to exist in FeSCs [125–133]. This commensurate framework was recently extended in Ref. [134] to include incommensurate magnetic texture crystals. Given the currently inconclusive status of the experimental observations, the phase discovered in Ref. [122] may as well be a magnetic texture crystal. This opens up new possibilities for topological superconducting phases in FeSCs, which are distinct to the ones that have so far been theoretically [40,41,43] and experimentally [135–139] explored.

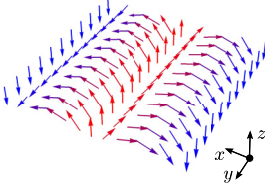
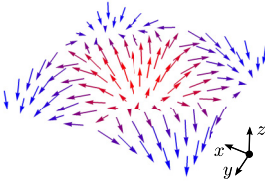
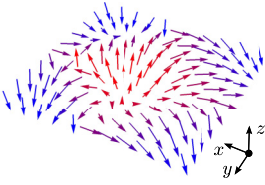
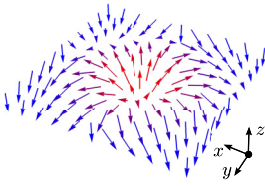
Motivated by the above, in the following we focus on the accessible TSCs in layered tetragonal itinerant magnets, which possess a  $D_{4h}$  point-group symmetry in the nonmagnetic normal phase. We also consider that spin transforms according to the spatial symmetry operations, and we restrict to a single Kramers doublet of the double covering  $D_{4h}$  group. We additionally assume that ISB SOC and spin anisotropies (cf. Ref. [132]) are negligible. Reference [134] has mapped out the types of single- and double- $Q$  textures that such magnets support, and we here focus on the single- $Q$  MHC and the fourfold-symmetric double- $Q$  spin whirl crystal (SWC<sub>4</sub>) profiles. We also consider the SWC<sub>4</sub> phase in the presence of an in- and out-of-plane Zeeman field,  $B_{\parallel}$  and  $B_{\perp}$ , leading to the here-termed SWCB<sub>2</sub> and SWCB<sub>4</sub> textures, respectively. Notably, for a range of  $B_{\perp}$  values, the SWCB<sub>4</sub> texture is equivalent to a fourfold-symmetry-preserving SSC phase [134], which we here denote SSC<sub>4</sub>. Table I provides an overview of these magnetic texture crystals.

## II. SUMMARY OF OUR TOPOLOGICAL CLASSIFICATION RESULTS

To perform the systematic topological classification of the various TSCs induced by the magnetic texture crystals presented in Table I, a number of aspects need to be taken into consideration in regards with the symmetry groups preserved by the magnetic and pairing terms.

A given magnetic texture crystal preserves the so-called magnetic point group  $M$ , which is here a group

TABLE I. Magnetic point- and space-group elements preserved for the different magnetic texture profiles studied in this work. These build upon the magnetic helix crystal (MHC) and the spin whirl crystal (SWC<sub>4</sub>) textures. The SWC<sub>4</sub> profile is also investigated in the presence of an in- (out-of-) plane Zeeman field  $B_{\parallel}$  ( $B_{\perp}$ ). Note that the SWC<sub>4</sub> texture with a nonzero  $B_{\perp}$  behaves as the spin skyrmion crystal (SSC<sub>4</sub>) texture in certain parameter-value regimes. Here  $\mathcal{T}$  represents the usual time-reversal operator, and  $\sigma_{xz}$  ( $\sigma_{yz}$ ) is the mirror operator in the  $xz$  ( $yz$ ) plane. The  $C_{4v}$  point group consists of the following five conjugacy classes:  $\{E\}$ ,  $\{C_2\}$ ,  $\{C_4, C_4^{-1}\}$ ,  $\{\sigma_v\}$ , and  $\{\sigma_d\}$ . Here,  $E$  denotes the identity element,  $C_n$  denotes a  $2\pi/n$  counterclockwise rotation of the system about the  $z$  axis, and  $\sigma_v$  ( $\sigma_d$ ) contain the mirrors  $\sigma_{xz,yz}$  ( $\sigma_{d_{\pm z}}$ ) with vertical mirror planes extending in the  $z$  direction and the main (diagonal  $d_{\pm}$  defined as  $x = \pm y$ ) in-plane axis, as denoted by the respective index. Space-group elements are denoted above using the Seitz notation, i.e.,  $\{g | \mathbf{t}\}$  where  $g$  is a point-group symmetry of  $D_{4h}$ , and  $\mathbf{t}$  is a translation by a fraction of the Bravais lattice vectors. Note that deviations from the above generally appear for multiband implementations of the magnetic texture crystal profiles. Examples of such situations are explored in detail in the main text.

Magnetic Texture	Spatial Profile $\mathbf{M}(\mathbf{r})/ \mathbf{M}(\mathbf{r}) $	Magnetic Point Group	Magnetic Space Group
Magnetic Helix Crystal (MHC) $\mathbf{M}(\mathbf{r}) = (M_{\parallel} \sin(Qx), 0, M_{\perp} \cos(Qx))$		$M_{\text{MHC}} = \{E, C_2, \sigma_{xz}\mathcal{T}, \sigma_{yz}\mathcal{T}\}$ $= C_2 + (C_{2v} - C_2)\mathcal{T}$	$\{\mathcal{T}   (\pi/Q, 0)\}$ $\{C_{2v} - C_2   (\pi/Q, 0)\}$
Spin Whirl Crystal (SWC <sub>4</sub> ) $\mathbf{M}(\mathbf{r}) = (M_{\parallel} \sin(Qx), 0, M_{\perp} \cos(Qx))$ $+ (0, M_{\parallel} \sin(Qy), M_{\perp} \cos(Qy))$		$M_{\text{SWC}_4} = \{E, C_4, C_4^{-1}, C_2,$ $\sigma_{xz}\mathcal{T}, \sigma_{yz}\mathcal{T}, \sigma_{d_{+z}}\mathcal{T}, \sigma_{d_{-z}}\mathcal{T}\}$ $= C_{4v} + (C_{4v} - C_4)\mathcal{T}$	$\{\mathcal{T}   (\pi/Q, \pi/Q)\}$ $\{C_{4v} - C_4   (\pi/Q, \pi/Q)\}$
Spin Whirl Crystal and Inplane $B$ Field (SWCB <sub>2</sub> ) $\mathbf{M}(\mathbf{r}) = (M_{\parallel} \sin(Qx), 0, M_{\perp} \cos(Qx))$ $+ (B_{\parallel}, M_{\parallel} \sin(Qy), M_{\perp} \cos(Qy))$		$M_{\text{SWCB}_2} = \{E, \sigma_{xz}\mathcal{T}\}$ $= C_1 + (D_1 - C_1)\mathcal{T}$	$\{\sigma_{yz}   (\pi/Q, \pi/Q)\}$
Spin Whirl Crystal and Out-of-Plane $B$ Field (SWCB <sub>4</sub> ) $\mathbf{M}(\mathbf{r}) = (M_{\parallel} \sin(Qx), 0, M_{\perp} \cos(Qx))$ $+ (0, M_{\parallel} \sin(Qy), M_{\perp} \cos(Qy) + B_{\perp})$		$M_{\text{SWC}_4} = \{E, C_4, C_4^{-1}, C_2,$ $\sigma_{xz}\mathcal{T}, \sigma_{yz}\mathcal{T}, \sigma_{d_{+z}}\mathcal{T}, \sigma_{d_{-z}}\mathcal{T}\}$ $= C_{4v} + (C_{4v} - C_4)\mathcal{T}$	—

related to the subgroups of the normal-phase symmetry group  $D_{4h}$ . The elements of  $M$  are generally obtained from products of the original double-point-group operations and time reversal  $\mathcal{T}$ . Products involving  $\mathcal{T}$  give rise to antiunitary mirror symmetries [140–143] which have nontrivial implications on the topological classification in high-symmetry planes (HSPs), and open the door to novel types of crystalline topological phases and MFs [144–156]. Further information about the symmetry properties of the various textures considered in this work is listed in Table I.

The classification in HSPs is also affected by magnetic space-group symmetries [88, 151, 157–164]. Here,  $\mathcal{T}$  or elements of the double  $D_{4h}$  point group are combined with translations which make the texture “slide” in the plane [165]. These constitute exact symmetries of the system only as long as the involved translation also constitutes a lattice translation, which takes place when the magnetic vector is commensurate. Nonetheless, in itinerant magnetic systems the invariance

under magnetic translations also emerges in an approximate manner for low energies since it is the Fermi wavelength rather than the lattice constant which sets the characteristic lengthscale that governs the properties of the system in that regime. In either situation, nonsymmorphic symmetries enrich the topological classification in bulk HSPs and at edges which preserve them.

The final crucial factor which influences the topological properties is the type of the pairing point group associated with the pairing gap. In this work, we assume (un)conventional one- and two-band spin-singlet pairing with possible symmetry-imposed or accidental nodes. Going beyond a single-band picture allows us to capture salient features of realistic band structures of correlated magnets, such as the FeSCs [166–173]. Moreover, depending on which irreducible representation (IR) of  $D_{4h}$  enters the pairing term  $\Delta_{\mathbf{k}}$ , i.e.,  $\{A_{1g}, B_{1g}, B_{2g}, A_{2g}\}$ , we generally find a different topological scenario in HSPs, since  $\Delta_{\mathbf{k}}$  may possess symmetry-enforced zeros in these.

Our main findings regarding the rich diversity of TSCs are collected in Tables II and III, for general and interband-only magnetic scattering, respectively. Two-dimensional (2D) systems in the presence of a MHC texture exhibit protected nodal points which lead to edge Majorana and Andreev flat bands (MFBs and AFBs). Bulk nodal points are also present when considering the  $SWC_4$  texture, but are not protected. As a result, edge MFBs and AFBs are not accessible. Nonetheless, a different type of MF edge modes arises, which we denote bidirectional (see also Ref. [162]) since they do not possess a fixed helicity or chirality, and depend strongly on the edge termination. These MF edge modes emerge due to mirror-symmetry-protected degeneracies at ISPs, or alternatively due to weak topological superconducting phases. The addition of a magnetic field can either render the bidirectional MF edge modes unidirectional [174–176], or open a bulk gap and mediate a transition to a chiral TSC, analogous to a  $p + ip$  superconductor. Remarkably, we find that the multiband character of the systems considered here not only allows for a more realistic description, but also results in unique topological superconducting phases and MF edge modes. In particular, we show that two-band systems under the influence of multiband magnetic textures harbor Kramers (mirror-symmetry-protected) pairs of (quasi)helical MF edge modes, although time-reversal (TR) symmetry is broken. In fact, these pairs of MFs constitute topologically protected Andreev zero modes (AZMs) in 1D [177–180]. While AZMs have been poorly explored, their topological nature also renders them prominent candidates for quantum computing applications [181,182].

At this point, it appears vital to underline the various features of this work in comparison to a number of previous studies concerning TSCs from MHCs in 1D and 2D (cf. Refs. [83,84,86,88–96,98,101]), as well as TSCs stemming from the coupling of a conventional spin-singlet superconductor to a  $SSC_4$  magnet [87,93,99,100]. Regarding the investigation of topological properties, the above studies proceeded along two different paths. Either by numerically evaluating a topological invariant or by considering special cases of magnetic texture crystals described by a magnetization of a spatially constant modulus, in which cases, the spatial dependence can be fully or approximately removed by appropriate  $SU(2)$  rotations [105]. In stark contrast, here we adopt a methodology that addresses the general case where the magnetic textures possess a spatially varying modulus. For the purposes of demonstration, and with no loss of generality, we restrict to crystals which lead to a small number of bands after the reconstruction of the band structure. Importantly, this formalism also reveals how to construct low-energy models which facilitate the analytical evaluation of the topological invariants. This aids in the description of the topological properties of the system in spite of the added complexity introduced by the superlattice formation. Moreover, our work is not restricted to the study of the MHC and  $SSC_4$  textures, but further includes the investigation of the  $SWC_4$ , which together with the MHC have been shown to constitute global minima of a general Landau functional describing incommensurate magnetism in itinerant magnets [134]. The topological properties of the  $SWC_4$  texture are also analyzed in the presence of

additional Zeeman and exchange fields, thus also connecting to the  $SSC_4$  phase.

Our work provides a complete description of the topological properties of these systems, by means of a classification which accounts for strong, weak, and crystalline phases. Notably, our analysis also considers the possibility of unconventional pairing terms. We demonstrate how the interplay of the magnetic and pairing groups shapes the topological properties of these systems and gives rise to a multitude of MF excitations, with several of these not having been previously discussed in this context. Hence, our work naturally involves the construction of a number of topological invariants which have not been previously discussed for TSCs originating from magnetic texture crystals. In fact, we reveal that a number of these topological invariants are responsible for the quantization of physical quantities, such as the bulk staggered magnetization, which can be harnessed to experimentally infer the topological phase of the systems in question. In contrast to previous works, that are primarily focused on single-band systems, our work discusses two-band scenarios which open the door to engineering topologically protected Andreev zero and edge modes, as well as Kramers pairs of Majorana solutions. The latter is a notable result, given the fact that the magnetic texture crystal violates the standard time-reversal symmetry.

The remainder of this paper is organized as follows. In Sec. III we describe the modeling assumptions that we use throughout this work. In Sec. IV, we investigate TSCs in 1D systems induced by a MHC. In Sec. V we extend our study to 2D, and explore the full variety of possible TSCs and protected MF edge modes induced by the  $SWC_4$  phase. The experimental implementation of the various topological scenarios of interest is examined in Sec. VI. There, we elaborate on the interplay of magnetic texture crystals and spin-singlet superconductivity, and enumerate prominent platforms that provide fertile ground for their viable coexistence. Section VII presents our conclusions and outlook. Lastly, Appendixes A–D contain various definitions, further technical details, and complementary numerical calculations.

### III. MODELING CONSIDERATIONS

Before proceeding, we specify the modeling assumptions employed in the upcoming analysis. While our analytical and numerical investigations also aim at predicting possible topological phases relevant to unconventional superconductors, we here treat these cases only in a qualitative fashion. Correlated systems generally exhibit complex band structures, which is an aspect that hinders a transparent discussion of the topological properties as pursued here. For example, an accurate description of the FeSCs typically requires 5- or 10-band models [169,170]. Therefore, in order to ensure a balance between analytical tractability and faithful modeling, we focus on simplified one- and two-band models<sup>1</sup> which exhibit hole and electron pockets, as well as FS nesting. These

<sup>1</sup>Note that each one of the band dispersions employed in the upcoming models is chosen to be independently invariant under all the  $D_{4h}$  point-group operations.

TABLE II. Summarizing table of the broad variety of 2D topological superconducting phases induced by a magnetic helix crystal (MHC), a fourfold-symmetric spin whirl crystal (SWC<sub>4</sub>), and a SWC<sub>4</sub> in the presence of in- and out-of-plane Zeeman field (SWCB<sub>2</sub> and SWCB<sub>4</sub>). The present table holds for magnetic textures where both intraband and interband contributions are generally present. For each texture we display the respective magnetic Brillouin zone (MBZ), the relevant high-symmetry planes (HSPs), and the arising symmetry-protected degeneracies induced by the given magnetic point group (see Table I). Furthermore, we also list the symmetry classification for the full MBZ and the HSPs, the relevant topological invariants, and the resulting type of Majorana and Andreev edge states. We arrive at three distinct types of invariants which become nontrivial. For a gapless energy spectrum these consist of the vorticities  $\nu/\nu$  of the arising nodes, while for a fully gapped energy spectrum, we find the winding number  $w$ , the Majorana number  $\mathcal{M}$ , and the first Chern number  $\mathcal{C}_1$ . Each invariant is in addition labeled as strong, weak, mirror, or glide, depending on its type. Note that the classification in HSPs presents all the possible topological scenarios obtained by assuming the presence of only a single-crystalline symmetry at a time. We further elaborate on these in the proceeding sections. The table also includes the HSP classification in the presence of a pairing function  $\Delta_{\mathbf{k}}$  transforming as one of the irreducible representations (IRs)  $\{A_{1g}, B_{1g}, B_{2g}, A_{2g}\}$  of the group  $D_{4h}$ . Depending on the IR of  $\Delta_{\mathbf{k}}$ , the classification in HSPs splits into two branches, depending on whether  $\Delta_{\mathbf{k}}$  is even or odd under the original  $D_{4h}$  mirror operation defined for the HSP of interest. In the former case ( $\mathcal{Q} = \mathbb{1}_\tau$ ),  $\Delta_{\mathbf{k}}$  remains invariant under the original mirror operation, while in the latter ( $\mathcal{Q} = \tau_3$ ),  $\Delta_{\mathbf{k}}$  is invariant under the mirror operation combined with a rotation in Nambu space, which is spanned by the unit  $\mathbb{1}_\tau$  and Pauli  $\tau$  matrices. Finally, the red and blue color coding is adopted throughout the text, and reflects the spin-up and -down orientation of the  $z$  component of the electronic spin polarization stemming from the mode appearing on the corresponding left (L) and right (R) edge, when a termination is considered. Left (right) edge modes are shown above with solid (dashed) lines.

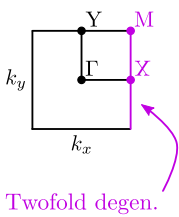
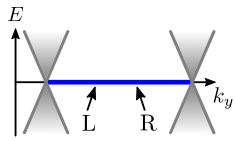
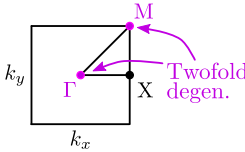
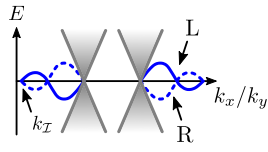
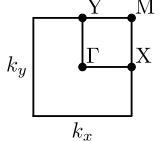
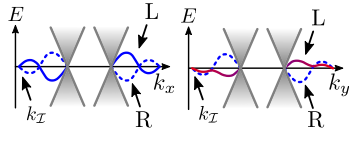
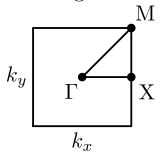
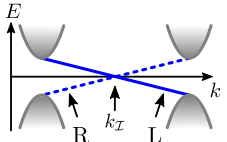
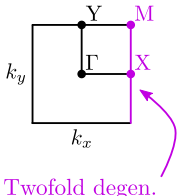
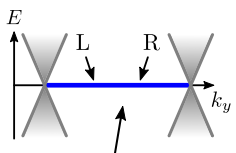
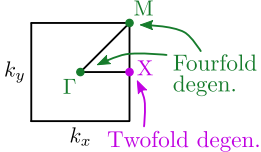
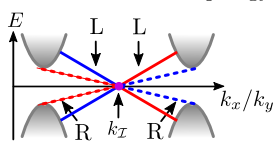
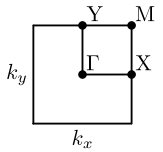
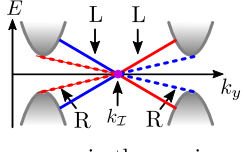
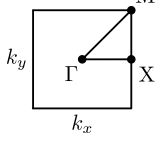
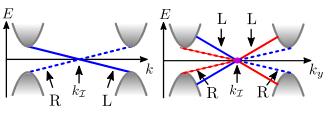
Magnetic Texture Properties	Topological Classification	Invariants Nodal Bulk	Invariants Fully-Gapped	Resulting Edge States
<p><u>MHC</u>                      MBZ: <math>\mathbf{k} \in (-q, q] \times (-\pi, \pi]</math>                      Protected degen.: XM</p> 	<ul style="list-style-type: none"> <li>Full MBZ: BDI</li> <li><math>\mathcal{Q} = \mathbb{1}_\tau (\tau_3)</math></li> <li><math>\Gamma Y</math>: BDI <math>\oplus</math> BDI or AI <math>\oplus</math> AI (BDI <math>\oplus</math> BDI)</li> <li>XM: AIII <math>\oplus</math> AIII or AI <math>\oplus</math> AI (AIII <math>\oplus</math> AIII or BDI <math>\oplus</math> BDI)</li> <li><math>\Gamma X</math> and YM: BDI (AI <math>\oplus</math> AI)</li> </ul>	<p>Strong: <math>\nu \in \mathbb{Z}</math></p> <p>Weak: <math>w_{k_{x,y}} \in \mathbb{Z}</math></p> <p>Mirror: <math>\nu_{k_x=0} \in \mathbb{Z}</math></p> <p>Mirror: <math>\nu_{k_x=q} \in \mathbb{Z}</math></p> <p>(Mirror: <math>\nu_{k_y=0,\pi} \in \mathbb{Z}</math>)</p>	<p>Weak: <math>w_{k_{x,y}} \in \mathbb{Z}</math></p> <p>Glide: <math>w_{G,k_x=0} \in \mathbb{Z}</math></p> <p>(Mirror/Glide: <math>w_{M/G,k_x=0} \in \mathbb{Z}</math>)</p> <p>Glide: <math>w_{G,k_x=q} \in \mathbb{Z}</math></p> <p>(Mirror/Glide: <math>w_{M/G,k_x=q} \in \mathbb{Z}</math>)</p>	<p>Majorana/Andreev Flat Bands</p> 
<p><u>SWC<sub>4</sub></u>                      MBZ: <math>\mathbf{k} \in (-q, q] \times (-q, q]</math>                      Protected degen.: <math>\Gamma</math> &amp; M</p> 	<ul style="list-style-type: none"> <li>Full MBZ: D</li> <li><math>\mathcal{Q} = \mathbb{1}_\tau (\tau_3)</math></li> <li><math>\Gamma X</math>, XM &amp; MF: BDI (BDI)</li> </ul>	<p>Weak: <math>\mathcal{M}_{k_{x,y}=q} \in \mathbb{Z}_2</math></p>	<p>Strong: <math>\mathcal{C}_1 \in \mathbb{Z}</math></p> <p>Weak: <math>\mathcal{M}_{k_{x,y}=q} \in \mathbb{Z}_2</math></p> <p>Mirror: <math>\tilde{w}_{M,HSP} \in \mathbb{Z}</math></p> <p>(Mirror: <math>\tilde{w}_{M,HSP} \in \mathbb{Z}</math>)</p>	<p>Bidirectional Majorana Modes</p> 
<p><u>SWCB<sub>2</sub></u> (<math>B_{  }\sigma_x</math>)                      MBZ: <math>\mathbf{k} \in (-q, q] \times (-q, q]</math>                      Protected degen.: -</p> 	<ul style="list-style-type: none"> <li>Full MBZ: D</li> <li><math>\mathcal{Q} = \mathbb{1}_\tau (\tau_3)</math></li> <li><math>\Gamma X</math> &amp; YM: BDI (BDI)</li> </ul>	<p>Weak: <math>\mathcal{M}_{k_{x,y}=q} \in \mathbb{Z}_2</math></p>	<p>Weak: <math>\mathcal{M}_{k_{x,y}=q} \in \mathbb{Z}_2</math></p> <p>Mirror: <math>\tilde{w}_{M,HSP} \in \mathbb{Z}</math></p> <p>(Mirror: <math>\tilde{w}_{M,HSP} \in \mathbb{Z}</math>)</p>	<p>Bi- or Uni-directional Majorana Modes</p> 
<p><u>SWCB<sub>4</sub></u>                      MBZ: <math>\mathbf{k} \in (-q, q] \times (-q, q]</math>                      Protected degen.: -</p> 	<ul style="list-style-type: none"> <li>Full MBZ: D</li> <li><math>\mathcal{Q} = \mathbb{1}_\tau (\tau_3)</math></li> <li><math>\Gamma X</math>, XM &amp; MF: BDI (BDI)</li> </ul>	<p>Weak: <math>\mathcal{M}_{k_{x,y}=q} \in \mathbb{Z}_2</math></p>	<p>Strong: <math>\mathcal{C}_1 \in \mathbb{Z}</math></p> <p>Weak: <math>\mathcal{M}_{k_{x,y}=q} \in \mathbb{Z}_2</math></p> <p>Mirror: <math>\tilde{w}_{M,HSP} \in \mathbb{Z}</math></p> <p>(Mirror: <math>\tilde{w}_{M,HSP} \in \mathbb{Z}</math>)</p>	<p>Chiral Majorana Modes</p> 

TABLE III. Summarizing table of the accessible topological phases induced by interband-only magnetic textures. As in Table II, also here we list the topological symmetry classification in the full MBZ and in HSPs, the relevant topological invariants and the resulting edge states, for all four magnetic textures of interest. As in the preceding table, the above classification is performed for a pairing function  $\Delta_{\mathbf{k}}$  transforming according to one of the  $\{A_{1g}, B_{1g}, B_{2g}, A_{2g}\} D_{4h}$  IRs. Note that the topological invariants in the MHC case are identical for the two AIII blocks. Hence, we only enlist the invariants for a single AIII block.

Magnetic Texture Properties	Topological Classification	Invariants Nodal Bulk	Invariants Fully-Gapped	Resulting Edge States
<p><u>MHC</u>                      MBZ: <math>\mathbf{k} \in (-q, q] \times (-\pi, \pi]</math>                      Protected degen.: XM</p> 	<ul style="list-style-type: none"> <li>Full MBZ: AIII <math>\oplus</math> AIII</li> <li>Strong: <math>v \in \mathbb{Z}</math></li> <li>Weak: <math>w_{k_x, y} \in \mathbb{Z}</math></li> </ul> <p><math>Q = \mathbb{1}_\tau (\tau_3)</math></p> <ul style="list-style-type: none"> <li><math>\Gamma Y</math> &amp; XM: CI <math>\oplus</math> CI or <math>\oplus_4</math> AIII (BDI <math>\oplus</math> BDI or <math>\oplus_4</math> AIII)</li> <li><math>\Gamma X</math> &amp; YM: AIII <math>\oplus</math> AIII (<math>\oplus_4</math> AIII)</li> </ul>	<p>–</p> <p>Weak: <math>w_{k_x, y} \in \mathbb{Z}</math></p> <p>(Mirror: <math>\tilde{w}_{M, \text{HSP}} \in \mathbb{Z}</math>)                      (Glide: <math>w_{G, k_x=0, q} \in \mathbb{Z}</math>)</p> <p>–</p> <p>(Mirror: <math>w_{M, k_y=0, \pi} \in \mathbb{Z}</math>)</p>	<p>Andreev/Majorana Flat Bands</p>  <p>Majorana Flat Bands:                      Twofold Degeneracy per Edge</p>	
<p><u>SWC<sub>4</sub></u>                      MBZ: <math>\mathbf{k} \in (-q, q] \times (-q, q]</math>                      Protected degen.: <math>\Gamma, X</math> &amp; M</p> 	<ul style="list-style-type: none"> <li>Full MBZ: DIII</li> </ul> <p><math>Q = \mathbb{1}_\tau (\tau_3)</math></p> <ul style="list-style-type: none"> <li><math>\Gamma X, XM</math> &amp; MF: AIII <math>\oplus</math> AIII (D <math>\oplus</math> D)</li> </ul>	<p>–</p> <p>Strong: <math>\mathcal{M}^{\text{KP}} \in \mathbb{Z}_2</math></p> <p>Weak: <math>\mathcal{M}_{k_x, y=q}^{\text{KP}} \in \mathbb{Z}_2</math></p> <p>–</p> <p>Mirror: <math>w_{M, \text{HSP}} \in \mathbb{Z}</math>                      (Mirror: <math>\mathcal{M}_{M, \text{HSP}} \in \mathbb{Z}_2</math>)</p>	<p>Quasi-Helical Majorana Modes from Weak or Mirror Topology</p>  <p>Helical Majorana Modes only for Broken C<sub>4</sub> Symmetry</p>	
<p><u>SWCB<sub>2</sub></u> (<math>B_{  \sigma_x}</math>)                      MBZ: <math>\mathbf{k} \in (-q, q] \times (-q, q]</math>                      Protected degen.: –</p> 	<ul style="list-style-type: none"> <li>Full MBZ: D</li> </ul> <p><math>Q = \mathbb{1}_\tau (\tau_3)</math></p> <ul style="list-style-type: none"> <li><math>\Gamma X</math> &amp; YM: BDI (BDI)</li> </ul>	<p>–</p> <p>Weak: <math>\mathcal{M}_{k_x, y=q} \in \mathbb{Z}_2</math></p> <p>–</p> <p>Mirror: <math>\tilde{w}_{M, \text{HSP}} \in \mathbb{Z}</math>                      (Mirror: <math>\tilde{w}_{M, \text{HSP}} \in \mathbb{Z}</math>)</p>	<p>Quasi-Helical Majorana Modes from Weak or Mirror Topology</p>  <p>A gap opens in the x-axis modes</p>	
<p><u>SWCB<sub>4</sub></u>                      MBZ: <math>\mathbf{k} \in (-q, q] \times (-q, q]</math>                      Protected degen.: –</p> 	<ul style="list-style-type: none"> <li>Full MBZ: D</li> </ul> <p><math>Q = \mathbb{1}_\tau (\tau_3)</math></p> <ul style="list-style-type: none"> <li><math>\Gamma X, XM</math> &amp; MF: BDI (BDI)</li> </ul>	<p>–</p> <p>Weak: <math>\mathcal{M}_{k_x, y=q} \in \mathbb{Z}_2</math></p> <p>–</p> <p>Mirror: <math>\tilde{w}_{M, \text{HSP}} \in \mathbb{Z}</math>                      (Mirror: <math>\tilde{w}_{M, \text{HSP}} \in \mathbb{Z}</math>)</p>	<p>Chiral/Quasi-Helical Majorana Modes from Strong/Weak or Mirror Topology</p> 	

features are similar to those exhibited by some FeSCs (see also Fig. 2). The one-band (two-band) models are particularly suitable for exploring topological properties arising from intrapocket (interpocket) nesting.

Another aspect of realistic systems that needs to be accounted for is the fact that the magnetic wave vectors may be incommensurate or exhibit a high-order degree of commensurability. As a result, such cases require an infinite or very large number of bands for an accurate description after downfolding to the magnetic Brillouin zone (MBZ). To avoid such a complication, we consider commensurate magnetic

wave vectors  $\mathbf{Q}_{1,2}$ , with the property  $\mathbf{k} + 4\mathbf{Q}_{1,2} \equiv \mathbf{k}$ . More precisely,  $\mathbf{Q}_1 = Q\hat{x}$  with  $Q = -3\pi/2 \equiv \pi/2$ , with the lattice constant set to unity throughout, and  $\mathbf{Q}_2 = Q\hat{y}$  since the latter is obtained via a counterclockwise fourfold rotation of  $\mathbf{Q}_1$ . In most cases we consider that the magnetic wave vectors coincide with the FS nesting wave vectors  $\mathbf{Q}_{N,1}$  and  $\mathbf{Q}_{N,2}$  (see Fig. 2), which is a realistic assumption within an itinerant picture of magnetism which is also of interest in this work.

We note that our choice of  $Q$  does not affect the generality of the qualitative conclusions regarding the topological features of the systems under discussion, as the above wave

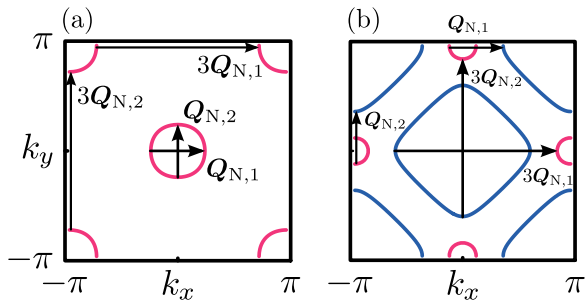


FIG. 2. One-band (a) and two-band (b) Fermi surfaces studied here. In (a) the two pockets possess the same character, while in (b) the pockets centered at the  $\Gamma$  and M (X and Y) points are of the hole (electron) type. The chosen electron- and hole characters for the pockets in (a) and (b) allow a qualitative connection with the band structures of certain FeSCs [169,170]. Note that the results presented in Tables II and III are not particular to the example band structures of (a) and (b), but hold generally for systems which share common magnetic and pairing point and space groups. The precise details of the band structures mainly influence the quantitative details of the topological phase diagrams, but not the accessible phases. Moreover, our results for the two-band model and the general mechanisms underlying the TSC phases can be directly generalized to system with more bands.

vectors can be adiabatically connected to incommensurate ones. This is achieved by only deforming the FS of the system without modifying its topology, i.e., assuming that neither Lifshitz [183,184] nor metal-to-insulator transitions [185] occur during this process. In fact, the analytical tractability which is ensured in this manner allows for a deeper and transparent understanding of the underlying mechanisms. Our conclusions thus serve as a basis for the study of more realistic multiband magnetic superconductors.

Furthermore, we point out that the upcoming analysis is not self-consistent with respect to the magnetic and superconducting order parameters. While our starting point partly builds upon the results of Ref. [134], which have been derived using microscopic models, we do not examine the fate of the textured magnetic order and its interplay with superconductivity in full detail. This work has a more explorative character and, thus, we allow for our search to be unconstrained in order to identify the most prominent routes for achieving TSCs. Section VI contains a detailed discussion of prominent routes and systems to realize the various topological phenomena investigated in this work.

We also wish to stress that the crystalline topological properties induced by the magnetic point- and space-group symmetries only give rise to topologically protected modes at boundaries which preserve the symmetries in question. This is in stark contrast to strong topological phases, for which the bulk-edge correspondence enforces the edge states to appear for a boundary of an arbitrary direction. For this reason, in the upcoming sections we first carry out the classification of the strong TSC phases, and subsequently discuss the possible crystalline ones which result from the magnetic point- and space-group symmetries. On the other hand, weak TSCs are distinct to both crystalline and strong phases. Weak TSCs can be viewed as a network of strong TSCs in one spatial

dimension lower. For instance, 2D weak topological phases emerge as a collection of strong 1D TSCs oriented along a given axis. Consequently, such weak 2D TSCs do not give rise to topologically protected modes along edges which are parallel to the characteristic axis determined by the constituent strong 1D TSCs. However, topologically protected modes appear for any other edge orientation, and the characteristics of the edge-mode dispersions vary depending on the orientation of the edge.

To this end, we clarify that the results of Tables II and III are not only applicable to the specific magnetic texture crystals depicted in Table I. Instead, these also hold for any other magnetic texture crystal combined with a pairing term which belongs to the point and space groups which are studied in this work. Even more, our results do not rely on any particular details of the underlying band dispersions, but only on the general assumption that these preserve  $\mathcal{T}$  and each band is individually invariant under the point- and space-group operations governing the normal phase (see also Footnote 1).

Concluding this section, we wish to emphasize that we have confirmed the validity of all the analytical results presented in the upcoming sections by means of numerical investigations of the respective lattice models in 1D and 2D, with open boundary conditions, and observed the predicted edge states.

#### IV. 1D TOPOLOGICAL SUPERCONDUCTORS

In the following analysis we first explore possible topological phases in 1D. Apart from being simple to investigate, the 1D case sets the stage and the formalism employed in the study of 2D systems, which is the main goal of this work. In 1D we consider the topological effects arising from the coexistence of either a conventional or an unconventional superconducting pairing with a MHC phase with either a constant or a spatially varying magnitude of the magnetic moment.

##### A. One-band models

We begin our study with one-band models (1BMs), which are defined on a lattice and describe electrons with a band dispersion  $\xi_{k_x}$  set by the hopping matrix elements  $t_{nm}$ . After including the chemical potential  $\mu$ , we have

$$H_0 = - \sum_{n,m} \psi_n^\dagger (t_{nm} + \mu \delta_{nm}) \mathbb{1}_\sigma \psi_m, \quad (1)$$

where the integers  $n, m$  label the positions  $R_{n,m}$  on the direct lattice, and  $\psi_n = (\psi_{n\uparrow}, \psi_{n\downarrow})^\top$ , with  $\top$  denoting transposition. The operator  $\psi_{n\sigma}$  ( $\psi_{n\sigma}^\dagger$ ) annihilates (creates) an electron with spin projection  $\sigma = \uparrow, \downarrow$  at the lattice site  $R_n$ . The magnetic part of the Hamiltonian describes a MHC texture winding in the  $xz$  spin plane:

$$H_{\text{mag}} = \sum_n \psi_n^\dagger [M_{\parallel} \sin(QR_n) \sigma_x + M_{\perp} \cos(QR_n) \sigma_z] \psi_n. \quad (2)$$

Here,  $Q = \pi/2$  denotes the magnetic ordering wave number, which in low-dimensional itinerant magnets it often happens to coincide with the nesting wave number  $Q_N$ . The texture mediates scattering between two distinct pairs of points. In

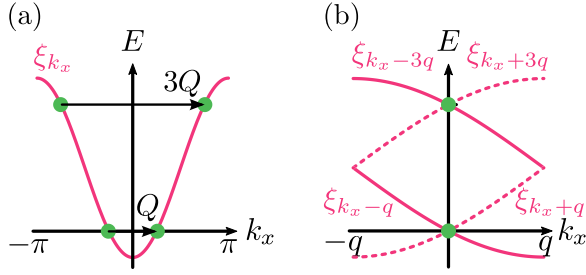


FIG. 3. Example of a 1BM in 1D, obtained by considering a nearest-neighbor hopping with strength  $t$  and a chemical potential value  $\mu = -\sqrt{2}t < 0$ . (a) The resulting dispersion  $\xi_{k_x} = -2t \cos k_x - \mu$  contains two Fermi points at  $k_x = \pm\pi/4$  of the first BZ, which are connected by  $Q_N = Q = \pi/2 \equiv -3\pi/2 = -3Q$ . The texture also mediates the scattering between two points lying at  $E = 2|\mu|$ . (b) The resulting four bands of the dispersion in the MBZ. The points connected by the magnetic wave vectors are depicted with green dots.

this work, one pair usually lies at high energies and the other at low. When the condition  $Q_N = Q$  is met, the latter pair is identified with the two nested Fermi points. See Fig. 3(a) for a concrete example. We observe that when  $|M_\perp| \neq |M_\parallel|$  ( $|M_\perp| = |M_\parallel|$ ) the MHC leads to a spatially varying (constant) magnetic moment. Below we examine each case separately.

### 1. MHC with a spatially constant magnetic moment: $|M_\perp| = |M_\parallel|$

In this case, we follow Ref. [105] and gauge away the spatial dependence of the magnetization profile through a unitary transformation  $\psi_n \mapsto \hat{U} \psi_n$  with  $\hat{U} = \exp(iqR_n \sigma_y)$ , where  $q = Q/2$ . By employing the plane-wave basis, the single-particle Hamiltonian reads as

$$\hat{h}_{k_x} = \xi_{k_x} \mathbb{1}_{\sigma-q\sigma_y} + M\sigma_z = \xi_{k_x;q}^+ \mathbb{1}_{\sigma} + \xi_{k_x;q}^- \sigma_y + M\sigma_z, \quad (3)$$

with  $M_\perp = M_\parallel = M > 0$ . The dispersions read as

$$\xi_{k_x;q}^\pm = (\xi_{k_x-q} \pm \xi_{k_x+q})/2. \quad (4)$$

One observes that the spin-dependent shift of the wave number splits the dispersion into an even and an odd function under inversion, i.e.,  $\xi_{-k_x;q}^\pm = \pm \xi_{k_x;q}^\pm$ . The emergence of the odd function reflects the induction of a Rashba-type SOC. By further considering a generic spin-singlet pairing gap  $\Delta_{k_x}$ , we obtain the Bogoliubov–de Gennes (BdG) Hamiltonian

$$\hat{\mathcal{H}}_{k_x} = \tau_3 \otimes (\xi_{k_x;q}^+ \mathbb{1}_{\sigma} + \xi_{k_x;q}^- \sigma_y) + M \mathbb{1}_{\tau} \otimes \sigma_z + \tau_1 \otimes (\Delta_{k_x;q}^+ \mathbb{1}_{\sigma} + \Delta_{k_x;q}^- \sigma_y), \quad (5)$$

where we introduced the superconducting gaps  $\Delta_{k_x;q}^\pm$  in a similar fashion to  $\xi_{k_x;q}^\pm$  in Eq. (4), as well as the spinor

$$\Psi_{k_x}^\dagger = (\psi_{k_x\uparrow}^\dagger, \psi_{k_x\downarrow}^\dagger, \psi_{-k_x\downarrow}, -\psi_{-k_x\uparrow}). \quad (6)$$

Hence, the many-body mean-field Hamiltonian reads as  $H = \frac{1}{2} \sum_{k_x} \Psi_{k_x}^\dagger \hat{\mathcal{H}}_{k_x} \Psi_{k_x}$ . In the above, we employed the  $\tau_{1,2,3}$  Pauli matrices defined in Nambu electron-hole space. From now on, we adopt the shorthand notation  $A \otimes B \equiv AB$  for Kronecker products, and we omit writing all identity matrices unless this is deemed necessary for reasons of clarity.

Leaving aside for the moment the magnetic point- and space-group symmetries present, the BdG Hamiltonian in Eq. (5) resides in the BDI symmetry class with generalized TR, charge-conjugation and chiral symmetries effected by the operators  $\Theta = \mathcal{K}$ ,  $\Xi = \tau_2 \sigma_y \mathcal{K}$ , and  $\Pi = \tau_2 \sigma_y$ , respectively. Here,  $\mathcal{K}$  denotes complex conjugation.

When  $\Delta_{k_x}$  leads to a fully gapped spectrum, the system harbors an integer number of topologically protected MZMs per edge, with the corresponding  $\mathbb{Z}$  topological invariant given by the winding number  $w$  [186]. To define the winding number, we rely on the chiral symmetry dictating the Hamiltonian and block off-diagonalize it via the unitary transformation  $S = (\Pi + \tau_3)/\sqrt{2}$ :

$$S^\dagger \hat{\mathcal{H}}_{k_x} S = \begin{pmatrix} 0 & \hat{A}_{k_x} \\ \hat{A}_{k_x}^\dagger & 0 \end{pmatrix}. \quad (7)$$

Given the above, we calculate  $\det(\hat{A}_{k_x})$ , which reads as

$$\det(\hat{A}_{k_x}) = (\xi_{k_x;q}^+)^2 + (\Delta_{k_x;q}^+)^2 - (\xi_{k_x;q}^-)^2 - (\Delta_{k_x;q}^-)^2 - M^2 + 2i(\xi_{k_x;q}^- \Delta_{k_x;q}^+ - \xi_{k_x;q}^+ \Delta_{k_x;q}^-) \quad (8)$$

and allows us to define the normalized complex function

$$z_{k_x} = \det(\hat{A}_{k_x}) / |\det(\hat{A}_{k_x})|, \quad (9)$$

and the associated winding number in the complex plane

$$w = \frac{1}{2\pi i} \int_{\text{BZ}} \frac{dz_{k_x}}{z_{k_x}}. \quad (10)$$

To facilitate the evaluation of  $w$ , one relies on its invariance under smooth deformations of the Hamiltonian, i.e., deformations that do not lead to any gap closings of the bulk spectrum. Hence, one assumes that the parameters take such values, so that the system is close to topological phase transitions. In such cases, the main contributions to  $w$  arise from the gap-closing points  $k_c$  of the bulk energy spectrum, determined by  $|\det(\hat{A}_{k_c})| = 0$ . This equation yields the conditions  $\text{Im}[\det(\hat{A}_{k_c})] = 0$  and  $\text{Re}[\det(\hat{A}_{k_c})] = 0$ , whereof the first one reads as

$$\text{Im}[\det(\hat{A}_{k_c})] = \xi_{k_c;q}^- \Delta_{k_c;q}^+ - \xi_{k_c;q}^+ \Delta_{k_c;q}^- = 0 \Rightarrow \xi_{k_c-q} \Delta_{k_c+q} = \xi_{k_c+q} \Delta_{k_c-q}. \quad (11)$$

The above is always satisfied at the ISPs ( $k_{\mathcal{I}} \equiv -k_{\mathcal{I}}$ ). If we momentarily assume that the  $k_x$  dependence of the pairing gap does not lead to any additional gap closings aside from the ones at the ISPs, and take into account the remaining gap-closing condition  $\text{Re}[\det(\hat{A}_{k_c})] = 0$ , we obtain the topological phase transition criterion

$$M = \sqrt{(\xi_{k_{\mathcal{I}};q}^+)^2 + (\Delta_{k_{\mathcal{I}};q}^+)^2} \quad (12)$$

because  $\xi_{k_{\mathcal{I}};q}^- = \Delta_{k_{\mathcal{I}};q}^- = 0$ . Since the 1D BZ contains only the two ISPs  $k_{\mathcal{I}} = \{0, \pi\}$ , the winding number reads as

$$w = \sum_{k_{\mathcal{I}}=0,\pi} \text{sgn} \left( \Delta_{k_{\mathcal{I}};q}^+ \frac{d\xi_{k_{\mathcal{I}};q}^-}{dk_x} - \xi_{k_{\mathcal{I}};q}^+ \frac{d\Delta_{k_{\mathcal{I}};q}^-}{dk_x} \right) \Big|_{k_x=k_{\mathcal{I}}} \times \frac{\text{sgn}[M^2 - (\Delta_{k_{\mathcal{I}};q}^+)^2 - (\xi_{k_{\mathcal{I}};q}^+)^2]}{2}. \quad (13)$$



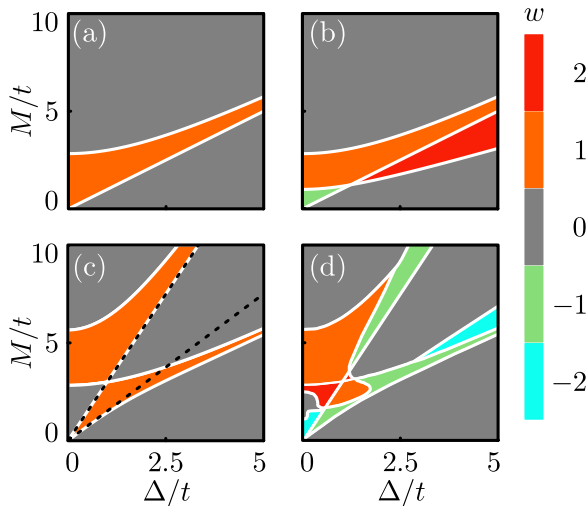


FIG. 4. Topological phase diagrams for the 1BM in Fig. 3 in the MHC phase for (a) a constant pairing gap  $\Delta_{k_x} = \Delta$  and (b) an unconventional pairing gap  $\Delta_{k_x} = \Delta[1 + 2 \cos(2k_x)]$ , which leads to additional gap-closing points. Both (a) and (b) were obtained for  $Q = Q_N$  and a spatially constant magnetic moment, i.e.,  $M_\perp = M_\parallel = M > 0$ . (c), (d) Display the same as in (a) and (b), respectively, but for a spatially varying magnetic moment with  $M_\perp = M > 0$  and  $M_\parallel = M/3$ . The black dotted lines in (c) span the topologically nontrivial region in the weak-coupling limit [see Eq. (31)]. As one observes, this limit is only valid when  $0 < M_{\perp,\parallel}, \Delta \ll 2|\mu|$  are satisfied.

We note that when the magnetic wave vector  $Q\hat{x}$  coincides with the FS nesting vector  $Q_N\hat{x}$ , the expression for the topological invariant further simplifies since  $\xi_{k_{\mathcal{I};q}}^+ = 0$  for at least one of the two ISPs. Remarkably, this special, but actually realistic situation, appears to be the sweet spot for entering the topologically nontrivial phase since the minimum magnetic gap  $M_c = |\Delta_{k_{\mathcal{I};q}}^+|$  is required in this case. Away from this special point, the critical magnetic gap increases, and its value is controlled by the degree of the  $|Q - Q_N|$  detuning, which is reflected in the size of  $|\xi_{k_{\mathcal{I};q}}^+|$ . Therefore, a topological phase transition still occurs even if the special condition  $Q = Q_N$  is not met. We thus conclude that the system exhibits gap closings at wave numbers for which  $\xi_{k_x+Q} = \xi_{k_x}$  and  $d\xi_{k_x+Q}/dk_x = -d\xi_{k_x}/dk_x$ . Notably, both conditions hold trivially for two nested Fermi points given that  $Q = Q_N$ .

For a 1BM model with  $\xi_{0;q}^+ = 0$  and  $\xi_{\pi;q}^+ = 2|\mu|$ , which happens to hold for the 1BM in Fig. 3, Eq. (13) yields

$$w = \frac{1}{2} \sum_{k_{\mathcal{I}}=0,\pi} e^{ik_{\mathcal{I}}} \text{sgn}[M^2 - (\xi_{k_{\mathcal{I};q}}^+)^2 - (\Delta_{k_{\mathcal{I};q}}^+)^2], \quad (14)$$

which implies that the topologically nontrivial regime is realized in the interval

$$\sqrt{(\xi_{0;q}^+)^2 + (\Delta_{0;q}^+)^2} < M < \sqrt{(\xi_{\pi;q}^+)^2 + (\Delta_{\pi;q}^+)^2}. \quad (15)$$

Note, however, that the upper boundary may not be reached in practice since for this purpose, magnetic gap values larger than the Fermi energy are required.

In Fig. 4(a), we numerically determine the topological phase diagram for a conventional  $s$ -wave pairing gap  $\Delta_{k_x} =$

$\Delta > 0$ , given the dispersion in Fig. 3. The orange region displays the parameter space, for which the system is in a topologically nontrivial phase with  $w = 1$ . For the parameters used in the figure, Eq. (15) reduces to  $\Delta < M < \sqrt{8t^2 + \Delta^2}$ , and coincides with the numerically obtained upper and lower bounds of the nontrivial region.

We now continue with addressing the case of an unconventional superconducting order parameter which generates additional gap closings away from ISPs. As a result of chiral and charge-conjugation symmetries, the additional gap closings come in pairs  $\pm k_*$  [80], and thus each pair of gap-closing points of this type generally contributes with  $\pm 1$  units to  $w$ . For an illustration, we consider the gap function  $\Delta_{k_x} = \Delta[1 + 2 \cos(2k_x)]$  which features a single pair of such nodes. The latter nodes have an accidental origin since they are not imposed by the presence of a symmetry, and further contribute to the winding number of Eq. (14).

A numerically obtained example for this case is depicted in Fig. 4(b). The regions with  $w = -1$  and  $+2$  appear due to the fact that the signs of the fractional contributions arising from the  $k_{\mathcal{I}} = 0, \pi$  points are no longer determined by Eq. (14), as a result of the unconventional pairing. Therefore, the contributions of the  $k_{\mathcal{I}}$  points for  $w = -1$  ( $w = +2$ ) cancel out (add up to  $+1$ ), while the contribution from the  $\pm k_*$  gap-closing pairing function is  $-1$  ( $+1$ ). Thus, the inclusion of an unconventional pairing function which leads to additional gap closings at  $\pm k_*$  does not significantly alter the nontrivial region here, but does increase the overall complexity of the phase diagram.

We conclude this section by discussing the impact of the various magnetic point-group symmetries on the topological classification, given that the nonmagnetic part of the BdG Hamiltonian is invariant under the symmetry group of the normal phase. The addition of magnetism reduces the initial point group down to the magnetic point group  $M_{\text{MHC}} = C_2 + (C_{2v} - C_2)\mathcal{T}$ , whose elements are presented in Table I. Any possible implications of the magnetic point group on the topological properties of the system are associated with the emergence of the two *antiunitary* mirror symmetries  $(C_{2v} - C_2)\mathcal{T} = \{\sigma_{xz}\mathcal{T}, \sigma_{yz}\mathcal{T}\}$ . Their presence implies that the symmetry classes for the  $xz$  and  $yz$  HSPs generally differ from the BDI class which was obtained by solely considering the generalized TR symmetry  $\Theta = \mathcal{K}$ . This is because these antiunitary mirror symmetries act as additional generalized TR symmetries in the HSPs. Furthermore, the presence of this set of three TR symmetries induces two *unitary* symmetries  $\{\mathcal{O}_{xz}, \mathcal{O}_{yz}\}$ , whose presence allows for the block diagonalization of the Hamiltonian.

It is customary to describe these effects in terms of  $\{\Theta, \Xi\}$  and their (anti)commutation relations with the generators of the induced unitary symmetries  $\{\mathcal{O}_{xz}, \mathcal{O}_{yz}\}$  [146–148,153], whose expressions are inferrable from the two *unitary* mirror symmetries:

$$\mathcal{R} = (C_{2v} - C_2)\mathcal{T}\Theta \equiv \{\mathcal{R}_{xz}, \mathcal{R}_{yz}\}. \quad (16)$$

Hence, by restricting to the HSPs, we find the expressions  $\mathcal{O}_{xz} \equiv \mathcal{R}_{xz} = \mathbb{1}_\sigma$  and  $\mathcal{O}_{yz} \equiv \mathcal{R}_{yz} = \sigma_z$ .

For the 1D system examined here  $\mathcal{R}_{xz}$  is trivial, while  $\mathcal{R}_{yz}$  is expected to only affect the bulk topological properties of the system since it is violated when boundaries are

introduced. Specifically,  $\mathcal{R}_{yz}$  can influence the classification at the mirror-symmetry-invariant points  $k_{\mathcal{R}_{yz}} = \{0, \pi\}$  satisfying  $\mathcal{R}_{yz}k_{\mathcal{R}_{yz}} \equiv k_{\mathcal{R}_{yz}}$ . For these points  $\xi_{k_{\mathcal{R}_{yz};q}}^- = \Delta_{k_{\mathcal{R}_{yz};q}}^- = 0$ , and the BdG Hamiltonian in Eq. (5) becomes block diagonal and reads as

$$\hat{\mathcal{H}}_{k_{\mathcal{R}_{yz};\sigma}} = \sigma M + \xi_{k_{\mathcal{R}_{yz};q}}^+ \tau_3 + \Delta_{k_{\mathcal{R}_{yz};q}}^+ \tau_1, \quad (17)$$

where we used the eigenvectors of  $\sigma_z$ , which are labeled by  $\sigma = \pm 1$ . The above Hamiltonian belongs to symmetry class AI  $\oplus$  AI with  $\Theta = \mathcal{K}$ , which in 0D yields the mirror topological invariant  $n_M \in \mathbb{Z}$ . See Refs. [20,146].

To calculate  $n_M$ , we choose an approach which keeps the variety of the topological-invariant constructions used in this work to a minimum. This is achieved by evaluating the mirror invariant in an augmented space, which is spanned by the spatial dimensions relevant for the classification, and the continuous frequency  $\epsilon \in (-\infty, \infty)$  obtained as the zero-temperature limit of the Matsubara frequencies. Adding  $\epsilon$  compensates the reduction of the physical dimensions by one, which occurs when restricting to a HSP. As a result, this allows us to describe both bulk and HSPs using a winding number defined in the natural and augmented 1D spaces, respectively.

The topological invariant for the AI class in 0D is thus given here by the winding number of the normalized complex number  $Z_{\epsilon}$ , obtained from the normalized determinant of the inverse single-particle Matsubara Green function  $\hat{\mathcal{G}}_{\epsilon}^{-1} = i\epsilon - \hat{\mathcal{H}}_{\text{BdG}}$ . See Refs. [20,187,188] for further details on topological invariants based on Green functions. In the present case, we have for each  $\sigma$  block

$$n_{k_{\mathcal{R}_{yz};\sigma}} = \frac{1}{4\pi i} \int_{-\infty}^{+\infty} \frac{dZ_{\epsilon,\sigma}}{Z_{\epsilon,\sigma}}, \quad (18)$$

with  $Z_{\epsilon,\sigma} = -\det(\hat{\mathcal{G}}_{\epsilon,\sigma}^{-1})/|\det(\hat{\mathcal{G}}_{\epsilon,\sigma}^{-1})|$ . We thus find

$$-\det(\hat{\mathcal{G}}_{\epsilon,\sigma}^{-1}) = (\xi_{k_{\mathcal{R}_{yz};q}}^+)^2 + (\Delta_{k_{\mathcal{R}_{yz};q}}^+)^2 - (i\epsilon)^2 - M^2 + 2i\sigma\epsilon M, \quad (19)$$

which has a form similar to that of the determinant in Eq. (8), that was employed to calculate the winding number  $w$  in  $k_x$  space.<sup>2</sup> To be in accordance with Ref. [146], given the definition in Eq. (18), we define the mirror invariant  $n_M$  using a single  $\sigma$  block of our choice as follows:

$$n_M = 2 \operatorname{sgn}(n_{k_x=0,\sigma} - n_{k_x=\pi,\sigma}) (|n_{k_x=0,\sigma}| - |n_{k_x=\pi,\sigma}|). \quad (20)$$

$n_M$  counts the number of mirror-symmetry-protected edge states for edges preserving the respective mirror symmetry. However, as we announced, the above invariant becomes obsolete in 1D systems since mirror symmetry is expected to be broken when termination edges are present. Nevertheless, here we rely on the translational invariance of the system and

instead introduce a set of bulk mirror invariants. In analogy to the spin Chern number construction [189–191], we define

$$n_{M;k_{\mathcal{R}_{yz}}} = \sum_{\sigma} \sigma n_{k_{\mathcal{R}_{yz};\sigma}}. \quad (21)$$

After evaluating  $n_{k_{\mathcal{R}_{yz};\sigma}}$ , we find that  $n_{M;k_{\mathcal{R}_{yz}}}$  becomes

$$n_{M;k_{\mathcal{R}_{yz}}} = \frac{\operatorname{sgn}[(\xi_{k_{\mathcal{R}_{yz};q}}^+)^2 + (\Delta_{k_{\mathcal{R}_{yz};q}}^+)^2 - M^2] - 1}{2}. \quad (22)$$

This bulk mirror invariant reflects the quantization of the  $z$ -axis magnetization<sup>3</sup> in HSPs since  $\langle \sigma_z \rangle_{k_x=k_{\mathcal{R}_{yz}}} = n_{M;k_{\mathcal{R}_{yz}}}$ . One finds  $|n_{M;k_{\mathcal{R}_{yz}}}| = 1$  only after certain level crossings occur at  $k_{\mathcal{R}_{yz}}$ , thus bearing similarities to parity-switching level crossings known for Yu-Shiba-Rusinov bound states [192], which are induced by magnetic impurities in spin-singlet superconductors [193].

The measurement of the  $k_x$ -resolved magnetization appears experimentally feasible by means of spin-resolved angle-resolved photoemission spectroscopy, which has already been successfully applied to map out the spin character of the surface states of TR-invariant 3D topological insulators [194]. We thus find that, although the unitary mirror symmetry  $\mathcal{R}_{yz}$  is generally broken when edges are introduced to the system, we can still use  $n_{M;k_{\mathcal{R}_{yz}}}$  as a bulk experimental probe for topological superconductivity. Finally, we remark that the above calculations also serve as a simple example of similar derivations that we plan to carry out in the upcoming sections.

## 2. MHC with a spatially varying magnetic moment: $|M_{\perp}| \neq |M_{\parallel}|$

We now extend the study of the previous section to the more general situation, in which  $|M_{\perp}| \neq |M_{\parallel}|$ . In this case, using a spin-dependent unitary transformation to gauge away the spatial dependence of the MHC is no longer possible, and one has to approach the problem in the MBZ, i.e.,  $k_x \in (-q, q]$ , with  $q = Q/2 = \pi/4$ . To describe the downfolding to the MBZ, one can either consider a sublattice description which is briefly discussed in Appendix A, or choose to express the Hamiltonian in  $\{k_x, k_x + Q\}$  and  $\{k_x, k_x + 2Q\}$  wave-number-transfer spaces. The former is advantageous for carrying out the topological classification since the resulting BdG Hamiltonian is  $2\pi$  periodic and thus suitably compactified. The results presented in Tables II and III were obtained using this approach. However, throughout the main text we follow the second route, which is implemented by introducing the enlarged spinor

$$\mathcal{X}_{k_x}^{\text{IBM}} = \mathbb{1}_{\eta} \otimes \frac{\rho_2 + \rho_3}{\sqrt{2}} (\Psi_{k_x-q}, \Psi_{k_x+q}, \Psi_{k_x+3q}, \Psi_{k_x-3q})^{\top}, \quad (23)$$

where we introduced the Pauli matrices  $(\rho_{1,2,3})$   $\eta_{1,2,3}$  defined in the  $(Q-)$   $2Q$ -transfer space. The above basis reveals more transparently the mechanisms underlying the nontrivial topological properties induced by the magnetic textures, it

<sup>2</sup>Note that the Green function approach could have been also used to evaluate the winding number  $w$  in Eq. (10), by means of a first Chern number in the augmented  $(\epsilon, k_x)$  space. This method has clear advantages if we wish to include possible self-energy effects.

<sup>3</sup>Recall that the above is expressed in the local spin frame. Rotating back with  $\hat{U}^{\dagger}$  implies that  $n_{M;k_{\mathcal{R}_{yz}}}$  leads to the quantization of the staggered magnetization in the  $xz$  spin plane.

highlights the emergent Dirac physics, and it provides a simpler and more convenient framework to evaluate the various topological invariants.

The wave-number shifts in the arguments of the above spinor were chosen to connect to the spinor obtained after performing the unitary transformation  $\hat{U}$  in the case  $|M_{\perp}| = |M_{\parallel}|$ . See also Fig. 3(b) and note that, given our spinor choice, the periodic magnetization opens gaps at  $k_x = 0$  when  $Q = Q_N$ . The extended BdG Hamiltonian reads as  $\hat{\mathcal{H}}_{k_x} = \hat{\mathcal{H}}_{k_x}^0 + \hat{\mathcal{H}}_{\text{mag}}$  with

$$\begin{aligned} \hat{\mathcal{H}}_{k_x}^0 &= [h_{k_x}^{(0)} + h_{k_x}^{(1)}\rho_2 + h_{k_x}^{(2)}\eta_3 + h_{k_x}^{(3)}\eta_3\rho_2]\tau_3 \\ &\quad + [\Delta_{k_x}^{(0)} + \Delta_{k_x}^{(1)}\rho_2 + \Delta_{k_x}^{(2)}\eta_3 + \Delta_{k_x}^{(3)}\eta_3\rho_2]\tau_1, \\ \hat{\mathcal{H}}_{\text{mag}} &= -\frac{M_{\perp}(\mathbb{1} + \eta_1)\rho_1\sigma_z + M_{\parallel}(\mathbb{1} - \eta_1)\rho_3\sigma_x}{2}, \end{aligned} \quad (24)$$

where the functions  $h_{k_x}^{(s)}$  and  $\Delta_{k_x}^{(s)}$  appearing above, with  $s = 0, 1, 2, 3$ , constitute linear combinations of  $\xi_{k_x}$  and  $\Delta_{k_x}$ , which follow from the general definitions

$$f_{k_x}^{(0)} = (f_{k_x-q} + f_{k_x+q} + f_{k_x+3q} + f_{k_x-3q})/4, \quad (25)$$

$$f_{k_x}^{(1)} = (f_{k_x-q} - f_{k_x+q} + f_{k_x+3q} - f_{k_x-3q})/4, \quad (26)$$

$$f_{k_x}^{(2)} = (f_{k_x-q} + f_{k_x+q} - f_{k_x+3q} - f_{k_x-3q})/4, \quad (27)$$

$$f_{k_x}^{(3)} = (f_{k_x-q} - f_{k_x+q} - f_{k_x+3q} + f_{k_x-3q})/4. \quad (28)$$

The above construction further implies that inversion  $k_x \mapsto -k_x$  acts as  $f_{-k_x}^{(s)} = (-1)^s f_{k_x}^{(s)}$ . One observes that the four linear combinations resulting from the electron part  $h_{k_x}^{(0)} + h_{k_x}^{(1)}\rho_2 + h_{k_x}^{(2)}\eta_3 + h_{k_x}^{(3)}\eta_3\rho_2$  of the nonmagnetic BdG Hamiltonian give rise to the four spin-degenerate band segments in the MBZ shown in Fig. 3(b).

We point out that the set of ISPs in the MBZ reads as  $k_{\mathcal{I}} = \{0, q \equiv -q\}$ , while the  $k_{\mathcal{I}} = \pi$  of the original BZ coincides now with  $k_{\mathcal{I}} = 0$  in the MBZ. Note that the inversion-symmetric nature of  $k_x = \pm q$  is established via the equivalence relation  $-q \equiv q + nQ$  with  $n \in \mathbb{Z}$ .

The magnetic point group dictating the above BdG Hamiltonian is identical to the one examined in the previous section for a MHC with a spatially constant magnetic moment ( $|M_{\perp}| = |M_{\parallel}|$ ). However, before discussing its implications on the topological classification, we point out that given the enlarged basis in Eq. (23), which is indispensable here for the description of the MHC, one needs to account for possible space-group symmetries.

Specifically, as also presented in Table I, the additional space-group symmetries  $\{\mathcal{T} | \pi/Q\}$  and  $\{\sigma_{xz, yz} | \pi/Q\}$  become now relevant. Throughout this work, we adopt the Seitz notation  $\{g | \mathbf{t}\}$ , which combines the point-group element  $g$  with the translation  $\mathbf{t}$ . Given our choice of basis,  $\{\mathbb{1} | \pi/Q\} = -ie^{ik_x\pi/Q}\rho_2$  and  $\mathcal{T} = i\sigma_y\mathcal{K}$  as usual, while the mirror operations have the following  $\rho \otimes \sigma$  space matrix structure, i.e.,  $\hat{\sigma}_{yz} = i\rho_1\sigma_x$  and  $\hat{\sigma}_{xz} = i\sigma_y$ . Hence, we find the unitary symmetries with  $\{\hat{\sigma}_{yz} | \pi/Q\} = ie^{ik_x\pi/Q}\rho_3\sigma_x$ ,  $\{\hat{\sigma}_{xz} | \pi/Q\} = e^{ik_x\pi/Q}\rho_2\sigma_y$ , and the antiunitary symmetry  $\hat{\Theta}_{k_x} \equiv \{\mathcal{T} | \pi/Q\} = e^{ik_x\pi/Q}\rho_2\sigma_y\mathcal{K}$ . In contrast to the physical TR operation which satisfies  $\mathcal{T}^2 = -\mathbb{1}$ , here  $\hat{\Theta}_{k_x}^2 = e^{i\pi k_x/q}\mathbb{1}$  and leads to a Kramers degeneracy only at the  $k_x = q$  ISP in the MBZ

[195–197]. Notably, this is the mechanism underlying the persistent Kramers degeneracies at the purple-colored points of the MBZ shown in Fig. 1(h). As also discussed in Appendix B, the above space-group symmetries do not lead to any further symmetry-protected degeneracies in the spectrum, and thus influence the topological classification only in HSPs. For this reason, their implications are discussed later, together with the magnetic point-group symmetries.

The extended BdG Hamiltonian belongs to class BDI and is classified by a winding number  $w \in \mathbb{Z}$ . Applying the methods of Sec. IV A 1, and assuming for simplicity that  $Q = Q_N$ , and  $\Delta_{k_x} = \Delta > 0$  so that  $\Delta_{k_x}^{(0)} = \Delta$  and  $\Delta_{k_x}^{(s)} = 0$  for  $s = 1, 2, 3$ , lead to (see Appendix C 1 for details)

$$w = \sum_{\nu} \frac{\nu}{2} \text{sgn} \left\{ (M_{\nu}^2 - \Delta^2) - \frac{(M_{\perp}^2 - \Delta^2)(M_{\parallel}^2 - \Delta^2)}{(2\mu)^2} \right\}, \quad (29)$$

with  $M_{\nu} = (M_{\parallel} + \nu M_{\perp})/2$  and  $\nu = \pm 1$ .

Figure 4(c) depicts the topological phase diagram for the 1BM in Fig. 3 when  $M_{\perp} = M$  and  $M_{\parallel} = M/3$ . The orange regions are phases with a single MZM per edge. While the anisotropic nature of the MHC does not lead to the removal of the topologically nontrivial phase, it still significantly modifies the phase diagram. It is straightforward to verify that for  $\Delta_{k_x} = \Delta$ , the gap closings responsible for the topological phase transition take place only at  $k_x = 0$ . Nonetheless, Eq. (29) also holds for an unconventional superconducting order parameter after replacing  $\Delta \mapsto \Delta_{k_x=0}$ , under the condition that additional gap-closing points do not emerge. Instead, for an unconventional pairing order parameter which leads to additional gap closings at  $\pm k_*$ , the topological phase diagram ends up to be quite complex. After obtaining  $w$  for a generic  $\Delta_{k_x}$  (see Appendix C 2), we focus on a pairing gap  $\Delta_{k_x} = \Delta[1 + 2 \cos(2k_x)]$ . The related topological phase diagram is depicted in Fig. 4(d).

To gain deeper insight, we set  $\Delta_{k_x} = \Delta > 0$  and restrict to the weak-coupling limit  $|\Delta|, |M_{\parallel, \perp}| \ll 2|\mu|$ . Since gap closings now occur only near the FS, Eq. (29) becomes

$$w = \frac{\text{sgn}(M_{+}^2 - \Delta^2) - \text{sgn}(M_{-}^2 - \Delta^2)}{2}. \quad (30)$$

Thus, the topological phases arising from gap closings occurring in the low-energy sector are solely determined by the inequality

$$M_{-} < \Delta < M_{+} \quad \text{for} \quad M_{\perp, \parallel} \geq 0. \quad (31)$$

The spatial variation of the magnetic moment, which is reflected in the size of the difference  $|M_{-}| = |M_{\parallel} - M_{\perp}|$ , sets a maximum value for the magnetic anisotropy that can still allow for the system to enter the nontrivial phase. For the specific parameters used in Fig. 4(c), the above inequality reduces to  $3\Delta/2 < M < 3\Delta$ . The low-energy nontrivial region is therefore spanned by the black dotted lines in Fig. 4(c), which verifies that Eq. (30) indeed describes the exact model well in the weak-coupling limit.

The results in the weak-coupling limit can be alternatively obtained by directly restricting the multicomponent spinor of Eq. (23) to the operators creating and annihilating electrons in

the low-energy sector, i.e.,

$$\chi_{k_x}^{\text{IBM}} = \frac{\rho_2 + \rho_3}{\sqrt{2}} (\Psi_{k_x - q}, \Psi_{k_x + q})^\top. \quad (32)$$

The projection of the Hamiltonian in Eq. (24) onto this subspace is achieved by setting  $\eta_3 = +1$ , and dropping the term proportional to  $\eta_1$  which connects the low- and high-energy sectors. These steps lead to the Hamiltonian

$$\hat{\mathcal{H}}_{k_x}^{\text{low-en}} = (\xi_{k_x; q}^+ + \xi_{k_x; q}^- \rho_2) \tau_3 - \frac{M_\perp \rho_1 \sigma_z + M_\parallel \rho_3 \sigma_x}{2} + (\Delta_{k_x; q}^+ + \Delta_{k_x; q}^- \rho_2) \tau_1, \quad (33)$$

with  $\xi_{k_x; q}^\pm$  and  $\Delta_{k_x; q}^\pm$  following once again from Eq. (4).

We now discuss the impact of the unitary mirror  $\mathcal{R}_{x,z}$  and space-group  $\{\sigma_{x,z} | \pi/q\}$  symmetries on the topological classification in HSPs. First of all,  $\tilde{\Theta}_{k_x}$  imposes a twofold degeneracy at  $k_x = q$ , thus implying that the magnetic texture does not induce any new topologically nontrivial phases at  $k_x = q$ . See Table II and Appendix A for more details. Even more, as in Sec. IV A 1, also here, the effects of  $\mathcal{R}_{x,z}$  are trivial since they lead to a unitary symmetry  $\mathcal{O}_{x,z} = \mathbb{1}$ . The remaining four symmetries modify the topological properties at  $k_x = 0$ . The symmetries  $\mathcal{R}_{y,z}$  and  $\{\sigma_{y,z} | \pi/q\}$  ( $\{\mathcal{T} | \pi/q\}$  and  $\{\sigma_{x,z} | \pi/q\}$ ) lead to a AI  $\oplus$  AI (BDI  $\oplus$  BDI) class, thus providing an additional  $\mathbb{Z}$  ( $\mathbb{Z}_2$ ) topological invariant to the winding number  $w$ .

The  $\mathcal{R}_{y,z}$  symmetry allows defining two types of mirror invariants, in analogy to Eqs. (20) and (21). The block diagonalization of the BdG Hamiltonian in Eq. (24), that is effected by the unitary transformation  $(\mathcal{O}_{y,z} + \sigma_x)/\sqrt{2}$ , yields in the weak-coupling limit (see also Appendix C 3)

$$2n_{M, k_x=0} = \sum_{v=\pm 1} v \operatorname{sgn}[(\xi_{0,q}^+)^2 + (\Delta_{0,q}^+)^2 - M_v^2]. \quad (34)$$

It is straightforward to verify that  $n_{M, k_x=0} = n_M$  since no topological gap closings can take place at  $k_x = q$ . In a similar fashion, the off-centered<sup>4</sup> space-group symmetry  $\{\sigma_{y,z} | \pi/q\}$  allows introducing the here-termed glide invariant  $n_{G, k_x=0} \in \mathbb{Z}$ , which is defined following Eqs. (18) and (21). As pointed out in Sec. IV A 1 and Footnote 3, also here the staggered magnetization in the  $z$ - ( $x$ -) spin axis becomes quantized when  $n_{M, k_x=0}$  ( $n_{G, k_x=0}$ ) is nonzero since  $2n_{M, k_x=0} = \langle \rho_1 \sigma_z \rangle_{k_x=0}$  ( $2n_{G, k_x=0} = \langle \rho_3 \sigma_x \rangle_{k_x=0}$ ). For the given model  $|n_{M, k_x=0}| = |n_{G, k_x=0}|$ .

We now proceed with the  $\mathbb{Z}_2$  topological invariants which emerge from the  $\{\mathcal{T} | \pi/q\}$  and  $\{\sigma_{x,z} | \pi/q\}$  symmetries. In the presence of either one of these, the unitary symmetry  $\tilde{\mathcal{O}} = \rho_2 \sigma_y$  is induced, and allows us to block diagonalize the Hamiltonian in Eq. (24) via the unitary transformation  $(\tilde{\mathcal{O}} + \sigma_z)/\sqrt{2}$ . This yields the BDI blocks

$$\hat{\mathcal{H}}_{k_x=0, \sigma} = \hat{\mathcal{H}}_{k_x=0}^0 - (M_\sigma - M_{-\sigma} \eta_1) \rho_1, \quad (35)$$

with  $\sigma = \pm 1$  labeling the eigenstates of  $\sigma_z$ . The two blocks see a chiral symmetry  $\Pi = \rho_2 \tau_2$ . Following the same ap-

<sup>4</sup>The nonmenclature highlights that this symmetry is not nonsymmorphic because we can choose a coordinate system in the direct lattice for which  $\{\sigma_{y,z} | \pi/q\} \mapsto \sigma_{y,z}$ . See also Appendix B.

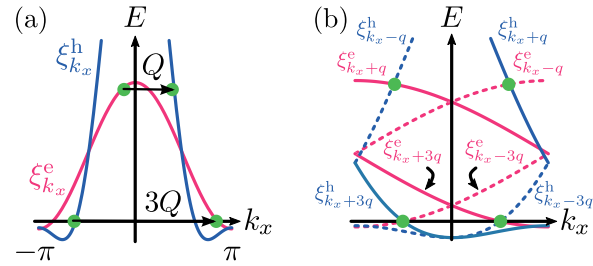


FIG. 5. Example of a 2BM in 1D. (a) The dispersions  $\xi_{k_x}^e = t_e \cos k_x - \varepsilon_e$  (fuchsia) and  $\xi_{k_x}^h = t_h \cos k_x + t'_h [1 + \cos(2k_x)] - \varepsilon_h$  (navy blue) in the first BZ. We set the parameter values  $t_h = 2.86 t_e$ ,  $t'_h = t_e$ ,  $\varepsilon_e \simeq -0.92 t_e$ , and  $\varepsilon_h = -0.80 t_e$ . We also show the nesting wave vector  $Q_N \hat{x}$  which, for the choice of parameters made here, coincides with the magnetic wave vector  $Q \hat{x}$ . Thus,  $Q \hat{x}$  connects two pairs of points at the Fermi level and two more pairs at higher energies. (b) The resulting eight band segments in the MBZ. The points connected by the magnetic wave number ( $3Q = -Q$ ) come in pairs due to  $C_2$  symmetry, and are depicted by green dots. For clarity, (a) depicts half of the ordering wave numbers.

proach that led to Eq. (7), we block off-diagonalize each  $\sigma$  block by means of the unitary transformation  $(\Pi + \tau_3)/\sqrt{2}$ , with the upper block denoted  $\hat{A}_{k_x=0, \sigma}$ . The  $\mathbb{Z}_2$  invariant, that we here term glide Majorana parity  $P_G$ , is constructed in Appendix C 4 and is defined as

$$P_{G, k_x=0} = \operatorname{sgn} \prod_{\sigma=\pm 1} \det(\hat{A}_{k_x=0, \sigma}). \quad (36)$$

Within the weak-coupling limit, we obtain the result

$$P_{G, k_x=0} = \operatorname{sgn} \prod_{\sigma=\pm 1} [(\xi_{0,q}^+)^2 + (\Delta_{0,q}^+)^2 - M_\sigma^2]. \quad (37)$$

Hence, here we end up with  $P_{G, k_x=0} = (-1)^{n_{M, k_x=0}}$ , which implies that in the present model  $P_{G, k_x=0}$  is nontrivial, i.e., equal to  $-1$ , when  $n_{M, k_x=0} \in 2\mathbb{Z} + 1$ .

Concluding this section, we remark once again that in strictly 1D systems the above point- and space-group symmetries affect only the bulk topological properties since these are all broken when edges are introduced. When this takes place, it is only  $w$  together with the weak  $\mathbb{Z}_2$  invariant of class BDI,<sup>5</sup> which are capable of predicting the number of the arising MZMs. This is in stark contrast to 2D systems, where certain edges also support crystalline and/or weak invariants, as discussed further in later sections.

## B. Two-band models

In this section, we extend the previous analysis to the case of two-band models (2BMs) with dispersions  $\xi_{k_x}^{e,h}$ , where the superscript e/h reflects the type of electron/hole pocket that

<sup>5</sup>We define the weak invariant  $P_{\mathcal{M}} = \operatorname{sgn} \prod_{k_{\mathcal{T}}} \det(\hat{A}_{k_{\mathcal{T}}}) \equiv \operatorname{sgn}[\det(\hat{A}_{k_x=0})]$ , with  $\hat{A}_{k_{\mathcal{T}}}$  the upper off-diagonal block of the block off-diagonalized Hamiltonian in Eq. (24) evaluated at  $k_{\mathcal{T}}$ . The arising equivalence is a result of the Kramers degeneracy at  $k_x = q$ . When either  $\{\mathcal{T} | \pi/q\}$  or  $\{\sigma_{x,z} | \pi/q\}$  is a symmetry,  $P_{\mathcal{M}}$  coincides with the glide Majorana parity  $P_{G, k_x=0}$  in Eq. (36).

arises from the respective band. An example of such a 2BM is shown in Fig. 5. We employ the  $\kappa_{1,2,3}$  Pauli matrices to represent Hamiltonian matrix elements in band space. This representation is also relevant for the magnetic and pairing terms, which now become matrices in this space. In particular, the direct-lattice profile of the magnetization generally reads as

$$\hat{M}_n = \frac{M_n^e + M_n^h}{2} + \frac{M_n^e - M_n^h}{2} \kappa_3 + M_n^{eh} \kappa_1. \quad (38)$$

One notes that a term proportional to  $\kappa_2$  is not allowed since this violates the requirement that the magnetization field of the texture is odd under  $\mathcal{T}$ . On the other hand, the spin-singlet pairing matrix reads as

$$\begin{aligned} \hat{\Delta}_{k_x} = & \frac{\Delta_{k_x}^e + \Delta_{k_x}^h}{2} + \frac{\Delta_{k_x}^e - \Delta_{k_x}^h}{2} \kappa_3 \\ & + \frac{\Delta_{k_x}^{eh} + \Delta_{k_x}^{he}}{2} \kappa_1 - \frac{\Delta_{k_x}^{eh} - \Delta_{k_x}^{he}}{2i} \kappa_2. \end{aligned} \quad (39)$$

The required antisymmetry of the superconducting matrix order parameter in the combined spin, band, and  $k_x$  spaces implies that the terms proportional to  $\mathbb{1}_\kappa$ ,  $\kappa_3$ , and  $\kappa_1$  are even under inversion, while the one proportional to  $\kappa_2$  is odd. In the remainder, we focus on cases where the FSs associated with the various pockets neither overlap nor share similar shapes and, as a result, interband pairing is expected to be substantially suppressed.<sup>6</sup>

In the present case we also consider that the magnetization possesses a MHC form, with the  $M_{\parallel,\perp}$  helix components of the previous section being upgraded to band-space matrices according to Eq. (38). In addition, we assume that the two intraband pairing order parameters  $\Delta_{k_x}^{e,h}$  do not contain any zeros and, thus, we set them to be constants. Nonetheless, our results qualitatively hold for more complex unconventional gap structures, as long as these do not contain any zeros. We further note that, here, the inclusion of an additional band does not lower the symmetry of the Hamiltonian, and the system is therefore left invariant under the magnetic point- and space-group symmetries discussed in the previous section.

Since the 2BMs bear similarities with the thoroughly explored 1BMs, we confine the analysis to the distinct features

<sup>6</sup>Note also that interband pairing appears more possible to arise in 1D rather than 2D systems since the FS in the former case consists of points. For nonoverlapping FSs, the appearance of interband pairing requires a suitable bosonic “glue,” such as antiferromagnetic magnons, which can provide the wave-vector transfer that is required to connect the different bands [198]. Even more, the development of interband pairing in such cases either leads to a net momentum in the ground state (Fulde-Ferrell phase [199]) or spontaneously violates translational invariance (Larkin-Ovchinnikov phase [200]). This may in turn generate electric currents or elastic deformations which result in additional energy penalties for band structures which originally respect TR and translational symmetries. Finally, in the here more relevant case of 2D systems which harbor multiple nonsimilar and nonoverlapping FSs, interband pairing is expected to be further disfavored since the establishment of a full gap on the FSs requires the development of a pairing order parameter which consists of multiple wave vectors [198].

brought about by the additional band. We extend the spinor defined in Eq. (23) as follows:

$$\mathcal{X}_{k_x}^{2\text{BM}} = (\mathcal{X}_{k_x}^{1\text{BM}^e}, \mathcal{X}_{k_x}^{1\text{BM}^h})^\top \quad (40)$$

and consider the Hamiltonian

$$\hat{\mathcal{H}}_{k_x} = \sum_s^{\text{e,h}} \mathcal{P}_s \hat{\mathcal{H}}_{k_x}^{0:s} - \frac{\hat{M}_\perp (\mathbb{1} + \eta_1) \rho_1 \sigma_z + \hat{M}_\parallel (\mathbb{1} - \eta_1) \rho_3 \sigma_x}{2}, \quad (41)$$

where we introduced the electronlike (holelike) band projectors  $\mathcal{P}_e = (\mathbb{1}_\kappa + \kappa_3)/2$  [ $\mathcal{P}_h = (\mathbb{1}_\kappa - \kappa_3)/2$ ]. Depending on the precise matrix form of the magnetization, one can interpolate between intraband and interband scattering.

For  $\hat{M}_{\parallel,\perp} \propto \mathbb{1}_\kappa$ ,  $\kappa_3$ , the magnetic scattering has only an intraband character, and the two bands are completely decoupled. Thus, the topological properties of the system follow from applying the results of the previous paragraphs separately to each band, and the symmetry class is  $\text{BDI} \oplus \text{BDI}$ . In contrast, when  $\hat{M}_\perp = M_\perp \kappa_1$  and  $\hat{M}_\parallel = M_\parallel \kappa_1$ , the Hamiltonian exhibits an additional unitary symmetry with the generator  $\mathcal{O} = \kappa_3 \sigma_y$ . Note that this symmetry is due to the specific form of the magnetic texture in band space, and intraband magnetic scattering terms  $\hat{M}_{\perp,\parallel} \propto \mathbb{1}_\kappa$ ,  $\kappa_3$  generally violate it.

Assuming the presence of  $\mathcal{O}$ , we block diagonalize the Hamiltonian using the transformation  $\mathcal{S} = (\mathcal{O} + \sigma_z)/\sqrt{2}$ , and find that the nonmagnetic part of Eq. (41) remains unaltered, while the magnetic part becomes

$$\hat{\mathcal{H}}_{\text{mag},\sigma} = -\frac{\sigma M_\perp \kappa_1 (\mathbb{1} + \eta_1) \rho_1 + M_\parallel \kappa_2 (\mathbb{1} - \eta_1) \rho_3}{2}, \quad (42)$$

where  $\sigma = \pm 1$  correspond to the eigenvalues of  $\sigma_z$ . Each Hamiltonian block belongs to the symmetry class AIII with  $\Pi = \kappa_3 \tau_2$ . The procedure for carrying out the 1D topological analysis is here identical to the one presented in Sec. IV A 2 for systems in the BDI symmetry class, since also the AIII class supports a  $\mathbb{Z}$  topological invariant in 1D, which is identified with a winding number.

Such an analysis (see Appendix C 5) yields that the topological phase transition from the trivial to the nontrivial phase occurs when  $\xi_{k_x \pm 3q}^e \Delta^h = \xi_{k_x \mp 3q}^h \Delta^e$  and  $\xi_{k_x \pm 3q}^e \xi_{k_x \mp 3q}^h + \Delta^e \Delta^h = M_\sigma^2$  are simultaneously satisfied for a given  $\sigma$ . When the magnetic wave vectors connect two points at the Fermi level, we have  $\xi_{k \pm 3q}^e = \xi_{k \mp 3q}^h = 0$  and the topological criterion reads as  $\Delta^e \Delta^h = M_\sigma^2$ . Remarkably, the latter condition can be satisfied only when the two magnetically connected points exhibit the *same* sign for the pairing term. Figures 6(a) and 6(b) display the resulting phase diagrams for  $\Delta^h/\Delta^e = \{2, \frac{1}{10}\}$ , respectively, with the topologically nontrivial regions marked in red. In agreement with the above criterion, we find that the nontrivial regime shrinks when  $|\Delta^e - \Delta^h|$  increases.

We note the doubling of  $w$  compared to the case of the 1BMs [cf. Figs. 4(a) and 4(c)]. This is due to the doubling of the number of gap-closing points  $k_c$ . Each one of the green dots in Fig. 5(b) contributes with a single unit to  $w$ . The emergence of a number of  $2\mathbb{Z}$  MZMs in conjunction with the AIII classification implies that each emergent pair of MZMs should be seen as a single topologically protected AZM.

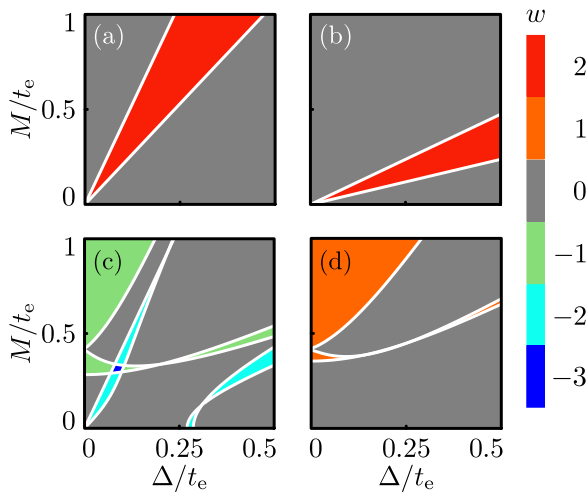


FIG. 6. Topological phase diagrams for the 2BM in Fig. 5 in the MHC phase, evaluated by projecting onto the low-energy sector. (a) Phase diagram when solely interband magnetic scattering is considered, and the order-parameter values  $\Delta^h = \Delta$  and  $\Delta^e = \Delta/2$  are employed. (b) Same as in (a), but with  $\Delta^h/\Delta^e = \frac{1}{10}$ . When  $\Delta^h\Delta^e < 0$  the topologically nontrivial phase vanishes. (c) Same as in (a), but with the inclusion of intraband magnetic scattering, with  $M_{\parallel,\perp}^e = M_{\parallel,\perp}^h = M$ . (d) Here,  $\Delta^h = -2\Delta^e$  and  $M_{\parallel,\perp}^e = M_{\parallel,\perp}^h = M$ . Notably, the inclusion of intraband magnetic scattering induces a topologically nontrivial phase in an otherwise trivial region. We considered  $M_{\perp}^{\text{eh}} = M$  and  $M_{\parallel}^{\text{eh}} = M/3$  in all calculations.

Indeed, from the analyses of Refs. [21,22], it emerges that here a TSC originating from an interband-only magnetic texture can be described with a spinor of halved dimensionality compared to the one defined in Eq. (40) since spin-up electrons of the electronlike pocket pair up only with spin-down electrons of the holelike pocket, and vice versa. While so far there exists only a little theoretical activity on AZMs compared to MZMs (cf. Refs. [101,177–180]), their experimental creation and manipulation is a fascinating topic on its own. Indeed, when these AZMs are topologically protected for an extended region in the parameter space, as found here, they in principle enable quantum information processing with long-lived quasiparticles [181,182].

In the more general case, intraband terms which break the  $\mathcal{O} = \kappa_3\sigma_y$  symmetry may also be present. These can be divided into nonmagnetic and magnetic. When these are nonmagnetic, e.g., various types of ISB SOC, they stabilize a DIII symmetry class which supports MZM Kramers pairs. For a similar situation, see Ref. [44]. However, throughout this work we consider that all types of ISB SOC have negligible strengths, thus implying that such a possibility is inaccessible here. Nonetheless, as we discuss later in this paper, DIII class Majorana fermions become generally accessible in 2D 2BMs for a  $\text{SWC}_4$  texture. On the other hand, when additional magnetic terms are considered, these restore the BDI class found in the 1BMs, as well as the Majorana nature of the topologically protected edge excitations.

We proceed by investigating the effects of intraband magnetic texture terms. For this purpose, we recalculate the winding number (see Appendix C 5), and obtain the phase diagrams in Figs. 6(c) and 6(d) for  $\Delta^h/\Delta^e = \pm 2$ , respectively.

Strikingly, as seen in Fig. 6(d), the inclusion of intraband magnetic scattering induces a topologically nontrivial phase, even when the connected points exhibit different signs for the pairing term. Once again, assuming that the transition occurs due to the gap closing at two magnetically connected Fermi points, and that the magnetic moments are spatially constant, the topological criterion reads as

$$(\Delta^e \pm M^e)(\Delta^h \pm M^h) = (M^{\text{eh}})^2. \quad (43)$$

This expression imposes severe constraints on the unconventional superconducting order parameter, as well as the relative contributions of intraband and interband magnetism, which can lead to topologically nontrivial phases in 1D. Nonetheless, this condition is not as stringent in higher-dimensional systems since the pairing term may lead to a gap closing for some of the BZ points, which is a sufficient condition to allow, but not necessarily guarantee, the transition to a TSC phase.

To this end, we remark that crystalline symmetries generally influence the bulk classification of multiband systems in a similar fashion to 1BMs when interband and intraband magnetic texture terms are simultaneously present. Instead, when only interband textures are considered, the presence of the  $\mathcal{O}$  symmetry renders the effects of the crystalline symmetries trivial.

Before proceeding to the 2D cases, we here summarize what we learned from the 1D models, and how this will help us explore the 2D cases. First of all, we discussed that a system in the presence of a MHC with a spatially varying magnetic moment  $|M_{\parallel}| \neq |M_{\perp}|$  cannot be directly mapped onto the ISB SOC mechanism in Figs. 1(a)–1(d), i.e., one cannot gauge away the spatial dependence of the MHC. Hence, one needs to adopt either a sublattice description (cf. Appendix A), or perform a downfolding to the MBZ. The latter serves as a convenient basis for our calculations, and is adopted in the upcoming paragraphs. In this regard, the 1D cases additionally served as an introduction and motivation for our formalism in the more complicated 2D systems.

Concerning the topological classification, we established that 1BMs and 2BMs in the MHC phase generally reside in the BDI symmetry class, regardless of the type of spin-singlet pairing gap. However, by considering interband-only magnetic scattering, we found that the 2BMs display an emergent unitary symmetry ultimately resulting in the class AIII  $\oplus$  AIII. This class supports AZMs, which, however, can be converted back to MZMs by including intraband terms. Lastly, we also performed the topological classification in the presence of magnetic point- and space-group symmetries, introduced the relevant invariants, and discussed how these can lead to new topological phases. For 1D systems, the additional unitary symmetries proved to be obsolete when it comes to the prediction of edge modes since edges generally break these. Nonetheless, their presence sets constraints on a number of bulk topological properties which can be harnessed to experimentally infer the TSC phase of the system. In fact, the methodology employed in the study of unitary symmetries sets the stage and introduces the concepts for the upcoming 2D cases, where magnetic point-group symmetries play instead an essential role in determining the type of Majorana or Andreev edge modes.

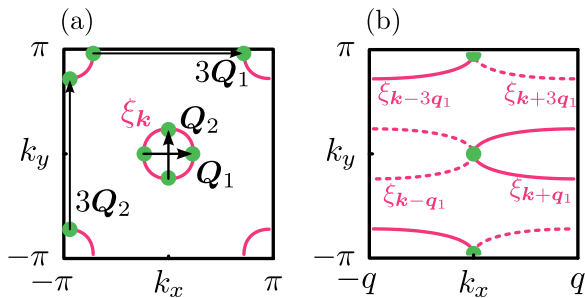


FIG. 7. Example of a 1BM in 2D. (a) Fermi surfaces (FSs) in the BZ obtained for a dispersion  $\xi_{\mathbf{k}} = -2t \cos k_x \cos k_y - \mu$  with  $\mu = -\sqrt{2}t < 0$ . We show the magnetic ordering wave vectors  $\mathbf{Q}_{1,2} = Q[\hat{x}, \hat{y}]$  and  $3\mathbf{Q}_{1,2} \equiv -\mathbf{Q}_{1,2}$  connecting points of the FS. (b) Depicts the resulting four FS segments after transferring to the MBZ for a MHC with the wave vector  $\mathbf{Q}_1$ . Similar to Fig. 3, also here there exist points at higher energy which are connected by  $\mathbf{Q}_{1,2}$ .

## V. 2D TOPOLOGICAL SUPERCONDUCTORS

We now extend our study to the case of 2D systems, which is the main topic on our agenda. We start with 1BMs and afterwards consider two-band extensions. We find that 2D systems exhibit a rich variety of MF-edge-mode types, i.e., flat, unidirectional, and bidirectional modes when nodes are present in the bulk energy spectrum or quasi-helical, helical, and chiral modes when the bulk energy band structure is fully gapped. This MF diversity is obtained by considering 1BMs and 2BMs in the presence of a MHC, a  $\text{SWC}_4$ , and, finally, a  $\text{SWC}_4$  combined with an external in- and out-of-plane Zeeman field, where the latter situation also reproduces a  $\text{SSC}_4$  phase.

### A. One-band models

In this section we extend the 1BM dispersion  $\xi_{k_x}$  to its 2D analog  $\xi_{\mathbf{k}}$ , with a focus on models leading to two hole pockets centered at  $\Gamma(0, 0)$  and  $M(\pi, \pi)$ . The two pockets are assumed to feature intrapocket FS nesting at the mutually orthogonal wave vectors  $\mathbf{Q}_{N,1}$  and  $\mathbf{Q}_{N,2}$ , thus generally supporting both single- $\mathbf{Q}$  and double- $\mathbf{Q}$  magnetic phases [134]. The magnetic vectors  $\mathbf{Q}_{1,2}$  may coincide with the nesting wave vectors. Such a type of band structure is shown in Fig. 7, and bears qualitative similarities to substantially hole-doped FeSCs. In principle, for highly symmetric FSs other nesting vectors may play a substantial role in deciding the resulting magnetic phase. Nonetheless, for the explorative nature of this paper we simply restrict to the star  $\pm\mathbf{Q}_{1,2}$ .

#### 1. MHC texture: Majorana flat bands

The construction of the Hamiltonian in 2D is straightforward, and is obtained by replacing the 1D dispersion in Eq. (24) by its 2D analog. The MBZ is now defined as the set  $\mathbf{k} \in (-q, q) \times (-\pi, \pi)$  and the ISPs are  $\mathbf{k}_{\mathcal{I}} = \{(0, 0), (q, 0), (0, \pi), (q, \pi)\}$ , where  $\mathbf{q}_{1,2} = \mathbf{Q}_{1,2}/2$  and  $q = |\mathbf{q}_{1,2}|$ . Out of these four,  $(q, 0)$  and  $(q, \pi)$  observe a Kramers degeneracy imposed by the antiunitary magnetic space-group symmetry  $\hat{\Theta}_{\mathbf{k}} = \{\mathcal{T} | (\pi/q, 0)\}$ .

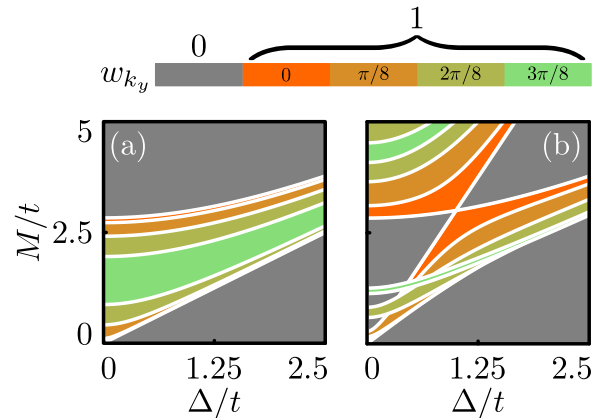


FIG. 8. (a), (b) Topological phase diagrams for the 2D IBM in Fig. 7, in the presence of a MHC texture with spatially constant and varying ( $M_{\perp}/M_{\parallel} = 3$ ) moment, respectively. For a given  $k_y = 0, \pi/8, 2\pi/8, 3\pi/8$  value, we find one (no) MZMs per edge in the correspondingly colored (gray) regions.

The extension to 2D is complete after the addition of  $k_y$  as a second argument to  $h_{k_x}^{(s)}$  and  $\Delta_{k_x}^{(s)}$  defined in Eqs. (25)–(28), which leads to  $h_{\mathbf{k}}^{(s)}$  and  $\Delta_{\mathbf{k}}^{(s)}$ . Note, however, that this seemingly trivial extension leads to a dichotomy in regards with the behavior of  $\Delta_{\mathbf{k}}^{(s)}$  under mirror operations. Specifically, one can now distinguish two cases depending on whether  $\Delta_{\mathbf{k}}$  transforms according to the  $\{A_{1g}, B_{1g}\}$  or the  $\{B_{2g}, A_{2g}\} \equiv B_{2g} \times \{A_{1g}, B_{1g}\}$  IRs of  $D_{4h}$ .<sup>7</sup> Notably, pairing gaps transforming according to the former (latter) satisfy  $\sigma_{xz,yz}\Delta_{\mathbf{k}} = +\Delta_{\mathbf{k}}$  ( $\sigma_{xz,yz}\Delta_{\mathbf{k}} = -\Delta_{\mathbf{k}}$ ). While this difference does not diversify the BDI 2D symmetry classification for the two categories of pairing, it does lead to two distinct classifications in the HSPs depending on whether the magnetic and pairing point groups coincide or not. Below, we first focus on the 2D classification and study the influence of the magnetic point group at the end of this section.

In analogy to our previous analysis, we define the winding number for each  $k_y$  subsystem which, notably, for the BDI class in 2D defines a *weak*, instead of a strong, topological invariant [201,202]. Under the condition that  $\Delta_{\mathbf{k}}$  does not induce additional gap closings in the MBZ other than the ones appearing for  $\mathbf{k} = (0, k_y)$ , we obtain

$$w_{k_y} = \sum_{k_c} \text{sgn} \left( \Delta_{k_c, q_1}^+ \frac{d\xi_{k_c, q_1}^-}{dk_x} - \xi_{k_c, q_1}^+ \frac{d\Delta_{k_c, q_1}^-}{dk_x} \right) \Big|_{k_x=k_c} \times \frac{\text{sgn} \{ M^2 - [\Delta_{(k_c, k_y), q_1}^+]^2 - [\xi_{(k_c, k_y), q_1}^+]^2 \}}{2}, \quad (44)$$

where we considered  $M_{\parallel, \perp} = M > 0$ , exploited the property  $\xi_{-k_x, k_y} = \xi_{k_x, k_y}$ , and made use of the constraint on  $\Delta_{\mathbf{k}}$ . Evidently, the 1D criterion for a gap closing at a point  $k_c$ , for a given  $k_y$ , still holds, namely,  $M^2 = [\Delta_{(k_c, k_y), q_1}^+]^2 + [\xi_{(k_c, k_y), q_1}^+]^2$ .

<sup>7</sup>For example,  $\{A_{1g}, B_{1g}, B_{2g}\} \sim \{1, \cos k_x - \cos k_y, \sin k_x \sin k_y\}$ .

Thus, gap-closing points appear for  $(k_x = 0, k_y)$  and suitable values of  $k_y$ .<sup>8</sup>

In Fig. 8(a) we display topological phase diagrams for the model in Fig. 7, for various  $k_y$  values which are depicted using a  $k_y$ -dependent color scale. In the weak-coupling limit, and for generally different  $M_{\parallel,\perp}$ , each  $k_y$  subsystem is dictated by the familiar criterion in Eq. (31):

$$M_- < \sqrt{(\xi_{k_c; q_1}^+)^2 + (\Delta_{k_c; q_1}^+)^2} < M_+. \quad (45)$$

However, in contrast to Eq. (31), here, not all gap-closing points  $k_c$  are at the Fermi level, and this detuning introduces an effective chemical potential  $\xi_{k_c; q_1}^+$  in the above criterion. As expected, for  $k_y = 0$  we reproduce Eq. (31) after setting  $\Delta_k = \Delta$ . Figure 8(b) presents the arising topological phase diagram for a system in the MHC phase with  $|M_{\perp}| \neq |M_{\parallel}|$ . Clearly, the phase diagram becomes significantly modified as  $k_y$  varies, and the various topologically nontrivial regions generally overlap.

Based on the criteria for a gap closing at the various  $k_y$  values, we infer that the nodes in the bulk spectrum move along the  $k_x = 0$  line in the MBZ when varying the superconducting and magnetic gaps. This resembles a gapless-gapful transition in topological insulators which leads to a Weyl semimetallic phase [203]. In fact, such transitions have also been studied previously in (i)  $p \pm ip$  TSCs, where an in-plane magnetic field drives the transition [174], (ii) in nodal  $d$ -wave SCs [175], and (iii) in nodal superconducting phases of FeSCs [204,205].

In Fig. 9(a) we sketch the path followed by the nodes in the MBZ when varying the superconducting and magnetic gaps. Given the structure of the weak topological invariant  $w_{k_y}$ , we expect to find topologically protected MF modes at the edges parallel to the  $y$  direction, but no modes at the edges perpendicular to it. This is indeed verified in Figs. 9(c) and 9(d), where we plot the spectrum with open boundary conditions along the  $x$  and  $y$  direction, respectively. Here, only the former edge spectrum displays topologically protected MF modes. This behavior is reminiscent of graphene and the appearance of flat bands only when the termination is of the zigzag type [206]. We observe that nodes related to each other by the discrete symmetries  $\Theta$  and  $\Xi$  are connected by Majorana flat bands (MFBs), in agreement with the values of  $w_{k_y}$  shown in Fig. 9(b). In the direct-lattice representation, these MFBs manifest as standing MF waves only at edges parallel to the  $y$  direction, i.e., they possess wave functions with a spatial part proportional to  $\sin(n\pi R_y/N_y)$  where  $n \in \mathbb{N}^+$  and  $N_y$  being the number of lattice sites in the  $y$  direction (cf. Ref. [207]).

So far, we studied the emergence of the MFBs by viewing  $k_y$  as a mere parameter which controls the topological properties of each 1D  $k_y$  subsystem. However, accounting for

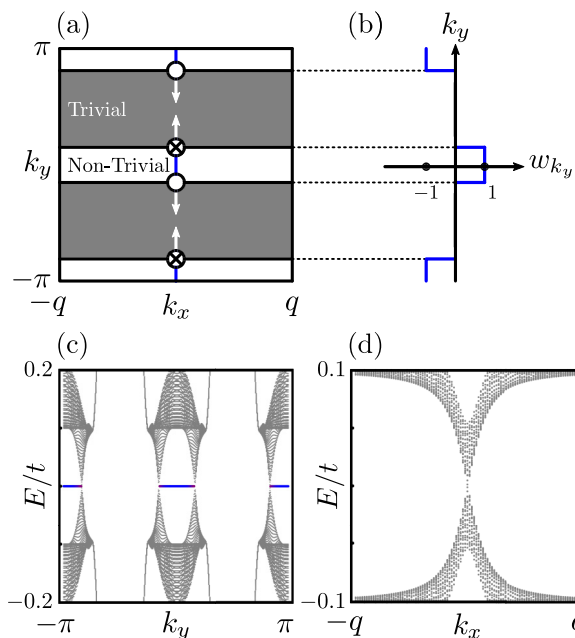


FIG. 9. Properties of the topologically stable nodes obtained in the gapless bulk energy spectrum of the IBM in Fig. 7 in the presence of the MHC texture. Here, nodes with vorticity  $v = +1$  ( $v = -1$ ) are discerned by a dot (cross). (a) Sketch of the path followed by the nodes when varying the superconducting and/or magnetic gaps. Nodes of opposite vorticities are connected by MFBs, in agreement with the winding number values in (b). (c), (d) Numerically obtained dispersions with open boundary conditions along the  $x$  and  $y$  direction, respectively. Parameter values used:  $\Delta = 0.1t$ ,  $M_{\perp} = M_{\parallel} = 0.2t$ , and  $L_{x,y} = 401$  sites in the  $x, y$  direction.

the correspondence of  $k_y$  to the spatial coordinate  $y$ , and considering the stable character of the nodes in the bulk energy spectrum, allows us to characterize the 2D nodal TSC using *local* strong topological invariants [208–210]. In fact, the BDI symmetry class ensures that the MFBs enjoy a topological protection, which is inherited from the respective robustness of the bulk nodes in the energy spectrum. Each node at  $k_c$  possesses a  $\mathbb{Z}$  topological charge, i.e., its vorticity

$$v = \frac{1}{2\pi i} \oint_{\mathcal{C}} \frac{dz_k}{z_k}, \quad (46)$$

where  $\mathcal{C}$  is a contour encircling the node. Here,  $z_k$  corresponds to the 2D extension of Eq. (9).<sup>9</sup>

<sup>9</sup>The apparent similarity of the invariants in Eqs. (10) and (46) is not accidental. In the 2D case, the  $k_y$  dependence of the dispersion can be viewed as a parameter that effectively controls the chemical potential of the 1D system. By deforming the contour  $\mathcal{C}$  to two parallel lines at  $k_y = k_c + 0^{\pm}$ , which “close” at infinity  $|k_x| \rightarrow \infty$ , the vorticity is given by the difference of the winding numbers  $w(\mu_c^{\pm})$ . Here,  $\mu_c$  corresponds to the  $k_c$  which tunes the system to the gap closing. Therefore, the vorticity defined in 2D yields the difference between two winding-number values which characterize two topologically distinct phases of the 1D TSC across the gap closing which appears at the location  $(0, \mu_c)$  of the respective Berry singularity in  $(k_x, \mu)$  space [20].

<sup>8</sup>Note that the IBM presented in Fig. 7 features additional gap closings at  $(k_x, \pm\pi/2)$ . However, these solely stem from the next-nearest-neighbor character of the hopping term considered, and do not constitute universal properties. In fact, this band peculiarity can be removed by considering additional hopping matrix elements of a different range in the 2D version of Eq. (1).



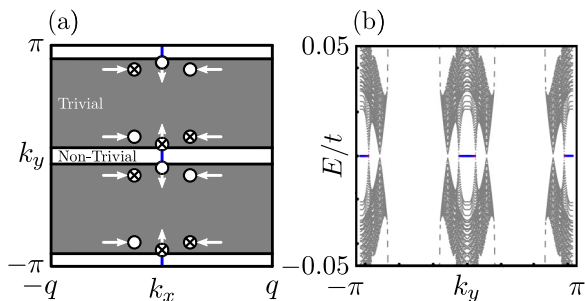


FIG. 10. Modification of the nodal spectrum in Fig. 9 due to the unconventional pairing function  $\Delta_{\mathbf{k}} = \Delta(\cos k_x - \cos k_y)$ . (a) The unconventional gap function induces eight additional nodes in the bulk spectrum. In (b) we present the energy spectrum for open boundary conditions along the  $x$  direction and  $L_x = L_y = 1001$ . We do not find any new MF bands since, for the given orientation of the termination edges, the contributions of the eight additional nodes cancel out. Parameter values used:  $\Delta = 0.1t$  and  $M_{\perp} = M_{\parallel} = 0.05t$ .

For the present model, linearizing the Hamiltonian about a node yields  $v = \text{sgn}(\alpha\beta\Delta\xi_{\mathbf{k}_c, q_1}^{\pm})$ , where we set  $\Delta_{\mathbf{k}} = \Delta$ , and expanded the shifted dispersions about  $\mathbf{k}_c$  as follows:  $\xi_{\mathbf{k}_c, q_1}^+ \approx \xi_{\mathbf{k}_c, q_1}^+ + \alpha k_y$  and  $\xi_{\mathbf{k}_c, q_1}^- \approx \beta k_x$ . The above result reveals that the vorticity is ill defined at the ISPs  $(0,0)$  and  $(0, \pi)$  since, there,  $\alpha = 0$ .<sup>10</sup>

Let us now proceed and consider a superconducting order parameter which *does* generate new nodal points. In order to determine the location of these new nodes, we employ the 2D analog of Eq. (33), which describes the low-energy features about the  $\Gamma(0,0)$  point in the MBZ. Alternatively, we can perform the shift  $\mathbf{k} \mapsto \mathbf{k} + 4\mathbf{q}_1$  to obtain a description about  $Y(0, \pi)$ . By repeating the steps detailed in Sec. IV A, the gap-closing points  $\mathbf{k}_c$  are given by  $\text{Im}[\det(A_{\mathbf{k}_c, \sigma}^{\text{low-en}})] = 0$  which yields the equation

$$\xi_{\mathbf{k}_c - q_1} \Delta_{\mathbf{k}_c + q_1} = \xi_{\mathbf{k}_c + q_1} \Delta_{\mathbf{k}_c - q_1}. \quad (47)$$

As an example, we consider the IBM of Fig. 7 and the  $d$ -wave gap function  $\Delta_{\mathbf{k}} = \Delta(\cos k_x - \cos k_y)$ . We find the gap-closing points  $\mathbf{k}_c : \{k_x = 0 \text{ or } \cos(2k_y) = -1 - \mu/t\}$ . For the given values of  $q$  and  $\mu$ , the additional nodes move on the lines  $k_y \simeq \pm 0.18\pi, \pm 1.18\pi$ . The complete information regarding the location of the above gap-closing points in the MBZ is found by further employing the remaining gap-closing condition  $\text{Re}[\det(A_{\mathbf{k}_c}^{\text{low-en}})] = 0$ , which is equivalent to the criterion in Eq. (45). Analyzing the above yields nodes moving along different lines in the MBZ, as shown in Fig. 10(a). Contrasting this to Fig. 9, we clearly see the introduction of eight new nodes in addition to the four nodes for  $k_x = 0$ . Here, however, we do not find any additional MF modes compared to Fig. 9(c) when we consider open boundary conditions along the main  $x, y$  axes, as is evident in Fig. 10(b) for open boundary conditions in the  $x$  direction. This is because the contributions of the additional nodes can-

cel out by virtue of mirror symmetries when projected onto the edge where translational invariance persists. However, if the system were to be terminated along the, e.g., (11) surface, that would indeed allow for the presence of new MF modes (cf. Ref. [205]).

We now consider the additional presence of the magnetic point- and space-group symmetries and the modifications that these bring to the topological classification. A common feature of the crystalline classifications in 1D and 2D for the MHC is that the effects of  $\mathcal{R}_{xz}$  are trivial in both. On the other hand, we find crucial differences which mainly relate to (i) the enhancement of the dimensionality which generally leads to different topological invariants even within the same symmetry class, and (ii) the structure of the pairing gap. Specifically, we find two distinct cases depending on whether  $\Delta_{\mathbf{k}}$  is invariant under the action of the magnetic point-group operations, or not. When  $\Delta_{\mathbf{k}} \in \{A_{1g}, B_{1g}\}$  ( $\Delta_{\mathbf{k}} \in \{B_{2g}, A_{2g}\}$ ), the magnetic point group  $M_{\text{MHC}}$  is (not) conserved. Notably, the pair of  $D_{4h}$  IRs bunched together in a given set are equivalent under the action of the magnetic point group.

Another key aspect of the crystalline classification in 2D is that the Kramers degeneracy imposed by  $\Theta_{\mathbf{k}}$  at  $(q, 0)$  and  $(q, \pi)$  extends to the entire  $k_x = q$  HSP. As discussed in Appendix B this is imposed by the pair of off-centered symmetries  $\mathcal{R}_{yz}$  and  $\{\sigma_{yz} | (\pi/q, 0)\}$ . Hence, MHC-driven gap closings cannot take place anywhere in the  $k_x = q$  HSP. Therefore, any possible crystalline topological features arising in this HSP originate from the structure of the pairing gap. For this reason, the remainder of this section focuses only on the  $k_x = 0$  HSP. The classification in the  $k_x = q$  HSP appears in Table II and the topological invariants connect to the analysis below.

For  $\Delta_{\mathbf{k}} \sim \{A_{1g}, B_{1g}\}$ ,  $\mathcal{R}_{yz}$  and  $\{\sigma_{yz} | (\pi/q, 0)\}$  lead to a  $\text{AI} \oplus \text{AI}$  class in the  $k_x = 0$  HSP. While a similar result was also encountered in Sec. IV A 2, here the topological consequences stemming from these symmetries differ because of the increased spatial dimensionality. Specifically, different topological features emerge only when the spectrum contains point nodes. In this case, the class  $\text{AI}$  allows defining an additional  $\mathbb{Z}$  crystalline topological invariant, which we denote  $\nu_{k_x}$ , and associate with the following vorticity in  $(\epsilon, k_y)$  space:

$$\nu_{k_x=0} = \frac{1}{4\pi i} \sum_{\sigma=\pm 1} \sigma \oint_{\mathcal{C}} \frac{dZ_{\epsilon, k_y, \sigma}}{Z_{\epsilon, k_y, \sigma}}, \quad (48)$$

with  $\mathcal{C}$  a path enclosing the node, and  $\sigma = \pm 1$  labeling the respective AI block.  $Z_{\epsilon, k_y, \sigma}$  is obtained in a similar fashion to Eq. (18). We remark that for the nodes shown in Fig. 9, we find  $|\nu_{k_x=0}| = |\nu| = 1$ .

The remaining two space-group symmetries, i.e.,  $\{\sigma_{xz} | (\pi/q, 0)\}$  and  $\{\mathcal{T} | (\pi/q, 0)\}$ , need to be treated more carefully since the former only leaves ISPs invariant, and thus does not introduce any changes to the topological classification in HSPs. The latter symmetry instead, combined with  $\Theta$ , leads to a class  $\text{BDI} \oplus \text{BDI}$  in the  $k_x = 0$  HSP. Hence, it only influences the topological properties of the system for a fully gapped spectrum since the BDI class cannot protect nodes in 1D [210]. Therefore, in the case of a full gap, we

<sup>10</sup>For the model in Fig. 7,  $v$  is also ill defined for  $k_y = \pm\pi/2$  since at these points  $\xi_{\mathbf{k}_c, q_1}^{\pm} = 0$  which, however, is only an artifact of the next-nearest-neighbor nature of the hopping considered.

define the glide winding number

$$w_{G,k_x=0} = \sum_{\sigma=\pm 1} \sigma w_{k_x=0,\sigma} \equiv \frac{1}{4\pi i} \sum_{\sigma=\pm 1} \sigma \int_{\text{BZ}} \frac{dz_{k_y,\sigma}}{z_{k_y,\sigma}}, \quad (49)$$

with  $w_{k_x=0,\sigma}$  corresponding to the winding number of each BDI class Hamiltonian block of Eq. (35), after the suitable  $k_y$  dependence is accounted for, and the respective normalized complex function  $z_{k_y,\sigma} = \det(\hat{A}_{k_x=0,k_y,\sigma}) / |\det(\hat{A}_{k_x=0,k_y,\sigma})|$  is constructed.

In contrast, when  $\Delta_{\mathbf{k}}$  transforms according to the IRs  $\{B_{2g}, A_{2g}\}$ , we find deviations from the above behaviors. Notably, the magnetic and pairing point groups differ since  $M_{\text{MHC}}$  acts on  $\Delta_{\mathbf{k}} \sim \{B_{2g}, A_{2g}\}$  as

$$\{E, C_2, \sigma_{xz}\mathcal{T}, \sigma_{yz}\mathcal{T}\}\Delta_{\mathbf{k}} = \{1, 1, -1, -1\}\Delta_{\mathbf{k}}. \quad (50)$$

Nevertheless, the sign-changing behavior of  $\Delta_{\mathbf{k}}$  under mirror operations still allows us to define a point group  $G_{\text{MHC}}$ , which is preserved by the total Hamiltonian and is isomorphic to  $M_{\text{MHC}}$ . This group consists of the elements

$$G_{\text{MHC}} = \{E, C_2, \sigma_{xz}^{\mathcal{Q}}\mathcal{T}, \sigma_{yz}^{\mathcal{Q}}\mathcal{T}\}, \quad (51)$$

with  $\sigma_{xz,yz}^{\mathcal{Q}} = \mathcal{Q}\sigma_{xz,yz}$ , where we introduced the dimensionless electric charge operator  $\mathcal{Q} = \tau_3$ . Such symmetries have also been previously discussed in connection to  $p$ -wave superconductors [20,211]. There, these ensure that the energy spectrum is inversion symmetric, despite the fact that inversion itself is not preserved. Similarly here,  $G_{\text{MHC}}$  ensures that the energy spectrum is invariant under the original  $M_{\text{MHC}}$  magnetic point group. Note also that the space-group symmetries  $\{\sigma_{xz,yz} | (\pi/\varrho, 0)\}$ , are correspondingly replaced by  $\{\sigma_{xz,yz}^{\mathcal{Q}} | (\pi/\varrho, 0)\}$ .

To infer the arising topological modifications, we block diagonalize the 2D extension of Eq. (24) according to the symmetry of interest. We immediately observe that the effects of  $\{\mathcal{T} | (\pi/\varrho, 0)\}$  and  $\{\sigma_{xz}^{\mathcal{Q}} | (\pi/\varrho, 0)\}$  in HSPs remain the same, with the latter only affecting ISPs once again. The presence of  $\mathcal{R}_{xz}^{\mathcal{Q}}$  establishes the class  $\text{AI} \oplus \text{AI}$  in the  $k_y = \{0, \pi\}$  HSPs, where however the pairing gap is zero. In these HSPs,  $\mathcal{R}_{xz}^{\mathcal{Q}}$  can only protect nodes, with a  $\mathbb{Z}$  invariant given by Eq. (48) after interchanging  $k_x$  and  $k_y$ , and considering  $k_y = \{0, \pi\}$ . The remaining two symmetries, i.e.,  $\{\sigma_{yz}^{\mathcal{Q}} | (\pi/\varrho, 0)\}$  and  $\mathcal{R}_{yz}^{\mathcal{Q}}$  lead to a  $\text{BDI} \oplus \text{BDI}$  class in the  $k_x = \{0, q\}$  HSPs. When the spectrum is fully gapped in these HSPs, one finds the glide  $w_{G,\text{HSP}}$  and mirror  $w_{M,\text{HSP}}$  winding numbers. These are correspondingly defined by, and in analogy to, Eq. (49). For details and concrete examples of the topological properties and the arising spectrum for a system with  $\Delta_{\mathbf{k}} \sim \{B_{2g}, A_{2g}\}$ , see Appendix C 6.

Closing this section, we point out that one can also introduce the BDI class weak  $\mathbb{Z}$  invariants for  $k_x$  points with a fully gapped spectrum. These are given by the winding numbers  $w_{k_x}$ , which are defined in an analogous manner to  $w_{k_y}$  in Eq. (44). The  $w_{k_x}$  invariants are expected to be particularly relevant when  $\Delta_{\mathbf{k}} \sim \{B_{2g}, A_{2g}\}$ . This is because, for a fixed  $k_x$ , the resulting pairing gap becomes effectively of the  $p_y$ -wave type (cf. Appendix C 6).

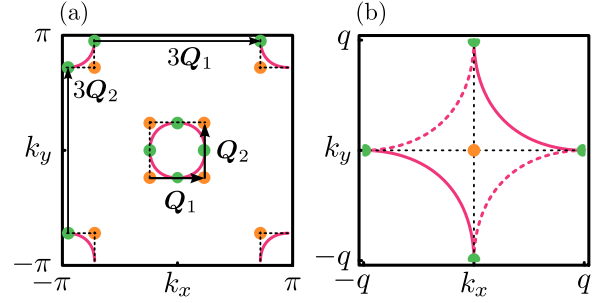


FIG. 11. 2D 1BM of Fig. 7 with a double- $\mathcal{Q}$  magnetic texture. (a) FSs of the 1BM in the first BZ. We show the magnetic ordering wave vectors  $\mathcal{Q}_1$  ( $3\mathcal{Q}_1 \equiv -\mathcal{Q}_1$ ) and  $\mathcal{Q}_2$  ( $3\mathcal{Q}_2 \equiv -\mathcal{Q}_2$ ), connecting points at the Fermi level (green dots). As in the 1D case (cf. Fig. 3), points at higher energies are also connected by  $\mathcal{N}_{1,2}$ , which upon increasing the magnetic energy scale give rise to nodes whose locations trace the dotted black lines. (b) Resulting FS segments in the MBZ, where the points simultaneously experiencing magnetic scattering by both  $\mathcal{Q}_1$  and  $\mathcal{Q}_2$  (orange dots), are now centered at the  $\Gamma(0, 0)$  point.

## 2. $\text{SWC}_4$ phase: Majorana bidirectional edge modes

In this section, we consider the case of a double- $\mathcal{Q}$  magnetic texture, with the ordering wave vectors depicted in Fig. 11(a). Here, we focus on the  $\text{SWC}_4$  profile which couples to the electrons through the exchange term

$$H_{\text{mag}} = \sum_n \psi_n^\dagger [M_\perp \cos(\mathcal{Q}_1 \cdot \mathbf{R}_n) \sigma_z + M_\parallel \sin(\mathcal{Q}_1 \cdot \mathbf{R}_n) \sigma_x + M_\perp \cos(\mathcal{Q}_2 \cdot \mathbf{R}_n) \sigma_z + M_\parallel \sin(\mathcal{Q}_2 \cdot \mathbf{R}_n) \sigma_y] \psi_n. \quad (52)$$

The double- $\mathcal{Q}$  structure of the magnetic texture implies that the MBZ is obtained by folding in both  $k_x$  and  $k_y$  directions of the original BZ, and is defined as  $\mathbf{k} \in (-q, q] \times (-q, q]$ . The ISPs span the set  $\mathbf{k}_{\mathcal{I}} = \{\Gamma(0, 0), X(q, 0), Y(0, q), M(q, q)\}$ . To proceed, we employ the wave-vector-transfer Pauli matrices  $\eta$  and  $\rho$  related to foldings in the  $k_x$  direction, as in Sec. IV A 2, and the Pauli matrices  $\lambda_{1,2,3}$  and  $\zeta_{1,2,3}$  related to foldings in the  $k_y$  direction, acting in  $\{\mathbf{k}, \mathbf{k} + \mathcal{Q}_2\}$  and  $\{\mathbf{k}, \mathbf{k} + 2\mathcal{Q}_2\}$  spaces, respectively. The resulting enlarged spinor reads as

$$\mathcal{X}_{\mathbf{k}}^{\text{1BM}, 2\text{D}} = \mathbb{1}_\zeta \otimes \frac{\lambda_2 + \lambda_3}{\sqrt{2}} (\mathcal{X}_{\mathbf{k}-q_2}^{\text{1BM}}, \mathcal{X}_{\mathbf{k}+q_2}^{\text{1BM}}, \mathcal{X}_{\mathbf{k}+3q_2}^{\text{1BM}}, \mathcal{X}_{\mathbf{k}-3q_2}^{\text{1BM}})^\text{T}, \quad (53)$$

where  $\mathcal{X}_{\mathbf{k}}^{\text{1BM}}$  is the 2D analog of Eq. (23). This yields the following class D ( $\Xi = \tau_2 \sigma_y \mathcal{K}$ ) bulk 2D Hamiltonian:

$$\hat{\mathcal{H}}_{\mathbf{k}} = \hat{F}(h_{\mathbf{k}}) \tau_3 + \hat{F}(\Delta_{\mathbf{k}}) \tau_1 - \frac{M_\perp (\mathbb{1} + \eta_1) \rho_1 \sigma_z + M_\parallel (\mathbb{1} - \eta_1) \rho_3 \sigma_x}{2} - \frac{M_\perp (\mathbb{1} + \zeta_1) \lambda_1 \sigma_z + M_\parallel (\mathbb{1} - \zeta_1) \lambda_3 \sigma_y}{2}, \quad (54)$$

where  $\hat{F}(h_{\mathbf{k}})$  and  $\hat{F}(\Delta_{\mathbf{k}})$  are defined in Appendix D.

The band dispersions and the magnetic part of the BdG Hamiltonian of Eq. (54) are invariant under the magnetic point group  $M_{\text{SWC}_4} = C_4 + (C_{4v} - C_4)\mathcal{T}$ , as well as the magnetic space-group operations  $\{\mathcal{T}, C_{4v} - C_4 | (\frac{\pi}{Q}, \frac{\pi}{Q})\}$ . See also Table I. Out of these five space-group symmetries, the antiunitary  $\tilde{\Theta}_k = \{\mathcal{T} | (\frac{\pi}{Q}, \frac{\pi}{Q})\} = ie^{i\pi(k_x+k_y)/Q}\lambda_2\rho_2\sigma_y\mathcal{K}$  defines a TR symmetry with  $\tilde{\Theta}_k^2 = -e^{i\pi(k_x+k_y)/Q}\mathbb{1}$ , and yields a Kramers degeneracy at  $\mathbf{k}_{\tilde{\Theta}_k} = \{\Gamma(0, 0), M(q, q)\}$ . The remaining space-group symmetries do not lead to any additional symmetry-protected degeneracies in the spectrum. See Appendix B for further clarifications.

Similar to the previous section, also here, the point group  $G_{\text{SWC}_4}$  preserved by the BdG Hamiltonian is decided by which *one* out of the possible four IRs  $\{A_{1g}, B_{1g}, B_{2g}, A_{2g}\}$ , is stabilized for  $\Delta_k$ . In a one-to-one correspondence to these four IRs, we find the scenarios

$$G_{\text{SWC}_4}^{A_{1g}} = \{E, C_2, 2C_4, 2\sigma_v\mathcal{T}, 2\sigma_d\mathcal{T}\}, \quad (55)$$

$$G_{\text{SWC}_4}^{B_{1g}} = \{E, C_2, 2C_4^Q, 2\sigma_v\mathcal{T}, 2\sigma_d^Q\mathcal{T}\}, \quad (56)$$

$$G_{\text{SWC}_4}^{B_{2g}} = \{E, C_2, 2C_4^Q, 2\sigma_v^Q\mathcal{T}, 2\sigma_d\mathcal{T}\}, \quad (57)$$

$$G_{\text{SWC}_4}^{A_{2g}} = \{E, C_2, 2C_4, 2\sigma_v^Q\mathcal{T}, 2\sigma_d^Q\mathcal{T}\}. \quad (58)$$

In a similar fashion, depending on the IR of  $\Delta_k$ , we obtain four space-group symmetries generated by products of  $\{\mathbb{1} | (\pi/Q, \pi/Q)\}$  and the mirror operations preserved by  $\Delta_k$ . Note that the topological class remains D, irrespectively of the given point group  $G_{\text{SWC}_4}$ . As it is customary in this work, the effects of the point and space groups are presented at the end of the section.

For the IBM in Fig. 11, we find two pairs of nodes upon modifying the various parameters, as sketched in Fig. 12(a). These pairs move along mutually orthogonal HSPs in the MBZ as indicated by the white arrows in the figure. Specifically, as the magnetic gap increases, the nodes first emerge at the  $X(q, 0)$  and  $Y(0, q)$  points, and then move towards the  $\Gamma(0, 0)$  point of the MBZ.

Similar nodes emerged for a MHC texture in 2D (cf. Fig. 9). Hence, we expect that in this nodal regime, the topological properties stemming from a  $\text{SWC}_4$  texture are describable by superimposing the results originating from two MHC textures which wind in perpendicular spatial directions and different spin planes. In this sense, the underlying topological mechanism is essentially 1D and, as long as these nodes are present, we do not expect to obtain any genuine 2D topological superconducting phases. The latter become accessible only after the nodes meet at the  $\Gamma(0, 0)$  point and annihilate. However, the Kramers degeneracy enforced by  $\tilde{\Theta}_k$  prohibits that, thus imposing that *only nodal* TSC phases become stabilized by a  $\text{SWC}_4$  texture in such IBMs. Nonetheless, as we show in the next section, the consideration of additional perturbations which violate  $\tilde{\Theta}_k$  unlocks the possibility of gapped 2D topological superconducting phases.

We anticipate that the gapping of these nodes becomes possible by considering suitable perturbations of even infinitesimally weak strength. This is because class D does not protect nodes in 2D [210]. In fact, one would expect that the

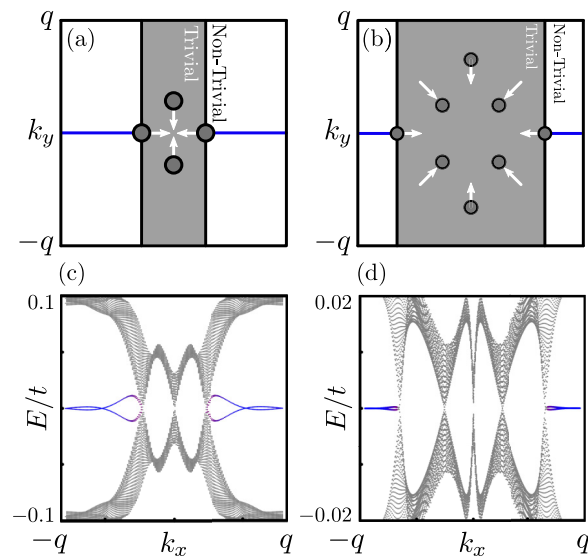


FIG. 12. (a), (b) Depict the paths swept by the pairs of nodes emerging in the bulk energy spectrum for the IBM in Fig. 7 in the  $\text{SWC}_4$  phase. In contrast to Sec. V A 1, the nodes here are not topologically protected as reflected by the gray shading of the dots. (c), (d) Show the related dispersions for open boundary conditions in the  $y$  direction. (a), (c) Obtained with  $\Delta_k = \Delta$  while for (b) and (d) we used the unconventional pairing gap  $\Delta_k = \Delta(\cos k_x - \cos k_y)$ . For the latter we have four additional nodes in the spectrum compared to case (a). Note also that the resulting MF modes in (d) are also lifted from zero energy away from ISPs, but with a much flatter dispersion compared to the surface bands in (c). All the figures were obtained for  $\Delta = 0.1t$  and  $L_x = L_y = 701$ , while in (c) and (d) we used  $M_\perp = M_\parallel = 0.2t$  and  $M_\perp = M_\parallel = 0.05t$ , respectively.

nodes could be protected by some crystalline symmetry, but as we find, this is also not the case. Let us further elaborate on this, through examining the impact of the crystalline symmetries on the topological classification. Each one of the  $(C_{4v} - C_4)\mathcal{T}$  symmetries acts as an effective TR symmetry in the HSPs that they leave invariant. Each TR symmetry operator in the HSPs squares to  $+1$ , thus establishing the BDI symmetry class in these high-symmetry lines. However, neither BDI class is capable of providing protection to nodes appearing in these HSPs. Lastly, as explained in Appendix B and Ref. [162], nonsymmorphic symmetries in 2D systems can only affect the classification at ISPs, and not in HSPs.

The absence of a topological protection for the nodes is reflected in the lack of MFBs in the energy spectrum obtained when open boundary conditions are imposed in one of the two main axes. Related numerical results for  $\Delta_k \sim \{1, \cos k_x - \cos k_y\}$  are discussed in Fig. 12, where we assume open boundary conditions in the  $y$  direction.<sup>11</sup> Remarkably, instead of MFBs we find MF edge modes with the distinctive feature that they do not have a fixed helicity or chirality. Even

<sup>11</sup>The particular choice of energy dispersion and pairing order parameter  $\Delta_k$  leads to an additional unitary symmetry and renders the spectra twofold degenerate. A weak violation of this symmetry gets the degeneracy lifted away from ISPs, but preserves the number of MF edge modes.

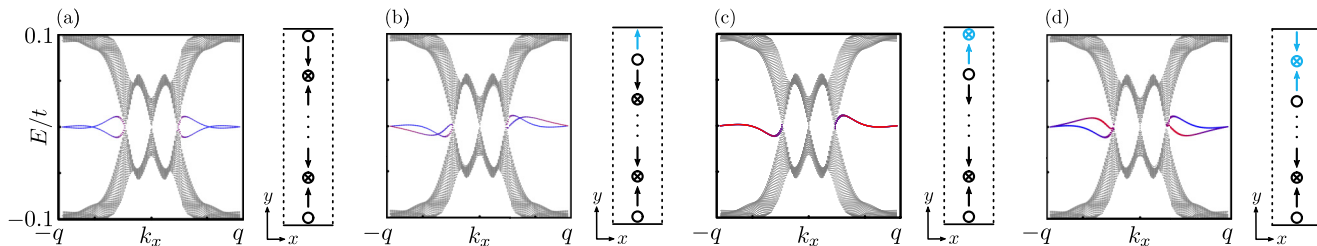


FIG. 13. Influence of crystal termination on the dispersion of the bidirectional MF edge modes in the 1BM in the  $SWC_4$  phase. All spectra were obtained with open boundary conditions along the  $y$  direction. The insets show the termination of the magnetic texture for (a)  $L_y = 701$ , (b)  $L_y = 702$ , (c)  $L_y = 703$ , and (d)  $L_y = 704$ . We see that only the termination in (a) leads to a symmetric spectrum since in (b)–(d) a net magnetization is accumulated at one edge (see cyan colored spin symbols). We used the parameter values  $\Delta = 0.1t$  and  $M_{\perp} = M_{\parallel} = 0.2t$ . The red and/blue color coding is defined as in Table II.

more remarkably, their spin character and group velocity are  $k_x$  dependent and become strongly affected by the type of crystal termination. See Ref. [162] for related findings, and Fig. 13 where we display the edge spectrum in Fig. 12 for various edge terminations. Clearly, we see that the local spin content on a given edge modifies the MF dispersion on that same edge. On these grounds, we here term this type of less familiar MF edge modes as *bidirectional*.

The properties of the bidirectional MF edge modes can be understood by viewing their presence as the outcome of the two coexisting MHCs. The MHC which winds spatially in the  $y$  direction gives rise to MFBs in the conserved  $k_x$  space, as long as the other MHC is completely neglected. In this ideal situation, one obtains a spectrum similar to the one of Fig. 9(c) after folding down to the MBZ. From this point of view, the secondary MHC mediates a  $BDI \rightarrow D$  symmetry-class transition for the 1D edge and, thus, lifts the protection of the MFBs. However, the presence of bidirectional MF edge modes is ensured by topologically protected degeneracies at ISPs.

The emerging 1D physics implies that there should be suitable topological invariants that encode the presence of a persistent degeneracy at  $k_x = q$ , thus enforcing the presence of the bidirectional MF edge modes. These are no other than the  $\mathbb{Z}_2$  weak invariants of class D, which correspond to the Majorana numbers  $\mathcal{M}_{k_x, y=q}$  [19, 149]:

$$\mathcal{M}_{k_x=q(k_y=q)} = \text{sgn} \prod_s^{X, M(Y, M)} \text{Pf}(\hat{B}_{k_s}), \quad (59)$$

where  $\text{Pf}(\hat{B}_{k_s})$  is the Pfaffian of the skew-symmetric matrix  $\hat{B}_{k_x} = \hat{U}_{\Xi} \hat{H}_{k_x}$ , where  $\Xi = \hat{U}_{\Xi} \mathcal{K}$ , with  $\hat{U}_{\Xi} = \tau_2 \sigma_y$ . The presence of a  $C_4$ -symmetric energy spectrum further renders the two invariants equal. Within the weak-coupling limit, these are nontrivial for  $M_- < |\Delta_{k=0, q_{1,2}}^+| < M_+$ , which is satisfied only after a simultaneous gap closing takes place at  $X(q, 0)$  and  $Y(0, q)$ . This mechanism stabilizes the degeneracies at the edge ISPs.

Alternatively, as a consequence of the antiunitary magnetic point-group elements  $(C_{4v} - C_4)\mathcal{T}$ , each HSP resides in the 1D BDI class, for which one can calculate the ensuing mirror winding number in 1D,  $\tilde{w}_{M, \text{HSP}}$ , similar to the weak invariant  $w_{k_x, y}$  for the MHC models in 2D.  $\tilde{w}_{M, \text{HSP}}$  is a crystalline topological invariant which is distinct from previously discussed

mirror invariants in this paper, in the sense that the symmetries  $(C_{4v} - C_4)\mathcal{T}$  do not induce any block-diagonal structure of the Hamiltonian in their respective HSPs, but rather an emergent TR symmetry. Note lastly that the invariants for the  $k_{x, y} = q$  HSPs fulfill the relation  $\mathcal{M}_{k_{x, y}=q} = (-1)^{\tilde{w}_{M, \text{HSP}}}$ .

### 3. $SWC_4$ texture: Genuine 2D TSCs

As we pointed out in the previous section, the Kramers degeneracy that the  $\tilde{\Theta}_k$  symmetry imposes at the  $\Gamma(0, 0)$  point of the MBZ does not allow the nodes moving along the  $\Gamma X$  and  $\Gamma Y$  lines to annihilate, therefore prohibiting the emergence of a fully gapped bulk energy spectrum and genuinely 2D topological superconducting phases. Nonetheless, a fully gapped bulk energy spectrum is obtainable in the presence of additional Hamiltonian terms which achieve at least one of the following two possibilities: (i) either preserve  $\tilde{\Theta}_k$  but enforce the nodes to meet and annihilate away from the Kramers degenerate points of the MBZ, i.e., away from  $k_{\Theta} = \{\Gamma(0, 0), M(q, q)\}$ , or (ii) violate  $\tilde{\Theta}_k$ .

In Fig. 14, we present a situation in which the former scenario takes place. In this case, the addition of a term proportional to  $\sin k_x \sin k_y$  to the dispersion preserves  $\tilde{\Theta}_k$  but violates  $C_4$  symmetry. As a result, the nodes intersect away from  $\Gamma(0, 0)$  and annihilate, therefore allowing for a chiral

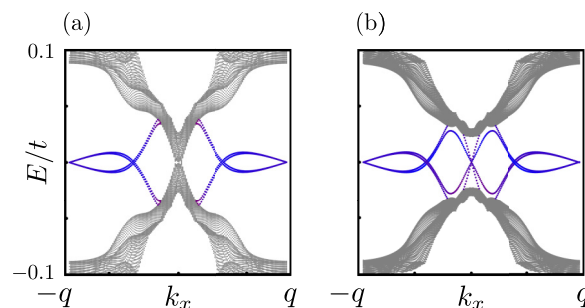


FIG. 14. (a) The nodal spectrum at  $\Gamma(0, 0)$  is protected by  $\tilde{\Theta}_k$  for the 1BM in Fig. 7 in the  $SWC_4$  phase. (b) Resulting fully gapped bulk spectrum for a broken  $C_4$  symmetry due to a nematic dispersion  $\xi_k^{\text{nem}} = \xi_k + t_{\text{nem}} \sin k_x \sin k_y$ , where  $\xi_k$  is the dispersion used in (a). In the fully gapped phase the preexisting bidirectional MF modes in (a) get accompanied by chiral MF modes. The figures were obtained using  $L_x = L_y = 1001$ ,  $\Delta_k = \Delta = 0.1t$ ,  $M_{\parallel} = M_{\perp} = 0.3t$ , and  $t_{\text{nem}} = 0.2t$ .

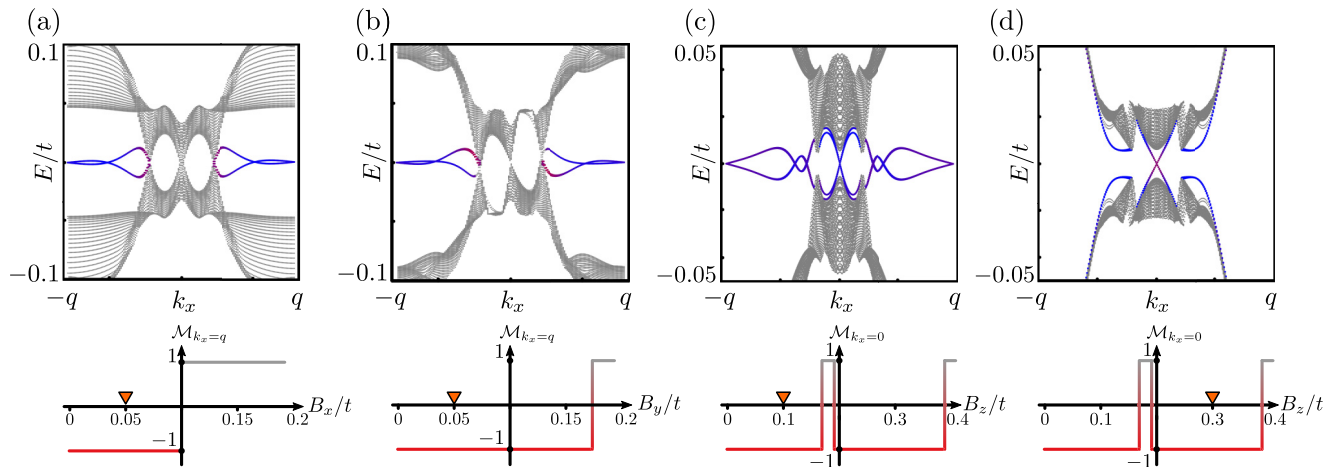


FIG. 15. The effects of Zeeman and exchange fields on the 1BM in Fig. 7 in the  $\text{SWC}_4$  phase. (a) [(b)] Spectrum with the field in the  $x$  ( $y$ ) direction with strength  $0.05t$ . (c) Displays the effect of a field oriented in the  $z$  direction, thus, giving rise to a  $\text{SSC}_4$  phase in the sufficiently weak  $B_z$  regime. Here the field does not lower the magnetic point-group symmetry of the system, but it does lift the unprotected nodes of the bulk spectrum. Here we used  $B_z = 0.1t$ . (d) Chiral edge modes for  $B_z = 0.3t$ , which become accessible only after a band inversion at  $\Gamma(0, 0)$  takes place. For all figures we display the numerically calculated Majorana number (59) as a function of the magnetic field for the different cases. The invariant  $\mathcal{M}_{k_x=0}$  in (c) and (d) is obtained by replacing  $(X, M)$  with  $(Y, \Gamma)$  in Eq. (59), and allows us to infer the transition to the chiral TSC phase without residing to the calculation of the related first Chern number  $\mathcal{C}_1$ . The red and blue color coding is defined as in Table II. All figures were obtained with open boundary conditions in the  $y$  direction and  $\Delta_k = \Delta = 0.1t$ ,  $M_{\parallel} = M_{\perp} = 0.2t$ , and  $L_x = L_y = 1001$ .

TSC. The second possibility is examined in the following section and is implemented by considering the presence of a constant Zeeman field  $\mathbf{B}$ , which is added to the Hamiltonian via the term  $\mathbf{B} \cdot \boldsymbol{\sigma}$ .

Depending on the orientation of the Zeeman field, the magnetic point- and space-group symmetries can be fully or partially violated, thus, also affecting the type of the accessible dispersive MF edge modes. Specifically, we find that an in-plane Zeeman field leads to unidirectional (bidirectional) MF edge modes when its direction is parallel (orthogonal) to the translationally invariant termination edge. In contrast, an out-of-plane field preserves the bidirectional character of the edge modes. We insist that such edge modes and ISP degeneracies are still accessible even when the crystalline symmetries are all broken since these are protected by the weak invariants defined in Eq. (59), which still remain valid.

Apart from the above-mentioned topological superconducting phases which have an underlying 1D character, the application of an out-of-plane field converts the  $\text{SWC}_4$  phase into a  $\text{SSC}_4$  for appropriate parameter regimes, and enables fully gapped chiral topological superconducting phases. These are topologically equivalent to a  $p + ip$  TSC, and are classified according to the first Chern number  $\mathcal{C}_1$  of the occupied bands [20].

Concluding this section, we remark that the introduction of the above perturbations is expected to influence the structure of the considered magnetic texture when the latter is treated in a self-consistent manner. However, sticking to the spirit of the explorative nature of this work, we neglect these modifications as they do not qualitatively modify the topological properties.

#### 4. $\text{SWCB}_2$ texture: Majorana unidirectional and bidirectional edge modes

An in-plane Zeeman field with a direction which is not aligned with the main or diagonal axes defined by the HSPs  $\{xz, yz, d_{\pm z}\}$  leads to the complete violation of the magnetic point- and space-group symmetries. In this case, it is the weak class D  $\mathbb{Z}_2$  invariants which predict the appearance of protected MZM crossings at edge ISPs independently of the orientation of the termination edge. However, considering a magnetic field which is aligned with one of these axes still allows for a nontrivial magnetic point group. For a Zeeman field in the  $x$  ( $y$ ) direction, the resulting magnetic point group becomes  $M_{\text{SWCB}_2} = \{E, \sigma_{xz}\mathcal{T}\}$  ( $M_{\text{SWCB}_2} = \{E, \sigma_{yz}\mathcal{T}\}$ ), while the symmetry  $\{\sigma_{yz(xz)} | (\frac{\pi}{Q}, \frac{\pi}{Q})\}$  also remains intact. See also Table I. Hence, now, by virtue of the TR symmetry  $\sigma_{xz, yz}\mathcal{T}$  acting in the respective HSP, one can also define the BDI class mirror winding number  $\tilde{w}_{M, \text{HSP}}$ .

In Figs. 15(a) and 15(b) we present the edge spectra for a  $B_x$  and a  $B_y$  Zeeman field, respectively, with the system being open in the  $y$  direction in both cases. By evaluating the respective weak invariant, we find protected degeneracies at the edge ISPs  $k_x = \{0, q\}$ . These persist until a gap closing takes place, which occurs for a Zeeman-field value which depends on its orientation. Moreover, we observe the appearance of dispersive MF edge modes. In the open-system geometry of Fig. 15(a), the antiunitary mirror symmetry implies that every state vector  $\phi_{n, k_x}$  corresponding to energy  $E_{n, k_x}$  possesses a mirror partner  $\sigma_{xz}\mathcal{T}\phi_{n, k_x}$  with energy  $E_{n, -k_x}$ , therefore resulting in a mirror-symmetric spectrum. In contrast, the emergent antiunitary mirror symmetry  $\sigma_{yz}\mathcal{T}$  in Fig. 15(b) relates a state

vector  $\phi_{n,k_x}$  with itself, thus allowing for a mirror-asymmetric spectrum and the emergence of unidirectional modes [see Fig. 15(b)].

### 5. SWCB<sub>4</sub> texture: Majorana bidirectional and chiral edge modes

In the case of an out-of-plane  $B_z$  field, the resulting SWCB<sub>4</sub> texture possesses nontrivial topological properties itself. Indeed, it has been shown [134] that SWCB<sub>4</sub> is equivalent to a SSC<sub>4</sub> texture for  $|B_z| < 2|M_\perp|$ . This allows us to establish a connection to prior works [87,212–216] which have focused on the emergence of chiral topological superconducting phases in other magnetic platforms. The above criterion also implies that, for  $|B_z| > 2|M_\perp|$ , SWCB<sub>4</sub> transforms into a ferromagnetic profile, which is expected to render the system trivial.

In connection to the detailed topological classification presented in the previous section for the SWC<sub>4</sub> phase, we observe that the addition of the  $B_z$  field leaves the magnetic point group  $M_{\text{SWC}_4}$  intact, but lifts the  $\hat{\Theta}_k$  and the space-group symmetries  $\{C_{4v} - C_4 | (\frac{\pi}{Q}, \frac{\pi}{Q})\}$ . As a consequence, the classification of the SWCB<sub>4</sub> texture follows from the classification performed for the TSCs induced by a SWC<sub>4</sub> magnetic texture. Indeed, we find that the presence of the  $B_z$  field still allows for MF edge modes crossings at ISPs, as seen in Fig. 15(c). By evaluating the respective weak Majorana number, we find that for higher values of the external magnetic field  $B_z \sim 0.2t$ , the edge-mode crossings at ISPs get lifted, while a band inversion at  $\Gamma(0,0)$  takes place for slightly higher values of the field strength. Remarkably, the latter gives rise to two chiral MF edge-mode branches as displayed in Fig. 15(d). The emergence of this chiral topological superconducting phase is also described by the Chern number  $|\mathcal{C}_1| = 2$ . Note that the Chern-number value  $|\mathcal{C}_1| = 1$  is also generally accessible, as long as the accidental symmetry discussed in Footnote 11 becomes lifted.

We now summarize the key results for 1BMs in 2D. For a MHC the energy spectrum is nodal and leads to MFBs. Moreover, the classification in HSPs strongly depends on the IR of the pairing term. Nodes emerge also for a SWC<sub>4</sub> but they are not topologically stable. Nonetheless, degeneracies at ISPs persist and give rise to weak and crystalline TSC phases, which result into bidirectional MF edge modes. In the SWC<sub>4</sub> case, a fully gapped spectrum is accessible only by violating  $C_4$  or TR symmetries. Indeed, including a Zeeman field leaves the bidirectional modes intact, converts them into unidirectional modes or opens a gap in the spectrum and stabilizes chiral Majorana edge modes.

### B. Two-band models

We now apply the classification methods discussed in the previous sections to 2D 2BMs. For an example of such a model see Fig. 16 which, for the chosen parameters, yields the FSs shown in Fig. 16(a). Interband FS nesting, with the two ordering wave vectors  $Q_{1,2}$ , takes place between the hole (fuchsia) and electron (navy blue) pockets. Hence, the system has the possibility to develop either a single- $Q$  or a double- $Q$  magnetic phase [134].

Recall from our previous discussion in Sec. IV B that a multiband system allows for an interplay of interband and

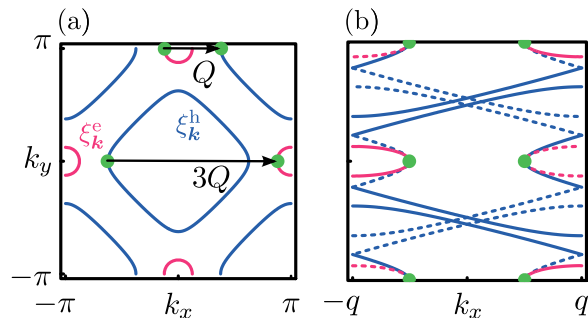


FIG. 16. Example of a 2BM in 2D, described by the dispersions  $\xi_k^h = t_h \cos k_x \cos k_y + t'_h [\cos(2k_x) + \cos(2k_y)] - \varepsilon_h$  and  $\xi_k^e = t_e \cos k_x \cos k_y - \varepsilon_e$ . We consider the parameters  $t_h = 2.86 t_e$ ,  $t'_h = t_e$ ,  $\varepsilon_e \simeq -0.92 t_e$ , and  $\varepsilon_h = -0.80 t_e$ . (a) FSs of the 2BM in the first BZ. For clarity we only show half of the magnetic ordering wave vectors  $Q$  and  $3Q = -Q$  connecting bands at the Fermi level. (b) FS segments for the 2BM in the MBZ for a MHC, where the nested points at the Fermi level are marked by green dots. Note that nested points at finite energy, away from the Fermi level, are also present.

intraband magnetic scattering, as well as for a here-assumed intraband pairing gap which is a matrix in band space  $\hat{\Delta}_k = (\Delta_k^e + \Delta_k^h)/2 + \kappa_3(\Delta_k^e - \Delta_k^h)/2$ . Even more importantly, we show here that the inclusion of the additional band may in many realistic situations enrich the symmetry of the system. As we discuss below, a number of features that become unlocked for 2BMs open perspectives for new phenomena and TSC phases.

#### 1. MHC texture: Majorana and Andreev flat bands

The present section builds upon the analyses of the 1D 2BMs and the 2D 1BMs under the influence of a MHC. In the general case, in which intraband and interband magnetic scatterings are present, the system is dictated by the same magnetic point- and space-group symmetries discussed in Sec. V A 1. The nodes in the bulk energy spectrum therefore possess a topological charge reflected in their vorticity  $\nu$ . Moreover, in HSPs one can also define the respective mirror vorticity  $\nu_{\text{HSP}} \in \mathbb{Z}$  following the definition in Eq. (48). By further assuming spatially constant pairing gaps  $\Delta^{e,h}$  for the two pockets, we find that the edge spectrum contains MFBs (see Fig. 17), whose topological protection can be genuinely described either by the strong local invariants mentioned above, or, by the weak invariant  $w_{k_y}$ .

As found previously for the 2BMs in 1D, the topologically stable bulk nodes and edge MFBs become accessible even for  $\Delta^e \Delta^h < 0$ , when intraband magnetic scattering is assumed. In Figs. 17(a) and 17(c) we display the resulting path of the nodes in the MBZ and spectrum, respectively, for  $\Delta^e = -\Delta^h$ . For the chosen values of interband and intraband scattering, the topological properties are essentially determined only by the hole pocket, thus exhibiting a similar phenomenology to Fig. 9(a), with the nodes moving on straight lines.

If instead we restrict to an interband-only magnetic texture, we find that almost all the features of the 2BMs in 2D are directly inherited from the 1D interband versions, namely, (i) the Hamiltonian is block diagonalizable into an AIII  $\oplus$  AIII fashion [see Eq. (42) and Fig. 17(b)],

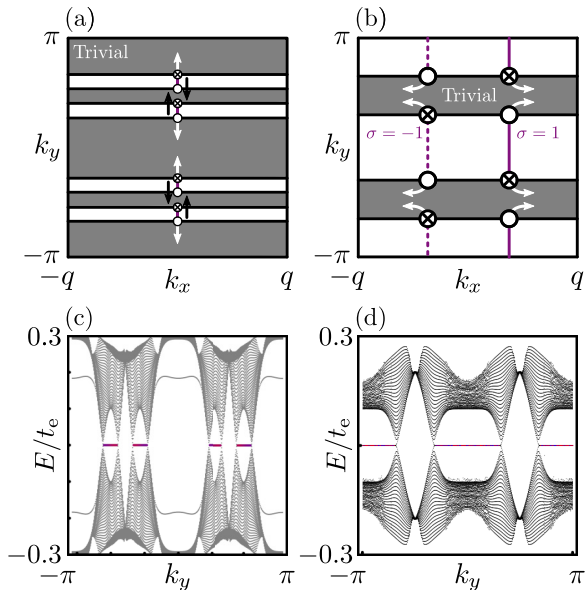


FIG. 17. Sketches of nodes and the numerically obtained dispersions for the 2BM of Fig. 16 in the MHC phase. (a), (c)  $\Delta^e = t_e$ ,  $\Delta^h = -t_e$ , and  $M_{||,\perp}^{eh} = M_{||,\perp}^e = M_{||,\perp}^h = 1.1 t_e$ . The nodes are moving on straight lines similar to the 1BM in 2D (cf. Fig. 9). The number of nodes has increased with the number of nested points (see green points in Fig. 16). (b), (d)  $\Delta^e = \Delta^h = t_e$ ,  $M_{||}^{eh} = M_{||}^e = 1.1 t_e$ , and  $M_{||,\perp}^e = M_{||,\perp}^h = 0$ . The nodes are now moving on arcs, due to the interband-only scattering mediated by the magnetic texture. Both dispersions are obtained with open boundary conditions along the  $x$  direction, and with  $L_x = L_y = 401$ . In (b)  $\sigma = \pm 1$  labels the two blocks of the Hamiltonian after performing the unitary transformation with the operator  $\mathcal{S}$  in Sec. IV B.

(ii) the number of gap-closing points  $\mathbf{k}_c$  and edge modes double compared to the 1BMs, (iii) the gap-closing points are found through the relation  $\xi_{\mathbf{k}\pm 3\mathbf{q}_1}^e \Delta^h = \xi_{\mathbf{k}\mp 3\mathbf{q}_1}^h \Delta^e$ , and (iv) nodal topological superconducting phases are accessible only for  $\Delta^e \Delta^h > 0$ .

All the above features are reflected in Figs. 17(b) and 17(d) where we display the path taken by the nodes upon variation of the magnetic and superconducting gaps, and the edge spectrum, respectively. Notably, here one obtains in most cases Andreev flat bands (AFBs), which extend the Andreev zero modes (AZMs) discussed in Sec. IV B to 2D. AFBs protected by the symmetry  $\sigma_{xz}^Q \mathcal{T} \Theta (\{ \mathcal{T} \Theta | (\frac{\pi}{Q}, 0) \})$  are also accessible in  $k_y = \{0, \pi\}$  for  $\Delta_{\mathbf{k}} \sim \{B_{2g}, A_{2g}\}$  (for  $\Delta_{\mathbf{k}}$  in any of the four  $D_{4h}$  IRs), in which case the symmetry class is  $\oplus_4 \text{AIII}$ , and the topological invariant is a mirror (glide) winding number  $w_{M,\text{HSP}}$  ( $w_{G,\text{HSP}}$ ). In contrast, MF excitations become possible only in crystalline TSC phases obtained for  $\Delta_{\mathbf{k}} \sim \{B_{2g}, A_{2g}\}$ , where the symmetry  $\sigma_{yz}^Q \mathcal{T}$  or  $\{ \sigma_{yz}^Q \Theta | (\frac{\pi}{Q}, 0) \}$  drives the symmetry-class transition  $\text{AIII} \oplus \text{AIII} \rightarrow \text{BDI} \oplus \text{BDI}$ , which in turn allows for MFs. These are protected by a mirror winding number  $\tilde{w}_{M,\text{HSP}}$ , which is similar to the weak invariant  $w_{k_x, y}$  for the 1BMs in 2D in the presence of a MHC. See Table III.

Notably, a very crucial difference compared to the 2D 1BM is that, here, the paths along which the bulk nodes move in  $\mathbf{k}$  space do not coincide with the main axes of the MBZ.

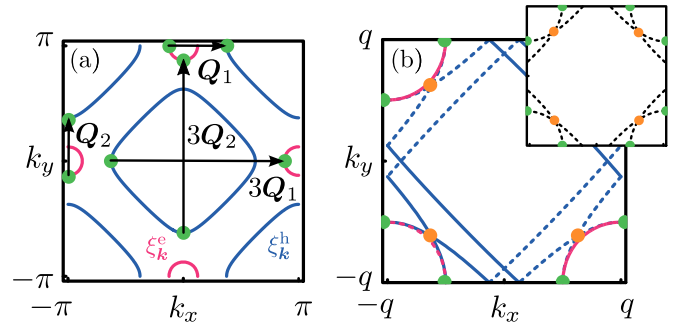


FIG. 18. 2BM of Fig. 16 under the influence of a double- $\mathbf{Q}$  magnetic texture. (a) FSs of the 2BM in the first BZ. We sketch the magnetic ordering wave vectors  $\mathbf{Q}_{1,2}$  ( $3\mathbf{Q}_{1,2} \equiv -\mathbf{Q}_{1,2}$ ), which connect points at the Fermi level (green dots). For clarity we only show half of the ordering wave vectors. (b) The resulting FS segments in the MBZ. As in Fig. 11, we also display the points connected by both  $\mathbf{Q}_1$  and  $\mathbf{Q}_2$  (orange dots) at energies away from the Fermi level. Inset: The dotted black lines show the gap-closing points  $\mathbf{k}_c$  in the MBZ.

Remarkably, here the nodes generally move on arcs, as indicated by the white arrows in Fig. 17(b). This enables the bulk nodes to meet and annihilate away from Kramers degenerate points, thus opening the perspective for fully gapped spectra for class D or DIII topological superconducting phases in the  $\text{SWC}_4$  phase. This implies that here strong 2D TSC phases seem to become accessible without the requirement of external perturbations, e.g., Zeeman fields, which was the case for 1BMs.

## 2. $\text{SWC}_4$ phase: Quasihelical Majorana edge modes

We now proceed by studying 2BMs with an *interband-only* double- $\mathbf{Q}$   $\text{SWC}_4$  texture. As in previous sections, we employ the usual set of wave-vector-transfer Pauli matrices  $\zeta$ ,  $\lambda$ ,  $\eta$ , and  $\rho$ , in order to account for the magnetic scattering taking place in the two orthogonal directions, as displayed in Fig. 18(a). The MBZ is displayed in Fig. 18(b), where points connected by a single- $\mathbf{Q}$  vector at the FS and points connected by both  $\mathbf{Q}$  vectors are marked by green and orange dots, respectively.

Due to the interband nature of the magnetic scattering the BdG Hamiltonian now enjoys a TR symmetry  $\Theta = \kappa_3 \mathcal{T}$ . This satisfies  $\Theta^2 = -\mathbb{1}$  and leads to Kramers pairs (KP) at all the ISPs of the MBZ, thus enlisting the BdG Hamiltonian in the DIII symmetry class. Nodes in the bulk spectrum of a DIII Hamiltonian are topologically stable only at ISPs, and are classified by a vorticity akin to the one in Eq. (46). For a fully gapped bulk spectrum, class DIII supports one strong and two weak  $\mathbb{Z}_2$  topological invariants [188,217–219], that we here construct as

$$\mathcal{M}^{\text{KP}} = \prod_s^{\Gamma, X, M, Y} \text{Pf}(\hat{\mathcal{W}}_{k_s}) / \sqrt{\det(\hat{\mathcal{W}}_{k_s})}, \quad (60)$$

$$\mathcal{M}_{k_x=q(k_y=q)}^{\text{KP}} = \prod_s^{X, M(Y, M)} \text{Pf}(\hat{\mathcal{W}}_{k_s}) / \sqrt{\det(\hat{\mathcal{W}}_{k_s})}. \quad (61)$$

In the above, we defined the skew-symmetric “sewing” matrix  $\hat{\mathcal{W}}_{\mathbf{k}_{\mathcal{I}}} \equiv \hat{\mathcal{U}}_{\Theta} \hat{A}_{\mathbf{k}_{\mathcal{I}}}$  at ISPs  $\mathbf{k}_{\mathcal{I}}$  only. The  $\hat{\mathcal{W}}$  matrix is the

DIII analog of the AII class sewing matrix introduced by Fu and Kane [220]. The difference is that, here,  $\hat{U}_\Theta = i\sigma_y$  corresponds to the unitary part of the block off-diagonal  $\Theta$ , obtained in the diagonal basis of the chiral symmetry operator  $\Pi$ . In this basis, we identify the block off-diagonal part of the Hamiltonian as  $\hat{A}_k$ . The transition to this basis is here effected via the transformation  $(\Pi + \tau_3)/\sqrt{2}$ , which brings the arising chiral symmetry generator  $\Pi = \kappa_3\tau_2$  into the form  $\Pi = \tau_3$ , and leads to

$$\begin{aligned} \hat{A}_k = & - \sum_s^{\text{e,h}} \mathcal{P}_s [\hat{F}(\Delta_k^s) + i\kappa_3 \hat{F}(h_k^s)] \\ & - \kappa_2 \frac{M_\perp(\mathbb{1} + \eta_1)\rho_1\sigma_z + M_\parallel(\mathbb{1} - \eta_1)\rho_3\sigma_x}{2} \\ & - \kappa_2 \frac{M_\perp(\mathbb{1} + \zeta_1)\lambda_1\sigma_z + M_\parallel(\mathbb{1} - \zeta_1)\lambda_3\sigma_y}{2}, \end{aligned} \quad (62)$$

with  $\mathcal{P}_{\text{e,h}}(\hat{F})$  defined once again as in Sec. IV B (Appendix D).

We now move on with the discussion of the various crystalline symmetries, which are identical to the ones dictating the 1BMs in Sec. V A 2. Specifically, the antiunitary mirror symmetries  $(C_{4v} - C_4)\mathcal{T}$  belonging to the related  $G_{\text{SWC}_4}$  point group discussed in Sec. V A 2, combine with  $\Theta$  and give rise to the unitary mirror operations  $\mathcal{R} = (C_{4v} - C_4)\mathcal{T}\Theta = \kappa_3(C_{4v} - C_4)$ . These lead to a AIII  $\oplus$  AIII (D  $\oplus$  D) class in the corresponding HSP when the pairing gap  $\Delta_k$  is even (odd) under the given mirror operation, e.g., for  $\Delta_k \in B_{1g}$  the symmetry class is AIII (D) in the  $xz$  ( $x = y$ ) and  $yz$  ( $x = -y$ ) HSPs. Both AIII and D classes are nontrivial in 1D for a fully gapped system. Thus, HSPs dictated by the symmetry class AIII  $\oplus$  AIII (D  $\oplus$  D) and at the same time exhibit a fully gapped spectrum, are characterized by a  $\mathbb{Z}$  ( $\mathbb{Z}_2$ ) mirror winding number  $w_{M,\text{HSP}}$  (mirror Majorana number  $\mathcal{M}_{M,\text{HSP}}$ ).<sup>12</sup> In contrast, nodes in HSPs dictated by either AIII  $\oplus$  AIII or D  $\oplus$  D are not protected.

On the other hand, nonsymmorphic symmetries can only influence the topological classification at ISPs. Remarkably, the  $\Gamma(0,0)$  and  $M(q,q)$  points are under the simultaneous influence of two TR symmetries which square to  $-\mathbb{1}$ , i.e.,  $\Theta = \kappa_3\mathcal{T}$  and  $\{\mathcal{T} | (\frac{\pi}{Q}, \frac{\pi}{Q})\}$ , thus observing a fourfold degeneracy. This can be understood in terms of the unitary symmetry  $\{\kappa_3 | (\frac{\pi}{Q}, \frac{\pi}{Q})\} = e^{i(k_x+k_y)\pi/Q}\kappa_3\lambda_2\rho_2$  which emerges at these two ISPs.<sup>13</sup>

We now investigate a concrete 2BM, specifically the model defined in Fig. 18. Similar to the analysis of the 1BMs in the  $\text{SWC}_4$  phase, we identify two types of MBZ points, namely, the points connected by a single- $\mathcal{Q}$  vector (green dots) and the points connected by both ordering wave vectors (orange dots) [cf. Fig. 18(b)]. Based on the results of the previous paragraphs, we find that the nodes move on arcs determined by the intersection of the two bands connected by a single-

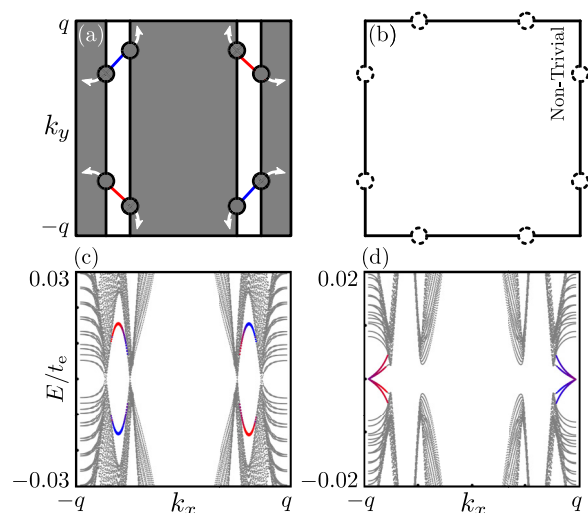


FIG. 19. Bidirectional and mirror-symmetry-protected quasi-helical Majorana edge modes for the 2BM in the  $\text{SWC}_4$  phase. (a) The bulk nodes move from the points connected by two  $\mathcal{Q}$  vectors [orange dots in Fig. 18(b)], and meet at points connected by a single- $\mathcal{Q}$  vector [green dots in Fig. 18(b)], as indicated by the white arrows. (c) The spectrum related to (a), with bidirectional Majorana edge modes ( $M_{\perp,\pm}^{\text{eh}} = 0.095 t_e$ ). Note that here the bidirectional MF modes are not topologically protected, due to the similar lack of protection seen by the bulk nodes. (b) Sketch of the MBZ after the nodes have met and annihilated at the points marked by the dotted circles. (d) Resulting quasi-helical edge modes connected to the sketch in (b), where we used  $M_{\perp,\pm}^{\text{eh}} = 0.11 t_e$ . For clarity, in (d), we show only the modes on a single edge since the  $z$ -spin axis electronic spin polarization of the modes on the other edge is exactly opposite. We note that both types of spectra are twofold degenerate for reasons discussed in Footnote 11. We used open boundary conditions in the  $y$  direction,  $\Delta^e = \Delta^h = 0.1 t_e$ ,  $M_{z,\pm}^{\text{e,h}} = 0$  and  $L_x = L_y = 501$ .

$\mathcal{Q}$  vector, e.g.,  $\xi_{k+3q_1-q_2}^e = \xi_{k-3q_1-q_2}^h$ . The paths of the nodes upon variations of the magnetic or superconducting gaps are marked by the black dotted lines in the inset of Fig. 18(b). Once again, bulk nodes appear strictly for  $\Delta^e\Delta^h > 0$  since we here consider an interband-only texture.

The presence of bulk nodes goes hand in hand with the emergence of bidirectional MF edge modes, as seen in Figs. 19(a) and 19(c) where we display the nodes and edge spectrum. However, in the present situation, the bulk nodes are not topologically protected, thus implying the same for the resulting bidirectional edge modes. Both nodes and edge modes are thus removable by considering additional Hamiltonian terms which do not modify the ensuing DIII class. Similar conclusions were drawn for the 1BMs in the  $\text{SWC}_4$ , with the crucial distinction that there the edge modes had a topologically protected crossing at  $k_{x,y} = q$ . Such protected crossings do not arise for the bidirectional MF modes in Fig. 19(c).

By increasing the energy scale of the magnetic gaps the nodes move on arcs, as indicated by the white arrows in Fig. 19(a), and meet up at the green points in the MBZ in Fig. 18(b), when the familiar criterion is satisfied  $\Delta^e\Delta^h = M_{\pm}^2$ . In contrast to the 1BMs, here the nodes *do* get lifted when they meet up since they intersect away from ISPs, as sketched

<sup>12</sup> $\mathcal{M}_{M,\text{HSP}}$  is defined as  $\mathcal{M}_{M,\text{HSP}} = \text{sgn} \prod_{\sigma} \mathcal{M}_{\sigma,\text{HSP}}$ , where  $\sigma = \pm 1$  labels the D  $\oplus$  D blocks. Each  $\mathcal{M}_{\sigma,\text{HSP}}$  follows from Eq. (59).

<sup>13</sup>Note that the above fourfold degeneracy does not lead to hourglass MFs. Following Ref. [162], we can attribute this to the commutation relation  $[\kappa_3 | (\frac{\pi}{Q}, \frac{\pi}{Q}), \Pi] = 0$  which holds here.



in Fig. 19(b). Beyond this point, the spectrum is fully gapped. In the present case, the fourfold degeneracies at  $\Gamma(0, 0)$  and  $M(q, q)$  additionally imply that, there,  $\text{Pf}(\hat{\mathcal{N}}_{k_x})$  features an even number of gap closings upon sweeping the various parameters. Hence, the above-mentioned invariants simplify as  $\mathcal{M}^{\text{KP}} = \mathcal{M}_{k_x=q}^{\text{KP}} \mathcal{M}_{k_y=q}^{\text{KP}}$  where  $\mathcal{M}_{k_x=q(k_y=q)}^{\text{KP}} = \text{sgn}[\text{Pf}(\hat{\mathcal{N}}_{k_x(y)})]$ . In the event of a  $C_4$ -symmetric energy spectrum, which is actually the case here, the two invariants are equal. The two weak Majorana Kramers pair (MKP) numbers generally become nontrivial simultaneously. Nonetheless, here we find that all three invariants remain trivial.

Despite the fact that the DIII invariants are here all trivial, in Fig. 19(d) we indeed find the here-termed quasihelical edge modes centered at  $k_x = q$ , which are protected by the mirror symmetry  $\sigma_{yz}\mathcal{T}$ . These come in pairs, and their electronic spin polarization is opposite on opposite edges, similar to what is encountered for their helical counterparts. However, the quasihelical ones appear only for edges preserving the respective mirror symmetry, in stark contrast to the helical edge modes stemming from the strong DIII invariant in 2D, which emerge for a termination of an arbitrary orientation. Since for the above numerical calculations we have considered  $\Delta_k^{e,h} \sim A_{1g}$ , the HSP plane is dictated by the  $\text{AIII} \oplus \text{AIII}$  symmetry class. On the other hand, considering a pairing gap  $\Delta_k^{e,h} \sim B_{2g}$  imposes the  $\text{D} \oplus \text{D}$  symmetry class in the  $k_x = q$  HSP, and allows instead for quasihelical Majorana edge modes protected by a mirror  $\mathbb{Z}_2$  invariant. The presence of two possible types of topological protection for the touching point further suggests a different behavior for the quasihelical Majorana edge modes in response to external perturbations, e.g., Zeeman fields.

### 3. Magnetic-field-induced TSC phases: Majorana unidirectional and bidirectional, quasihelical, and chiral edge modes

We complete the study of the 2BMs in 2D by considering the effects of an additional Zeeman field on the system discussed in the previous paragraph. In this case, the system undergoes the symmetry class transition  $\text{DIII} \rightarrow \text{D}$ . Therefore, for a fully gapped bulk energy spectrum, chiral edge modes become accessible. Even more, when the field is aligned with one of the HSPs, mirror-symmetry-protected edge modes are also possible. For a magnetic field in the  $x$  ( $y$ ) direction, the resulting magnetic point group becomes  $M_{\text{SWCB}_2} = E + \sigma_{xz}\mathcal{T}$  ( $M_{\text{SWCB}_2} = E + \sigma_{yz}\mathcal{T}$ ). HSPs now belong to the BDI symmetry class since the antiunitary elements of the point group act as TR symmetries. Hence, we can define the mirror winding numbers  $\tilde{w}_{M,\text{HSP}} \in \mathbb{Z}$  similarly to the weak winding numbers  $w_{k_{x,y}}$  introduced in Eq. (44).

For concreteness, below we focus on a system with open boundaries along the  $y$  direction, and assume that the pairing gap is nonzero in the  $xz$  and  $yz$  HSPs. For a magnetic field in the  $x$  direction, the TR symmetry  $\sigma_{xz}\mathcal{T}$  is not preserved by the termination, thus not protecting the quasihelical modes in the HSP. Evidently the quasihelical Majorana edge modes in Fig. 20(a) become lifted by the term  $B_x\sigma_x$ , as seen in Fig. 20(b). If we instead consider a field perpendicular to the edge, i.e., a nonzero  $B_y$  or  $B_z$  field, we find that the TR symmetry  $\sigma_{yz}\mathcal{T}$  is preserved by the termination, thus allowing for mirror-symmetry-protected quasihelical edge modes

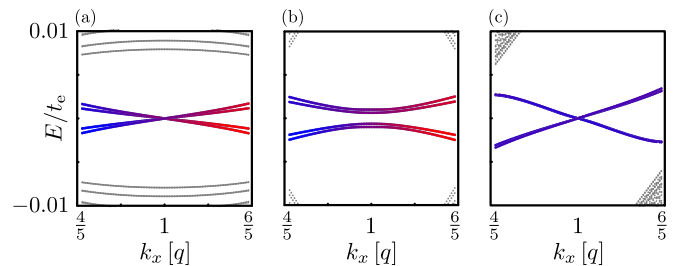


FIG. 20. Impact of an applied Zeeman field on the quasihelical Majorana modes of Fig. 19(d). Once again, only modes on a single edge are also shown here for clarity. (a) Zoom in the edge-mode spectrum of Fig. 19(d). (b) [(c)] Shows the resulting edge spectrum for an external magnetic field in the  $x$  ( $y$ ) direction ( $B_x = 0.04 t_e$ ) [ $(B_y = 0.05 t_e)$ ]. The quasihelical edge modes are protected by the TR symmetry  $\sigma_{yz}\mathcal{T}$ , except in the case for a magnetic field in the  $x$  direction, where the modes get lifted. Hence, the addition of the Zeeman field modifies the symmetry properties at the touching point in such a way so that the quasihelical Majorana modes in (a) still are present in (c). The figures were obtained with open boundary conditions along the  $y$  direction,  $\Delta^e = \Delta^h = 0.1 t_e$ ,  $M_{z,\perp}^{e,h} = 0$ , and  $L_x = L_y = 501$ .

shown in Fig. 20(c) for a field in the  $y$  direction. Finally, we remark that results with a  $B_z$  field are not shown since for the present model the transition to a chiral TSC appears to occur for extremely large values of the magnetic field.

## VI. EXPERIMENTAL IMPLEMENTATION

This section discusses the most prominent categories of systems which exhibit the coveted coexistence of magnetic texture crystals and spin-singlet superconductivity, thus being compatible with the topological scenarios presented in the previous paragraphs. This section (i) associates the various TSCs discussed in the previous paragraphs with realistic physical systems that can support them, (ii) brings to the attention of the reader a number of already accessible 1D and 2D TSC platforms based on a MHC texture, whose properties need to be revisited in the presence of additional magnetic point- and space-group symmetries (see concluding discussions of Sec. II), and (iii) discusses the conditions for realizing TSCs based on the  $\text{SWC}_4$  texture in itinerant magnets.

The existence of such candidate platforms is here made plausible by relying on general symmetry arguments and results from previous theoretical studies, and does not resort to model specific self-consistent studies. It is important to note that for the qualitative discussion pursued in this section, carrying out self-consistent calculations appears nonvital. In this paper we have mainly focused on topological phases for which the magnetic energy scale is required to exceed the pairing gap. See, for instance, Fig. 1 and the topological criterion in Eqs. (45). Hence, our interest lies in situations with a clear separation between the magnetic and pairing energy scales, which simplifies the analysis of their interplay. In the following two subsections we elaborate on two distinct limiting situations, in which one of the two above energy scales clearly dominates over the other.

### A. Case of dominant magnetic energy scale

The limit of interest in this section describes the scenario where the influence of superconductivity is much weaker than that of magnetism. Below, we discuss five general classes of systems that in certain circumstances can satisfy this condition and engineer a TSC.

#### 1. Hybrid devices with integrated nanomagnets

The first possibility is to engineer the desired magnetic texture crystal by means of tunable magnets. Such a direction has recently attracted significant attention from both theoretical [83,85,96–98,101] and experimental [72,221] points of view. The most feasible TSCs that appear to be engineerable in this manner are 1D fully gapped and 2D gapless TSCs generated by a MHC due to the stray fields of a nanomagnet, which is coupled to a single semiconducting nanowire or an array of semiconducting nanowires in proximity to a conventional superconductor. In these systems, one aims at simultaneously tuning the doping of the semiconductor and the periodicity of the magnetic texture crystal, in order to reduce the threshold magnetic energy scale required for the system to enter the topologically nontrivial phase.

#### 2. Magnet-superconductor interfaces

Another platform where 2D TSCs with a fully gapped bulk energy spectrum become accessible are interfaces of a magnetic insulator and a conventional superconductor [87,100,102,152]. The class of so-called chiral magnets, which are characterized by the absence of inversion symmetry and are dictated by the Dzyaloshinskii-Moriya interaction (DM) [222], were theoretically predicted to harbor SSCs more than two decades ago [223,224]. Those theoretical predictions fueled an intense pursuit of such topological magnetic states of matter [225,226], which eventually led to their successful discovery by a number of experimental groups (cf. Refs. [227–231]). Such hybrid platforms have recently drawn renewed attention [107,108], after the discovery of a triple- $Q$  noncoplanar magnetic texture crystal in Mn/Re (0001) [232], and the experimental demonstration of a skyrmion-vortex coupling in such interfaces [108]. Notably, it has been theoretically shown that the triple- $Q$  magnetic order discussed in the experiment of Ref. [232] is capable of inducing a 2D TSC with a nonzero Chern number [100], which supports chiral Majorana edge modes.

To this end, we remark that SSCs arising in chiral magnets due to localized moments typically appear as metastable states which are stabilized by an external magnetic field. In contrast, metallic magnets do not conform to this constraint, and allow for the spontaneous appearance of SSCs [233]. Even more, SSCs can also appear even when inversion symmetry is preserved and the DM interaction is absent. This becomes possible as long as the magnet is sufficiently frustrated. The latter possibility has been shown in Heisenberg models with competing spin-spin couplings of different ranges [234,235].

#### 3. Kondo lattice systems

In the previous section, the magnets in discussion were governed by direct couplings between localized spins which

are described in terms of generalized Heisenberg models. However, another possibility is that the magnetic state arises due to indirect spin-spin interactions, which are mediated by conduction electrons. This indirect mechanism is a result of the Ruderman-Kittel-Kasuya-Yosida (RKKY) interaction [236], and arises due to the exchange coupling between itinerant electrons and localized spin moments. A rich variety of magnetic phases emerge in these systems, which also includes noncoplanar phases such as the SSC texture [237–240]. Since magnetism in this case stems from localized moments, which are described within a classical picture, the modulus of the moments induced by the magnetic texture crystal is also here spatially constant. Consequently, the systems of present interest are prominent candidates for experimentally realizing TSCs in 1D and 2D which result from the MHC [84] and SSC textures [93].

#### 4. Topological magnetic adatom lattices

The next general class consisting of systems known to support the coexistence of magnetic texture crystals and superconductivity concerns a conventional superconductor, on top of which a single chain or a 2D lattice of magnetic adatoms are deposited. See, for instance, the proposals in Refs. [82,86,87,89–92,95,99]. When the exchange coupling of the electrons in the superconducting substrate is sufficiently strong, low-energy in-gap Yu-Shiba-Rusinov states [192] appear and dictate the topological properties of the system. Such systems appear prominent to harbor fully gapped TSCs in 1D and 2D, where the magnetic texture crystal is of the MHC or the SSC type, respectively. Note that, within the limit of classical magnetic adatoms, the magnetic moment of the adatoms is equal and fixed, thus giving rise to a magnetization profile whose modulus is spatially constant.

The type of magnetic order governing these lattices is also here usually controlled by substrate-mediated RKKY spin-spin interactions. The arising magnetic ground state depends on various parameters [80,89,95,241]. Of primary importance here is how the adatom lattice constant compares to the lattice constant or the Fermi wavelength of the substrate since in the present systems these generally differ. Other factors that determine the outcome of the magnetic ground state consist of band-structure features of the substrate superconductor [89], the strength of the Rashba SOC in the substrate and its interplay with crystal fields [80], and finally long-range RKKY-type spin-spin couplings [241].

#### 5. Itinerant magnetic superconductors

In the above four cases, the interplay between magnetism and superconductivity can lead to non-negligible competition type of effects. For example, in nanowire hybrids the superconducting phase exhibited by the metallic segment which is required to engineer the proximity effect “melts” beyond a critical value for the magnetic energy scale. In addition, in topological YSR lattices the pairing term can become substantially suppressed in the vicinity of the adatoms [193], while the RKKY interaction is also rendered shorter ranged when it is mediated by a conventional superconductor [90]. Remarkably, the presence of superconductivity in the substrate on top

of which a magnetic chain is deposited can be pivotal for the stabilization of MHC phases [95].

In spite of these notable consequences of the interplay between these two phases of matter, the competition between magnetism and superconductivity is typically weak in the above-mentioned systems. The reason is that magnetism and superconductivity originate from different degrees of freedom. Therefore, the above four general categories appear prominent for realizing a number of TSCs discussed in this work, and in particular those possessing a fully gapped energy spectrum.

The suppressed competition arising above is, however, not relevant when discussing itinerant magnetic superconductors, in which case both magnetism and superconductivity arise from the same degrees of freedom. A representative category of such systems, which is currently receiving significant attention from the condensed matter physics community, is the quite broad family of FeSCs. While in these systems the competition between magnetism and superconductivity is generally expected to be substantial, FeSCs have been nonetheless experimentally captured to harbor magnetic superconducting phases [109–124]. Even more, the here considered MHC and  $\text{SWC}_4$  have been recently theoretically predicted to appear in doped  $\text{BaFe}_2\text{As}_2$  compounds [134]. In fact, these two magnetic texture crystal phases constitute only a part of the possible magnetic textured phases that can appear as stable global minima in an itinerant tetragonal magnet. Among these, one also finds that the  $\text{SSC}_4$  phase is metastable and only accessible as a local minimum. The above results were obtained in Ref. [134] using a general Landau functional that considers the principal harmonics of magnetic texture crystals.

In the limit of a dominant magnetic energy scale assumed here, magnetic texture crystals which lead to a full gap in the energy spectrum are expected to completely suppress the emergence of superconductivity. At least this picture appears probable to hold in the usual weak-coupling limit, where superconductivity originates from Cooper pairing at the FS. This prohibits the appearance of TSCs in 1D since the FS consists of points and any arising FS is due to accidental degeneracies. However, the 2D case does not present such stringent restrictions since for nonperfectly nested FSs the stabilization of a magnetic texture crystal is expected to gap out only a fraction of the FS, thus leaving behind a reconstructed band structure consisting of Fermi pockets. This remnant FS typically occupies a smaller area than the original FS, and therefore provides a substantially reduced phase space for spin-singlet superconductivity to appear.

Notably, while the shape of the remnant FS may retain inversion symmetry,<sup>14</sup> the FS points connected by inversion do not generally carry opposite spins in the magnetic phase, unless additional symmetries are present. As a matter of fact, this is the case for the MHC and  $\text{SWC}_4$  phases because these do not induce a net spin polarization.<sup>15</sup> This is corroborated by Figs. 21(a) and 21(b), where we depict the spin polarization of

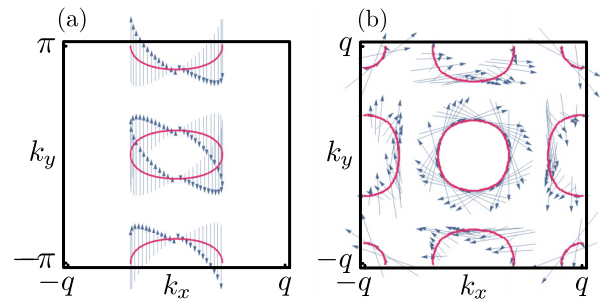


FIG. 21. (a), (b) Show the reconstructed FS for the 2D 1BM of Fig. 7 in the presence of a MHC and a  $\text{SWC}_4$ , respectively. The corresponding FSs in the absence of magnetism are shown in Figs. 7(b) and 11(b). The arrows depict the electronic spin polarization in the  $xy$  spin plane, along the reconstructed FS. In the MHC ( $\text{SWC}_4$ ) phase the net spin polarization is zero, thus inducing a 1D (2D) Rashba type of SOC. Hence, the reconstructed FSs consist of Kramers partners which allow for the spontaneous appearance of spin-singlet superconductivity. The figures were obtained for  $M_{\parallel,\perp} = 2.5t$ .

the remnant FS for the model of Fig. 7, after a reconstruction is introduced by a MHC and a  $\text{SWC}_4$  texture. Indeed, the presence of the two magnetic texture crystals gives rise to a spin texture in  $k$  space which is equivalent to a Rashba type of SOC. Therefore, the emergence of Kramers partners stemming from points connected by inversion allows the spontaneous development of spin-singlet superconductivity. In contrast, the possible appearance of net spin polarization in the remnant FS implies that spin-singlet superconductivity cannot arise for an infinitesimally weak strength of the interaction driving the Cooper pairing, but instead it needs to reach a threshold value since the pairing susceptibility is no longer divergent at zero temperature.<sup>16</sup>

The structure of the spin orientation along the FS is also distinct to the one that typically stabilizes finite Cooper-pair momentum phases [199,200]. The latter phases are usually favored when different FSs are spin polarized in an antiparallel manner. This is obviously not the case here. Therefore, spin-singlet superconductivity pairing up electrons of opposite wave vectors remains favorable. A natural question to ask is what is the  $k$ -space structure of the spin-singlet gap  $\Delta_k$  which becomes preferred deep in the magnetic phase. To provide an answer, one first needs to reclassify the various pairing terms according to the IRs of the magnetic point group. As it has been already discussed in Sec. V, the four 1D IRs of  $D_{4h}$  are bunched together into the two groups  $\{A_{1g}, B_{1g}\}$  and  $\{B_{2g}, A_{2g}\}$  when the MHC sets in, while they all belong to distinct IRs when instead the  $\text{SWC}_4$  emerges [cf. Eqs. (55)–(57)]. Therefore, the emergent  $\Delta_k$  is of the nematic type in the case of MHC, while it is expected to preserve the fourfold symmetry of the energy spectrum in the case of a  $\text{SWC}_4$  texture.

<sup>14</sup>See, for instance, in Table I that the magnetic point groups of MHC and  $\text{SWC}_4$  contain the  $C_2$  point-group element.

<sup>15</sup>This is due to the space-group symmetries discussed in Table I.

<sup>16</sup>In certain systems the emergence of net spin polarization may significantly enhance the tendency to develop equal spin-pairing phases [242]. We assume that this is not the case here.

To this end, an important aspect concerning the possible realization of a TSC needs to be discussed. Since the spin-singlet superconductivity emerges to gap out only the helical FS branch which was left ungapped by the magnetic texture crystal, one expects that the system will prefer to develop a highly selective  $k$  structure, which mainly becomes nonzero in the vicinity of the remnant helical FS. If such a scenario is realized, then a TSC phase does not become accessible since magnetism and superconductivity do not coexist in the same regions of  $k$  space. Nevertheless, such a situation appears highly unlikely for systems whose pairing instabilities are driven by interactions which favor only a low number of crystal harmonics. Consequently, nonzero pairing is expected to also appear in the vicinity of the FS gapped out by the magnetic texture crystals and mediate the electron-hole conversion which is required for the charge-neutral Majorana quasiparticles to appear.

### B. Case of dominant pairing energy scale

Concluding this section, we wish to briefly comment on what types of TSCs are still accessible in the antipodal limit than the one discussed above, i.e., in which the strength of the energy scale of the magnetic texture crystal is subdominant to the pairing gap. It is first of all straightforward to infer that, when magnetism and superconductivity coexist in this limit, TSC phases are not accessible when the system is fully gapped. Instead, if nodes appear in the spectrum, then one arrives at situations similar to the ones discussed in Appendix C 6. There, the nontrivial topology stems from the unconventional character of the pairing term itself, while the influence of the added magnetic texture crystal leads to qualitatively new effects only after its strength exceeds the required threshold to compensate the pairing gap at the nested points of the underlying band structure.

Aside from the above, we remark that an alternative topological scenario becomes accessible when the pairing term contains nodes and the magnetic texture crystal is such so that it mediates the pairwise scattering of all the nodes. In the event that this process leads to a fully gapped energy spectrum, the bulk system may be classifiable as topologically trivial, but it still allows for the appearance of MZMs. This occurs by trapping the MZMs at the cores of vortex defects introduced in the magnetic texture crystal. Such a possibility is detailed in Ref. [44].

## VII. CONCLUSIONS AND OUTLOOK

We provide a systematic classification of the rich variety of accessible topological phases and Majorana excitations that appear due to the bulk interplay of spin-singlet superconductivity and representative magnetic texture crystals. This work aims at inspiring developments in a field which has recently attracted significant interest from both theoretical [44,46,49–54,80–102,134,152] and experimental [67,69,71,72,74,106–108] sides. Our work accounts for all possible strong, weak, and crystalline phases arising in topological superconductors (TSCs) induced by a set of particularly relevant magnetic texture crystals, and considers one- and two-band systems which harbor conventional or unconventional spin-singlet pairing.

As we uncovered here, the concepts of the magnetic and pairing groups play a crucial role in the symmetry classification of these systems since their interplay controls the topological bulk and boundary properties. Our entire discussion unfolds by further assigning and calculating suitable topological invariants that arise from general classification schemes [21–25]. Notably, we show how a number of these abstract invariants emerge in the present context, explicitly provide their construction, and finally clarify their physical meaning by linking their presence to the quantization imposed on a number of physical quantities, such as the staggered magnetization.

Our investigation first focuses on 1D systems. This allows bridging our work with previous known results [83–86,88–90,105] but also reports a long list of different phenomena. Even more, it sets the stage for the formalism that we employ in 2D, which relies on a sublattice description, as well as on downfolding to the magnetic Brillouin zone (MBZ). While a rigorous topological classification is extracted by investigating the symmetry of properties of general Hamiltonians within the sublattice picture, the latter approach exposes transparently the key mechanisms which drive the nontrivial topology. In fact, the MBZ description is also computationally advantageous when studying the topological properties in the low-energy sector since a few number of bands are required for this.

By following the above approaches, we find a number of interesting results in 1D. First of all, we construct crystalline topological invariants which reflect the quantization of the staggered magnetic moment in such systems. In addition, our analysis includes the study of unconventional pairing gaps and discusses how multiple Majorana zero modes appear on a given edge. Another important component of this study is the consideration of two-band models (2BMs). Remarkably, the multiband structure of the magnetization allows interpolating between different symmetry classes, i.e., BDI, AIII, and DIII. The former appears when both interband and intraband magnetic scatterings are present. The second becomes relevant for interband-only scattering, in which case the Majorana edge excitations come in pairs. However, these do not obey a charge-conjugation symmetry and thus each pair should be viewed as a single Andreev zero mode. On the other hand, true Majorana Kramers pairs appear when interband-only scattering is present and additional TR-symmetry-preserving intraband terms are included, e.g., inversion-symmetry-breaking spin-orbit coupling terms. See also Ref. [44].

The emergence of Andreev edge modes in topologically nontrivial systems has recently attracted substantial attention [101,177–180]. Noteworthy, here we obtain topologically protected Andreev modes (cf. Ref. [180]) which are pinned to zero energy in an extended window in parameter space. As a result, these topologically protected zero modes open perspectives for new quantum computing platforms since they can constitute the hardware of long-lived Andreev qubits with enhanced protection against decoherence [181,182]. Even more, engineering systems harboring topologically protected AZMs opens an alternative direction in synthesizing topological Andreev band structures in synthetic space [243–257]. Indeed, such a pursuit in TSCs has so far been unavoidably restricted

to exploiting MZMs in multiterminal devices [250–256], and theoretical works predict that it gives access to the observation of Weyl points, chiral anomaly, and a number of quantized Josephson transport phenomena. Being in a position to obtain AZMs in multiterminal platforms, such as the one experimentally investigated recently in Ref. [258], provides an alternative and in some cases more robust and less demanding route for such types of synthetic topology.

The 2D investigation brings forward an equally rich list of results. By considering once again one- and two-band models, generally unconventional multiband pairing, as well as various multiband implementations of representative textures, we uncover an intricate set of flat-band, unidirectional, bidirectional, quasi-helical, helical, and chiral Majorana edge modes, that may be protected by strong, weak, or crystalline topology. Specifically, for a magnetic helix crystal (MHC) we obtain Majorana and Andreev flat bands, which can be viewed as direct extensions of the 1D phenomena. However, unique physics appears here due to the interplay of the magnetic and pairing point groups, thus revealing a dichotomy when it comes to the topological classification in high-symmetry planes (HSPs). Depending on whether the irreducible representation (IR) of the pairing term belongs to either the  $\{A_{1g}, B_{1g}\}$  or  $\{B_{2g}, A_{2g}\}$  set, we find a different topological classification and, in turn, Majorana edge-mode dispersions.

Considering instead a spin whirl crystal (SWC<sub>4</sub>) magnetic texture which eliminates the possibility of dispersionless edge modes, since the coexistence of two magnetic helix textures winding in different directions and spin planes, lifts almost all the degeneracies in the MBZ. Strikingly, however, mirror and space-group symmetries consistent with the structure of the texture still impose a number of degeneracies in HSPs. These enable the conversion of the flat-band edge modes into unidirectional and bidirectional ones. The bidirectional modes constitute dispersive Majorana edge modes with neither a fixed chirality nor helicity, whose spin character depends on the conserved wave number. Notably, aside from a few exceptions [162], this type of excitation has been poorly discussed so far in the literature.

We find that the emerging topological phases in 2D are mostly of the crystalline or weak type, and become manifest through the appearance of the here-called quasi-helical Majorana edge modes, which present a certain number of similarities with the standard helical edge modes in 2D. Remarkably, strong phases do not become accessible in 2D because the crystalline symmetries present trivialize the respective strong topological invariants. Specifically, the presence of space-group symmetries imposes degeneracies at inversion-symmetric points (ISPs) which, in conjunction with the fourfold rotational symmetry ( $C_4$ ) present, imposes a nodal bulk spectrum in the one-band models (1BMs), and do not allow for a strong  $\mathbb{Z}_2$  invariant in 2BMs despite the fact that a fully gapped spectrum is accessible there. As we demonstrate, one possible route to unlock genuinely 2D topological phases is by including terms which violate  $C_4$  symmetry, while respecting the degeneracies imposed by the magnetic space group. Notably, the violation of  $C_4$  symmetry can be either externally imposed via strain engineering or spontaneously appear in systems with nematic correlations (cf. Ref. [259]).

Another possibility is to consider the additional presence of a Zeeman and exchange field, which lifts the degeneracies at ISPs, but still retains a number of crystalline symmetries. As a result, the arising bidirectional modes can be converted into unidirectional depending on the orientation of the field, Majorana chiral edge modes become accessible in 1BMs, and mirror-symmetry-protected quasi-helical edge modes may persist or get gapped out. Despite the fact that space-group symmetries appear to be detrimental for the appearance of genuinely 2D topological phases, we remark that they still constitute a unique pathway to obtain multiply degenerate Majorana excitations, such as hourglass Majorana edge modes [162]. While such a possibility did not occur for the models examined, it still constitutes an interesting direction of research. Lastly, we remind that space-group symmetries are absent for magnetic textures with incommensurate magnetic ordering vectors [134], but may still be approximately preserved in itinerant magnets for low energies.

At this point, we wish to discuss in more detail prominent candidate physical systems that can host the above-mentioned phenomena. Our framework addresses a single Kramers doublet of the double covering  $D_{4h}$  point group, therefore allowing to describe tetragonal magnets. These systems may, for instance, correspond to correlated magnetic superconductors, where magnetism and superconductivity coexist microscopically. The desirable scenario is the one where a magnetic texture appears to partially gap out a well-nested Fermi surface [134], leaving behind reconstructed pockets, which can be subsequently gapped out by the emergence of superconductivity. Similar to Ref. [89], in this situation one expects that the resulting magnetic superconductor self-tunes into one of the topological phases discussed here.

Among the possible systems that promise to provide a fertile ground to materialize such a possibility, the family of doped Fe-based superconductors (FeSCs) stands out. Some FeSCs are well known to exhibit a coexistence of magnetism and superconductivity [109–124]. Reference [134] has identified all the possible single- and double- $Q$  magnetic ground states that can appear in representative five-orbital models of FeSCs, and demonstrated that doping generally enables various magnetic textures, some of which we explore here. The possible subsequent emergence of conventional or unconventional spin-singlet superconductivity can give rise to a number of the topological scenarios discussed here. Moreover, accounting for a weak band dispersion in the third spatial dimension, which may be non-negligible in certain compounds, opens additional perspectives for realizing systems with topologically protected Weyl and Dirac points [260], as well as nodal lines, rings, and chains [261], thus leading to Majorana and Andreev arc and drumhead surface modes.

Other physical systems which our results may be applicable to include hybrid systems [69,72,74,83,86–98,101] such as superconductor-semiconductor nanowire hybrids and topological magnetic lattices. In the former class of systems, it is desirable to impose on the system the desired magnetic texture by external means, i.e., using nanomagnets [72,221]. In this case, the magnetic wave vectors should be tailored to be comparable to the Fermi wave vectors of the underlying hybrid system, which in turn can be controlled by gating the device. On the other hand, the wave vectors describing the

magnetic texture appearing in topological chains depends on up to which degree is the electronic spectral weight carried by the superconducting electrons of the substrate [78–80]. In the deep so-called Yu-Shiba-Rusinov limit, the magnetic adatoms can be treated classically, and the modulation of the magnetic texture is determined by a number of factors. These include the spacing of the magnetic adatoms, the size of their moment, the strength of their coupling to the substrate electrons, the possible presence of ISB in the substrate and/or crystal-field effects. See Refs. [80,241] for investigations concerning topological magnetic chains.

We continue with enumerating a number of possible experimental methods to infer the various topological phases discussed here, and detect the arising Majorana and Andreev modes. As mentioned already, spin- and angle-resolved photoemission spectroscopy [194] can provide information regarding protected degeneracies. Spectroscopic methods are also standard routes to detect Majorana and Andreev excitations [262–266]. Here we are particularly interested in spin-resolved scanning tunneling spectroscopy [265,266] which can probe the spin character of the boundary excitations [267,268]. The various MF edge modes lead to a characteristic electronic edge spin polarization. For a TSC induced by a MHC the presence of chiral symmetry confines the electronic spin polarization within a given spin plane, similar to what is encountered in superconductor-semiconductor nanowires [265–267], magnetic chains [80,103], as well as charged [254] and neutral [268]  $p$ -wave superfluids. TSCs engineered from the SWC<sub>4</sub> texture exhibit a wider range of possibilities. As we show in Fig. 13, the type of termination is decisive for the spin character of the bidirectional MF modes which possess neither fixed helicity nor chirality. In contrast, unidirectional modes tend to exhibit a higher degree of spin polarization. Chiral and (quasi)helical MFs have instead a fixed spin character since they stem from fully gapped TSCs. Even more, the various dispersionless or dispersive Majorana and Andreev edge modes can be probed in suitably designed generally spin-resolved charge and thermal transport experiments [269–273]. Depending on whether we have electrically neutral (Majorana) or charged (Andreev) edge excitations one can correspondingly look for characteristic features and scaling behaviors in thermal and Hall responses [273].

Finally, we conclude by pointing out that magnetic texture crystals can generally harbor 0D topological defects, such as vortices, which can be further employed to trap Majorana zero modes. This was brought to light only recently in Ref. [44], where it was also shown that such a mechanism takes place only when the pairing term of the coexisting superconducting order contains nodes in its bulk energy spectrum. By considering also this possibility, spin-singlet superconductors harboring magnetic textures appear to be unique versatile platforms where a multitude of TSC phases can be observed and harnessed for cutting-edge applications.

#### ACKNOWLEDGMENTS

D.S. and B.M.A. acknowledge support from the Carlsberg Foundation. B.M.A. additionally acknowledges support from the Independent Research Fund Denmark Grant No. DFF-6108-00096. M.H.C. acknowledges financial support from

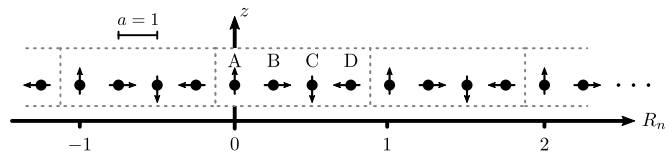


FIG. 22. Unit cells for a 1D system experiencing a magnetic texture with a four-site periodicity. The four sites of a unit cell are labeled as {A, B, C, D} and the center of inversion is here chosen to be the site A of the  $n = 0$  unit cell.

U.S. Department of Energy, Office of Science, Basic Energy Sciences, Materials Science and Engineering Division, under Award No. DE-SC0020045.

#### APPENDIX A: SUBLATTICE FORMULATION IN 1D

In this Appendix, we reformulate our analysis in terms of a four-sublattice basis, which is more transparent in regards to the topological classification since it leads to properly compactified  $2\pi$ -periodic Hamiltonians. For illustrative purposes, we restrict to the 1D case since the 2D description is obtainable in a straightforward manner. Within this framework a unit cell consists of four sites labeled as {A, B, C, D} (cf. Fig. 22). We define the spinor

$$\vec{\psi}_n^\dagger = (\psi_{A,n}^\dagger, \psi_{B,n}^\dagger, \psi_{C,n}^\dagger, \psi_{D,n}^\dagger), \quad (\text{A1})$$

where  $n$  now labels a four-site unit cell. In this basis, a translation  $\{\mathbb{1} | a\}$  effects the shift  $n \mapsto n + \frac{1}{4}$ . Hence,  $\{\mathbb{1} | a\}$  and  $\{\mathbb{1} | 2a\} \equiv \{\mathbb{1} | \pi/Q\}$  [for  $Q = \pi/(2a)$ ] read as, in wave-number space  $k_x \in (-\pi/4, \pi/4)$  (with  $a = 1$ ),

$$\begin{aligned} \{\mathbb{1} | a\} &= \begin{pmatrix} 0 & 0 & 0 & \beta^* \\ 1 & 0 & 0 & 0 \\ 0 & 1 & 0 & 0 \\ 0 & 0 & 1 & 0 \end{pmatrix}, \\ \{\mathbb{1} | \pi/Q\} &= \begin{pmatrix} 0 & 0 & \beta^* & 0 \\ 0 & 0 & 0 & \beta^* \\ 1 & 0 & 0 & 0 \\ 0 & 1 & 0 & 0 \end{pmatrix}, \end{aligned} \quad (\text{A2})$$

where we set  $\beta = -e^{i4k_x}$  in order for the MBZs of the wave-number shifts and sublattice descriptions to match. Next, we identify the action of inversion  $\mathcal{I}$  about the center of inversion which is here set to be the A site of the  $n = 0$  unit cell. For a Hamiltonian element  $\hat{H}_{k_x}$  defined in the respective wave-number spinor of Eq. (A1), inversion acts as  $\mathcal{I}\hat{H}_{k_x} = [\hat{\mathcal{I}}^\dagger \hat{H}_{k_x} \hat{\mathcal{I}}]_{k_x \mapsto -k_x}$  with

$$\hat{\mathcal{I}} = \begin{pmatrix} 1 & 0 & 0 & 0 \\ 0 & 0 & 0 & \beta \\ 0 & 0 & \beta & 0 \\ 0 & \beta & 0 & 0 \end{pmatrix}. \quad (\text{A3})$$

We note that the inversion of  $k_x$  takes place only after the matrix multiplications. This is because the matrix representation of inversion is  $k_x$  dependent in this basis. The kinetic energy operator describing first- ( $t$ ), second- ( $t'$ ), and

third- ( $t''$ ) order neighbor hopping is represented as

$$\hat{H}_{\text{kin},k_x} = -t \begin{pmatrix} 0 & 1 & 0 & \beta^* \\ 1 & 0 & 1 & 0 \\ 0 & 1 & 0 & 1 \\ \beta & 0 & 1 & 0 \end{pmatrix} - t'' \begin{pmatrix} 0 & \beta^* & 0 & 1 \\ \beta & 0 & \beta^* & 0 \\ 0 & \beta & 0 & \beta^* \\ 1 & 0 & \beta & 0 \end{pmatrix} - t' \begin{pmatrix} 0 & 0 & 1 + \beta^* & 0 \\ 0 & 0 & 0 & 1 + \beta^* \\ 1 + \beta & 0 & 0 & 0 \\ 0 & 1 + \beta & 0 & 0 \end{pmatrix}. \quad (\text{A4})$$

One verifies that the above kinetic part of the Hamiltonian is invariant under translations and inversion. The Hamiltonian for the MHC texture in Eq. (2) here reads as

$$\hat{H}_{\text{mag}} = \begin{pmatrix} M_{\perp}\sigma_z & 0 & 0 & 0 \\ 0 & M_{\parallel}\sigma_x & 0 & 0 \\ 0 & 0 & -M_{\perp}\sigma_z & 0 \\ 0 & 0 & 0 & -M_{\parallel}\sigma_x \end{pmatrix}. \quad (\text{A5})$$

The main target of this Appendix is to shed light to the topological classification at ISPs and HSPs. At  $k_x = 0$ , we find that  $\mathcal{I}$  and  $\{\mathbb{1} | \pi/Q\}$  possess the twofold-degenerate eigenvalues  $\pm 1$  and  $\pm i$ , respectively. Instead, at  $k_x = \pi/4$ , we find that  $\mathcal{I}$  possesses the eigenvalues  $\{1, 1, 1, -1\}$ , while  $\{\mathbb{1} | \pi/Q\}$  possesses the twofold-degenerate eigenvalues  $\pm 1$ . The emergence of different eigenvalues for these symmetry operations at the two ISPs implies that the respective symmetry classes generally differ. In contrast, these symmetry operators are  $k_x$  independent in the wave-number-transfer description, thus implying that the various ISPs and HSPs are dictated by the same symmetry and topological properties. The apparent discrepancy is attributed to the fact that the Hamiltonian in the wave-number-transfer description is not compactified. Therefore, caution is needed when performing the classification using this formalism. In fact, we find that the topological classifications coincide for the the ISPs and HSPs where a magnetic gap opens. In contrast, at ISPs and HSPs where a Kramers degeneracy appears and the magnetization becomes ineffective, only the sublattice-based topological classification is valid.

## APPENDIX B: SPACE-GROUP SYMMETRY-PROTECTED DEGENERACIES

Nonsymmorphic space-group operations take the form  $\{g | \mathbf{t}\}$ , where  $g$  defines a point-group operation and  $\mathbf{t}$  is a translation by a fraction of a Bravais lattice vector. A space-group symmetry is referred to as nonsymmorphic, when no coordinate system can be chosen to remove the translation  $\mathbf{t}$  in  $\{g | \mathbf{t}\}$  [162, 196, 197, 274, 275]. This is satisfied when  $g\mathbf{t} = \mathbf{t}$ , i.e., when the involved translation is along a HSP of  $g$ . If this is not the case, the component of  $\mathbf{t}$  which is perpendicular to the HSP of  $g$  is obsolete and can be removed. However, such a removal may result in the redefinition of other symmorphic-symmetry elements, which in this basis may involve a translation. The elements that become simultaneously modified in such a process define the so-called set of “off-centered symmetry elements.” In the main text, we encounter pairs of such off-centered symmetries. As explained

below, their presence introduces protected degeneracies in the spectrum. See also Refs. [276–279], and Figs. 23 and 24.

The fact that a genuine nonsymmorphic symmetry requires that the equivalence  $g\mathbf{t} = \mathbf{t}$  should be met further restricts the systems in which nonsymmorphic symmetries can provide topological protection to boundary modes and thus stabilize crystalline topological phases. Since such a boundary is required to preserve both  $g$  and  $\mathbf{t}$ , only 3D systems can exhibit topological crystalline phases induced by nonsymmorphic symmetries. Indeed, edges of 2D systems generally fail to fulfill these criteria, and the presence of nonsymmorphic symmetries can only affect the bulk topological properties of the system. Consider, for example, a 2D system with the nonsymmorphic symmetry  $\{\sigma_{xz} | (1, 0)\}$ . For this particular case, the edge (01) is invariant under  $\sigma_{xz}$  while (10) is preserving  $\{\mathbb{1} | (1, 0)\}$ , i.e., we can never find an edge which is invariant under the symmetry operation  $\{\sigma_{xz} | (1, 0)\}$ . Extending the example to 3D systems, we immediately observe that the surface (001) preserves both  $\sigma_{xz}$  and  $\{\mathbb{1} | (1, 0)\}$ , and can thus potentially exhibit topological surface states protected by the nonsymmorphic symmetry. Hence, we conclude that a nonsymmorphic symmetry cannot induce a crystalline topological phase in 2D systems, except in rare cases where  $g\mathbf{k} = \mathbf{k}$  [162].

For the MHC texture in 1D, our system is invariant under a set of symmetries shown in Table I. Out of these, we find that the symmetry element  $\{\sigma_{yz} | \pi/Q\}$  is rendered symmorphic after translating the magnetic unit cell by  $\{\mathbb{1} | a\}$ , as shown in Fig. 24. At the same time, the point-group element  $\mathcal{R}_{yz} = \sigma_{yz}\mathcal{T}\Theta$  is redefined and in this basis involves a translation. Specifically, the two symmetry elements become redefined as follows:

$$\left\{ \sigma_{yz} \left| \frac{\pi}{Q} \right. \right\} \mapsto \sigma_{yz} \quad \text{and} \quad \mathcal{R}_{yz} \mapsto \left\{ \mathcal{R}_{yz} \left| \frac{\pi}{Q} \right. \right\}. \quad (\text{B1})$$

In fact, it is not possible to choose a coordinate system for which both  $\{\sigma_{yz} | \frac{\pi}{Q}\}$  and  $\mathcal{R}_{yz}$  become regular point-group elements. This leads to symmetry-protected degeneracies in the spectrum. To exemplify this, we rely on the relation  $\{\sigma_{yz} | \frac{\pi}{Q}\} \mathcal{R}_{yz} = \mathcal{R}_{yz} \{\sigma_{yz} | \frac{\pi}{Q}\} e^{ik_{\mathcal{I}}\pi/Q}$ . By further taking into account that  $\Theta^2 = +\mathbb{1}$ , which holds in the here-relevant BDI symmetry class, we obtain  $\{\sigma_{yz} | \frac{\pi}{Q}\}^2 = +\mathbb{1} e^{ik_{\mathcal{I}}\pi/Q}$  for  $k_{\mathcal{I}} = 0, q$ . This leads to the two eigenvalue equations

$$\left\{ \sigma_{yz} \left| \frac{\pi}{Q} \right. \right\} |k_{\mathcal{I}}, \pm\rangle = \pm e^{ik_{\mathcal{I}}\pi/Q} |k_{\mathcal{I}}, \pm\rangle, \quad (\text{B2})$$

$$\left\{ \sigma_{yz} \left| \frac{\pi}{Q} \right. \right\} \mathcal{R}_{yz} |k_{\mathcal{I}}, \pm\rangle = \pm e^{3ik_{\mathcal{I}}\pi/Q} \mathcal{R}_{yz} |k_{\mathcal{I}}, \pm\rangle. \quad (\text{B3})$$

We thus observe that the two pairs  $|k_{\mathcal{I}}, \pm\rangle$  and  $\mathcal{R}_{yz}|k_{\mathcal{I}}, \pm\rangle$  have the same (opposite) eigenvalues at  $k_{\mathcal{I}} = 0$  ( $k_{\mathcal{I}} = q$ ). The two states are therefore mutually “parallel” (orthogonal) at  $k_{\mathcal{I}} = 0$  ( $k_{\mathcal{I}} = q$ ), ultimately leading to a protected degeneracy at  $k_x = q$  [see Fig. 23(a)].

The above degeneracies appear at isolated points of the MBZ. This behavior has to be compared with the consequences of the genuinely nonsymmorphic symmetry  $\{\sigma_{xz} | \frac{\pi}{Q}\} k_x = k_x$ . The latter can be employed to label the eigenstates of the Hamiltonian  $\forall k_x$  in the 1D MBZ. Since the

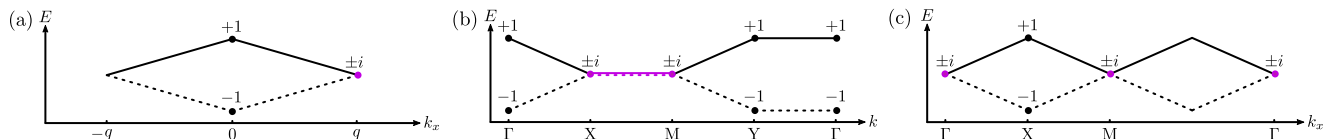


FIG. 23. Sketches of the entire bulk band structure, or cuts of it, in the case of a MHC in 1D and 2D [(a) and (b)], and the SWC<sub>4</sub> magnetic phase [(c)]. The labels show the eigenvalues of the space-group symmetry which commutes with the Hamiltonian in the given HSP. Degeneracies are colored in purple.

system is effectively spinless,  $\Theta^2 = +\mathbb{1}$ , we find

$$\left\{ \sigma_{xz} \left| \frac{\pi}{Q} \right. \right\} |k_x, \pm\rangle = \pm e^{ik_x \pi/Q} |k_x, \pm\rangle. \quad (\text{B4})$$

From the above eigenvalues, in combination with  $\Theta$ , we know that the spectrum in the MBZ must follow the sketch in Fig. 23(a), which is compatible with the degeneracies imposed by the pair of off-centered symmetries. The twofold degeneracy at  $k_x = q$  is enforced because the eigenvalues  $\pm i$  are connected by the antiunitary symmetry  $\Theta$ . Notably, this degeneracy can be alternatively seen as the result of the emergent TR symmetry effected by  $\tilde{\Theta} = \{\sigma_{xz} | \frac{\pi}{Q}\} \Theta \equiv \{\mathcal{T} | \pi/Q\}$ , with  $\tilde{\Theta}^2 = \mathbb{1} e^{ik_x \pi/q}$ .

Similar arguments for the MHC in 2D establish once again that the symmetries  $\{\sigma_{yz} | \frac{\pi}{Q}\}$  and  $\mathcal{R}_{yz}$  constitute a pair of off-centered ones, and impose a twofold degeneracy at  $k_x = q$  for all  $k_y \in [0, 2\pi)$ . This gives insight about the key features of the generic band structure which is depicted in Fig. 23(b), and reveals that the pairing gap cannot be compensated by the magnetic gap in this HSP.

We conclude this section with a brief comment on the generic characteristics of the band structure for a 2D system under the influence of a SWC<sub>4</sub> texture. In this case, we do not find any off-centered symmetries. Nonetheless, twofold degeneracies still appear as the result of the presence of non-symmorphic symmetries. See Fig. 23(c) for a sketch of the general dispersion in the MBZ.

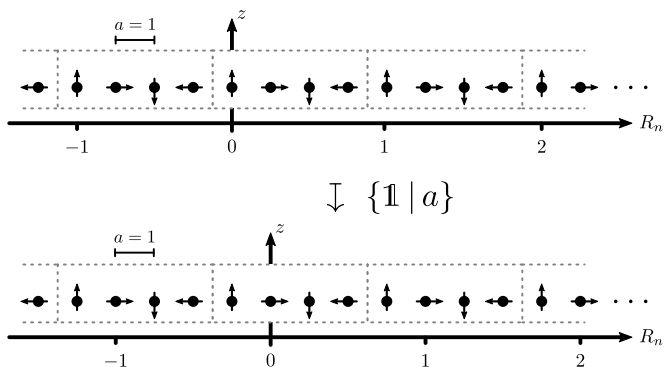


FIG. 24. Sketch of the magnetic unit cell under the action of  $\{\mathbb{1} | a\}$ . This translation renders  $\{\sigma_{yz} | \frac{\pi}{Q}\}$  symmorphic, while at the same modifying  $\mathcal{R}_{yz}$ . See Eq. (B1).  $\{\sigma_{yz} | \frac{\pi}{Q}\}$  and  $\mathcal{R}_{yz}$  define a pair of off-centered symmetries.

## APPENDIX C: DETAILS ON TOPOLOGICAL INVARIANTS

### 1. Winding number in 1D IBMs for $\Delta_{k_x} = \Delta$

The calculation is facilitated by noticing the presence of the antiunitary TR symmetry  $\tilde{\Theta} = \rho_2 \sigma_y \mathcal{K}$  of the Hamiltonian in Eq. (24). Being  $k_x$  independent,  $\tilde{\Theta}$  influences the topological classification in the entire MBZ. Note that such a  $k_x$ -independent symmetry does not appear in the sublattice formulation of the problem. The product involving  $\tilde{\Theta}$  and the preexisting  $\Theta = \mathcal{K}$  symmetry induces the unitary symmetry  $\tilde{\mathcal{O}} = \tilde{\Theta} \Theta = \rho_2 \sigma_y$ . In particular, this allows us to diagonalize the BdG Hamiltonian into blocks labeled by the eigenvalues of  $\tilde{\mathcal{O}}$ . By performing the unitary transformation induced by the operator  $\tilde{\mathcal{S}} = (\tilde{\mathcal{O}} + \sigma_z)/\sqrt{2}$ , we obtain the blocks

$$\begin{aligned} \hat{\mathcal{H}}'_{k_x, \sigma} = & [h_{k_x}^{(0)} + h_{k_x}^{(1)} \rho_2 + h_{k_x}^{(2)} \eta_3 + h_{k_x}^{(3)} \eta_3 \rho_2] \tau_3 - M_\sigma \rho_1 \\ & + M_{-\sigma} \eta_1 \rho_1 + [\Delta_{k_x}^{(0)} + \Delta_{k_x}^{(1)} \rho_2 + \Delta_{k_x}^{(2)} \eta_3 \\ & + \Delta_{k_x}^{(3)} \eta_3 \rho_2] \tau_1, \end{aligned} \quad (\text{C1})$$

where  $M_\sigma = (M_\parallel + \sigma M_\perp)/2$ , with  $\sigma = \pm 1$  labeling the eigenvalues of  $\sigma_z$  in the new frame. Both blocks reside in BDI class with  $\Theta = \mathcal{K}$ ,  $\Xi = \rho_2 \tau_2 \mathcal{K}$ , and  $\Pi = \rho_2 \tau_2$ . Consequently, the presence of the unitary symmetry effected the symmetry-class transition  $\text{BDI} \rightarrow \text{BDI} \oplus \text{BDI}$ , which allows defining a winding number  $w_\sigma$  for each block.

One observes that each block leads to a fractional winding number  $\pm \frac{1}{2}$ . As discussed previously in Ref. [80], this peculiarity is due to the choice of the spinor, which, while being convenient, does not guarantee that the Hamiltonian blocks satisfy the compactification criteria required to define the  $\mathbb{Z}$  index. As a result, the block winding numbers cannot define two independent topological invariants, but they have to be added or subtracted to provide the proper invariant. The correct way to combine them can be inferred based on a well-known limiting case or by adding infinitesimal terms which violate the unitary symmetry but preserve  $\Theta$ ,  $\Xi$ , and  $\Pi$ . Nevertheless, here it is straightforward to infer how to combine the block invariants by investigating their behavior in the already established result for  $M_\perp = M_\parallel = M > 0$ . In this known case, the block winding numbers become

$$\begin{aligned} w_{+}^{M_\parallel, \perp = M} &= -\frac{\text{sgn}\{(M^2 - \Delta^2)[1 + (\Delta^2 - M^2)/(2\mu)^2]\}}{2}, \\ w_{-}^{M_\parallel, \perp = M} &= \frac{1}{2}. \end{aligned} \quad (\text{C2})$$

In order to retrieve the topological invariant of Eq. (14), we verify that the winding number should be defined as

$$w = w_- - w_+. \quad (\text{C3})$$



## 2. Winding number in 1D 1BMs for a generic $\Delta_{k_x}$

Here we obtain an expression for the winding number in the case of a generic  $\Delta_{k_x}$ . To facilitate the derivation of an analytical result, we restrict to the weak-coupling limit. We block diagonalize the low-energy BdG Hamiltonian in Eq. (33) and find

$$\hat{\mathcal{H}}_{k_x, \sigma}^{\text{low-en}} = (\xi_{k_x; q}^+ + \xi_{k_x; q}^- \rho_2) \tau_3 - M_\sigma \rho_1 + (\Delta_{k_x; q}^+ + \Delta_{k_x; q}^- \rho_2) \tau_1, \quad (\text{C4})$$

and define

$$\det(\hat{A}_{k_x, \sigma}^{\text{low-en}}) = (\xi_{k_x; q}^+)^2 + (\Delta_{k_x; q}^+)^2 - (\xi_{k_x; q}^-)^2 - (\Delta_{k_x; q}^-)^2 - M_\sigma^2 + 2i(\xi_{k_x; q}^- \Delta_{k_x; q}^+ - \xi_{k_x; q}^+ \Delta_{k_x; q}^-), \quad (\text{C5})$$

which is of the exact same form as Eq. (8), with the crucial difference that here  $k_x \in \text{MBZ}$ , which implies that the contribution of the last term in the topological invariant of Eq. (29) drops out. In addition, when  $k_x = 0$  constitutes the only wave number where a gap closing takes place, one directly retrieves the result of Eq. (30) after setting  $\Delta_{k_x} = \Delta$ .

## 3. Mirror invariant in 1D 1BMs

To evaluate the mirror invariant of Eq. (34) at  $k_x = 0$ , we restrict to the weak-coupling regime, and block diagonalize Eq. (33) by means of effecting the unitary transformation  $(\mathcal{O}_{yz} + \sigma_x)/\sqrt{2}$ , which yield the blocks

$$\hat{\mathcal{H}}_{k_x=0, \sigma}^{\text{low-en}} = \xi_{0; q}^+ \tau_3 + \Delta_{0; q}^+ \tau_1 - \sigma \frac{M_\perp + M_\parallel \rho_3}{2}. \quad (\text{C6})$$

The above is further block diagonalizable by introducing the eigenstates of  $\rho_3$  labeled by  $\rho = \pm 1$ . Straightforward manipulations following after the definitions of Eq. (18) yield the result for each  $\hat{\mathcal{H}}_{k_x=0, \sigma, \rho}^{\text{low-en}}$  block:

$$n_{k_x=0, \sigma, \rho} = \sigma \rho \frac{1 + \text{sgn}[M_\rho^2 - (\xi_{0; q}^+)^2 - (\Delta_{0; q}^+)^2]}{2}.$$

Similar to the construction leading to Eq. (C3), also here one has to consider combinations of the invariants stemming from the  $\rho$  blocks. Specifically, here we need to define  $n_{k_x=0, \sigma} = -(n_{k_x=0, \sigma, -} + n_{k_x=0, \sigma, +})/2$ .

## 4. Glide Majorana parity

The glide Majorana parity is here defined as a  $\mathbb{Z}_2$  invariant for the BDI class in 0D. This is given as the parity of the winding number for an interpolation  $\hat{\mathcal{H}}_\ell$  with  $\ell \in [0, 2\pi)$  connecting the Hamiltonian of interest  $\hat{\mathcal{H}}_\pi$  and a reference Hamiltonian  $\hat{\mathcal{H}}_0$ . The winding number reads as

$$w_{\text{inter}} = \int_0^{2\pi} \frac{d\ell}{2\pi i} \text{Tr} \left( \hat{A}_\ell^{-1} \frac{d}{d\ell} \hat{A}_\ell \right). \quad (\text{C7})$$

By virtue of the charge-conjugation symmetry, we obtain

$$\begin{aligned} i\pi w_{\text{inter}} &= \ln[\det(\hat{A}_\pi)/\det(\hat{A}_0)] \\ \Rightarrow P_G &= \text{sgn}[(-1)^{w_{\text{inter}}}] = \text{sgn} \prod_{\ell=0, \pi} \det(\hat{A}_\ell). \end{aligned} \quad (\text{C8})$$

To obtain the result of Eq. (37), we employ the above equation, where each one of the two  $\sigma$  blocks of Eq. (35) is considered as a reference Hamiltonian for the other. In the weak-coupling limit, we project onto the  $\eta_3 = 1$  block and obtain the Hamiltonian blocks:

$$\hat{\mathcal{H}}_{k_x=0, \sigma}^{\text{low-en}} = \xi_{0; q}^+ \tau_3 + \Delta_{0; q}^+ \tau_1 - M_\sigma \rho_1. \quad (\text{C9})$$

We block off-diagonalize the above blocks via the transformation  $(\rho_2 \tau_2 + \tau_3)/\sqrt{2}$  and find

$$\hat{A}_{k_x=0, \sigma} = -\Delta_{0; q}^+ - M_\sigma \rho_3 - i\xi_{0; q}^+ \rho_2. \quad (\text{C10})$$

By obtaining the determinant of the above upper off-diagonal blocks, we directly find the result of Eq. (37).

## 5. Winding number in 1D 2BMs

To obtain the winding number for an interband-only MHC, we restrict to the low-energy sector of the system and consider the projected spinor

$$\chi_{k_x}^{2\text{BM}} = \frac{\rho_2 + \rho_3}{\sqrt{2}} (\Psi_{k_x+3q}^e, \Psi_{k_x-3q}^e, \Psi_{k_x+3q}^h, \Psi_{k_x-3q}^h)^\top, \quad (\text{C11})$$

as well as the corresponding Hamiltonian blocks

$$\begin{aligned} \hat{\mathcal{H}}_{k_x}^{\text{low-en}} &= \sum_{s=e, h} \mathcal{P}_s \{ (\xi_{k_x; -3q}^{s,+} + \xi_{k_x; -3q}^{s,-} \rho_2) \tau_3 + \Delta^s \tau_1 \} \\ &\quad - \frac{\hat{M}_\perp \rho_1 \sigma_z + \hat{M}_\parallel \rho_3 \sigma_x}{2}. \end{aligned} \quad (\text{C12})$$

By exploiting the  $\tilde{\mathcal{O}} = \rho_2 \sigma_y$  symmetry, we can block diagonalize the Hamiltonian by means of  $\tilde{\mathcal{S}}$  in Appendix C 1:

$$\begin{aligned} \hat{\mathcal{H}}_{k_x, \rho}^{\text{low-en}} &= \sum_{s=e, h} \mathcal{P}_s \{ (\xi_{k_x; -3q}^{s,+} + \xi_{k_x; -3q}^{s,-} \rho_2) \tau_3 + \Delta^s \tau_1 \} \\ &\quad - \hat{M}_\sigma \rho_1. \end{aligned} \quad (\text{C13})$$

By solely considering interband magnetic scattering, i.e.,  $\hat{M}_\sigma = M_\sigma \kappa_1$  we find the emergent unitary symmetry  $\mathcal{O} = \kappa_3 \sigma_y$  in the original basis, which allows for yet another block diagonalization via  $(\tilde{\mathcal{S}}^\dagger \mathcal{O} \tilde{\mathcal{S}} + \rho_1)/\sqrt{2}$ :

$$\begin{aligned} \hat{\mathcal{H}}_{k_x, \rho}^{\text{low-en}} &= \sum_{s=e, h} \mathcal{P}_s \{ (\xi_{k_x; -3q}^{s,+} + \rho \xi_{k_x; -3q}^{s,-} \kappa_3) \tau_3 + \Delta^s \tau_1 \} \\ &\quad - \rho M_\sigma \kappa_1, \end{aligned} \quad (\text{C14})$$

where  $\rho = \pm 1$  label the eigenvalues of the matrix  $\rho_1$ . Hence, we block off-diagonalize the Hamiltonian via the unitary transformation  $(\Pi + \tau_3)/\sqrt{2}$ , and obtain

$$\begin{aligned} \det(\hat{A}_{k_x, \sigma, \rho}^{\text{low-en}}) &= \xi_{k_x+3q}^e \xi_{k_x-3q}^h + \Delta^e \Delta^h - M_\sigma^2 \\ &\quad + i(\xi_{k_x+3q}^e \Delta^h - \xi_{k_x-3q}^h \Delta^e). \end{aligned} \quad (\text{C15})$$

A nonzero intraband magnetization components restores the BDI  $\oplus$  BDI class found in 1BMs and yields

$$\hat{A}_{k_x, \sigma}^{\text{low-en}} = - \sum_{s=e,h} \mathcal{P}_s \{ i(\xi_{k_x; -3q}^{s,+} + \xi_{k_x; -3q}^{s,-}) + \Delta^s + M_\sigma^s \rho_3 \} - \kappa_1 M_\sigma^{\text{eh}} \rho_3. \quad (\text{C16})$$

## 6. Invariants for 2D 1BMs in the MHC phase and with

$$\Delta_{\mathbf{k}} \sim \{B_{2g}, A_{2g}\}$$

For a gap function transforming as the  $B_{2g}$  or  $A_{2g}$  IR, the resulting point group becomes  $G_{\text{MHC}}$  accompanied by the space-group symmetries  $\{\mathcal{T}, \sigma_{xz, yz}^{\mathcal{Q}} | (\frac{\pi}{Q}, 0)\}$ . As discussed in Sec. V A 1, these modified symmetries lead to a BDI  $\oplus$  BDI class in the  $k_x = 0$  HSP and a AI  $\oplus$  AI class for  $k_y = \{0, \pi\}$  since, for the latter, the gap function vanishes. Specifically, for these HSPs, denoted by the wave vectors  $\mathbf{k}_{\mathcal{R}_{xz}}$ , the Hamiltonian takes the simple form in the weak-coupling regime:

$$\hat{H}_{\mathbf{k}_{\mathcal{R}_{xz}}, \sigma, \tau} = \tau [\xi_{\mathbf{k}_{\mathcal{R}_{xz}}; q_1}^+ + \xi_{\mathbf{k}_{\mathcal{R}_{xz}}; q_1}^- \rho_2] - M_\sigma \rho_1, \quad (\text{C17})$$

where  $\tau = \pm 1$  labels the two AI blocks. This class only supports a strong mirror  $\mathbb{Z}$  invariant for a nodal spectrum, with the associated invariant defined similar to Eq. (48). Specifically, we find the normalized complex function entering in the invariant

$$Z_{\epsilon, k_x, \sigma, \tau} = \frac{\xi_{\mathbf{k}_{\mathcal{R}_{xz}}; -q_1} \xi_{\mathbf{k}_{\mathcal{R}_{xz}}; +q_1} + \epsilon^2 + M_\sigma^2 + 2i\tau \epsilon \xi_{\mathbf{k}_{\mathcal{R}_{xz}}; q_1}^+}{\sqrt{(\xi_{\mathbf{k}_{\mathcal{R}_{xz}}; -q_1} \xi_{\mathbf{k}_{\mathcal{R}_{xz}}; +q_1} + \epsilon^2 + M_\sigma^2)^2 + 4\epsilon^2 (\xi_{\mathbf{k}_{\mathcal{R}_{xz}}; q_1}^+)^2}}. \quad (\text{C18})$$

Instead, for the  $k_x = 0$  HSP, the BdG Hamiltonian in the weak-coupling limit becomes

$$\hat{H}_{\mathbf{k}=(0, k_y)} = \xi_{\mathbf{k}=(q, k_y)} \tau_3 - \Delta_{\mathbf{k}=(q, k_y)} \rho_2 \tau_1 - (M_\perp \rho_1 \sigma_z + M_\parallel \rho_3 \sigma_x) / 2. \quad (\text{C19})$$

For this case we can only define a strong invariant for a fully gapped spectrum, namely, the glide  $w_{G, k_x=0}$  and mirror  $w_{M, k_x=0}$  winding numbers [see Eqs. (49) and (21)] after replacing  $\epsilon \mapsto k_y$  in the latter. For the symmetry  $\{\mathcal{T} | (\frac{\pi}{Q}, 0)\} \Theta \equiv \tilde{\mathcal{O}}$  we block diagonalize the Hamiltonian via  $\tilde{S}$  and find

$$\hat{H}_{\mathbf{k}=(0, k_y), \sigma} = \xi_{\mathbf{k}=(q, k_y)} \tau_3 - \Delta_{\mathbf{k}=(q, k_y)} \rho_2 \tau_1 - M_\sigma \rho_1. \quad (\text{C20})$$

After block off-diagonalizing the above Hamiltonian by means of the unitary operator  $(\rho_2 \tau_2 + \tau_3) / \sqrt{2}$ , we obtain

$$\det(\hat{A}_{k_y, \sigma}) = \xi_{\mathbf{k}=(q, k_y)}^2 - \Delta_{\mathbf{k}=(q, k_y)}^2 - M_\sigma^2 + 2i \xi_{\mathbf{k}=(q, k_y)} \Delta_{\mathbf{k}=(q, k_y)}.$$

For the remaining two symmetries  $\{\sigma_{yz}^{\mathcal{Q}} | (\frac{\pi}{Q}, 0)\}$  and  $\mathcal{R}_{xz}^{\mathcal{Q}}$ , which in fact commute with  $\tilde{\mathcal{O}}$ , we find that their matrix representations coincide in each  $\sigma$  block. This leads to the additional block diagonalization by means of the unitary operator  $(\rho_1 \tau_3 + \rho_2) / \sqrt{2}$ :

$$\hat{H}_{\mathbf{k}=(0, k_y), \sigma, \rho} = \xi_{\mathbf{k}=(q, k_y)} \tau_3 - \rho \Delta_{\mathbf{k}=(q, k_y)} \tau_1 - \rho M_\sigma \tau_3, \quad (\text{C21})$$

which we further block off-diagonalize with by means of a unitary transformation with operator  $(\tau_2 + \tau_3) / \sqrt{2}$ , and find  $\hat{A}_{\mathbf{k}=(0, k_y), \sigma, \rho} = -i[\xi_{\mathbf{k}=(q, k_y)} - \rho M_\sigma] + \rho \Delta_{\mathbf{k}=(q, k_y)}$ .

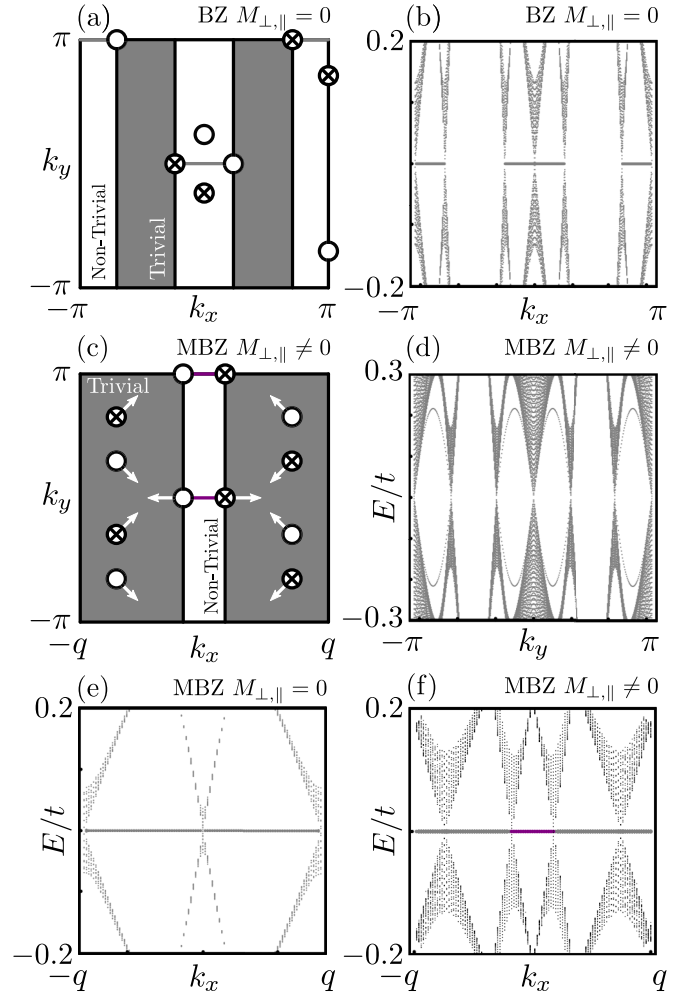


FIG. 25. Nodal spectrum for the 1BM in Fig. 7 in the MHC phase with  $\Delta_{\mathbf{k}} = \Delta \sin k_x \sin k_y \sim B_{2g}$ . (a) Displays the nodes in the first BZ in the absence of magnetism. These symmetry-enforced nodes give rise to MFBS, as seen in (b). (c) Illustrates the same as in (a), after we include magnetism and downfold to the MBZ. We see that the initial nodes in (a) split and move on straight lines. This ultimately lifts the MFBS on edges perpendicular to the magnetic ordering wave vector  $\mathcal{Q}$  [see (d)] since the vorticity of the nodes cancels when projected onto this edge. In contrast, we see in (f) that new MFBS (marked in purple) are established on edges parallel to  $\mathcal{Q}$  in addition to the MFBS inherited from the case of  $M_\parallel = M_\perp = 0$  (marked in gray) [cf. (e)]. We used  $L_x = L_y = 401$ ,  $\Delta = 1t$  throughout, and  $M_{\perp, \parallel} = 0.8t$  in (d) and (f).

In order to exemplify the above, we consider in the following the 1BM from Fig. 7 in the MHC phase, with a pairing function transforming as the  $B_{2g}$  IR, specifically,  $\Delta_{\mathbf{k}} = \Delta \sin k_x \sin k_y$ . Through relation Eq. (47), we find the gap-closing points  $\mathbf{k}_c : \{k_y = 0, \pi, \text{ or } k_x = \pm \arccos(-2t \cos k_y \cos q / \mu)\}$ . For the values of  $q$  and  $\mu$  used in Fig. 7, we obtain the simple relation  $\mathbf{k}_c : \{k_y = 0, \pi, \text{ or } k_x = \pm k_y\}$ . For the gap-closing points  $\mathbf{k}_c = (k_x, 0)$  and  $(k_x, \pi)$  we straightforwardly find the gap-closing criterion  $\xi_{\mathbf{k}_{\mathcal{R}_{xz}}; -q_1} \xi_{\mathbf{k}_{\mathcal{R}_{xz}}; +q_1} = M_\sigma^2$ . When the magnetic wave vector  $\mathcal{Q}_1$  coincides with the nesting vector  $\mathcal{Q}_N$ , we observe that the spectrum is nodal even for  $M_\perp = M_\parallel = 0$  with

$k_c = (0, 0)$  and  $(0, \pi)$ . For a nonzero  $M_{\perp, \parallel}$  the nodes move along the  $xz$  HSPs. The remaining set of nodes, i.e., the ones moving along the lines  $k_x = \pm k_y$ , appear for  $M_\sigma^2 = \sqrt{\xi_{k-q_1} \xi_{k+q_1} + \Delta_{k-q_1} \Delta_{k+q_1}}$ . Similar to the nodes moving along the HSPs  $k_y = \{0, \pi\}$ , also here we find a nodal spectrum for  $M_\perp = M_\parallel = 0$  for  $k_x = \pm k_y = q$  and  $q + \pi$ . Upon increasing  $M_{\perp, \parallel}$  the nodes move along the lines  $k_x = \pm k_y$ .

In Fig. 25 we sketch the path of the nodes, the vorticities, and resulting edge spectra. As seen in Fig. 25(a), already in the absence of the MHC, the spectrum contains zeros which are enforced by the symmetry of  $\Delta_k$ . These give rise to topologically protected MFBs. This is exemplified in Fig. 25(b) using open boundary conditions in the  $y$  axis. Since in this case  $M_{\perp, \parallel} = 0$ , we show the original BZ. After switching on magnetism and transferring to the MBZ, we observe in Fig. 25(c) that the nodes split and start to move on straight lines as we vary the pairing and magnetic gaps. This splitting lifts the preexisting MFBs on edges perpendicular to the  $\mathbf{Q}$  vector, as a consequence of the canceling vorticities. This becomes more transparent by comparing Figs. 25(b) and 25(d). Instead, for edges parallel to the  $\mathbf{Q}$  vector, we recover the MFBs in Fig. 25(b), but we also obtain newly established MFBs stemming from the split nodes. This is illustrated in

Fig. 25(e), where we show the same as in Fig. 25(b) but now in the MBZ, and in Fig. 25(f) with  $M_{\perp, \parallel} \neq 0$ .

#### APPENDIX D: FUNCTIONS FOR THE REPRESENTATION OF THE BDG HAMILTONIAN IN 2D

The matrix function  $\hat{F}(f_k)$  has the form

$$\begin{aligned}
 \hat{F}(f_k) = & f_k^{(0,0)} + f_k^{(0,1)} \rho_2 + f_k^{(0,2)} \eta_3 + f_k^{(0,3)} \eta_3 \rho_2 \\
 & + \lambda_2 [f_k^{(1,0)} + f_k^{(1,1)} \rho_2 + f_k^{(1,2)} \eta_3 + f_k^{(1,3)} \eta_3 \rho_2] \\
 & + \zeta_3 [f_k^{(2,0)} + f_k^{(2,1)} \rho_2 + f_k^{(2,2)} \eta_3 + f_k^{(2,3)} \eta_3 \rho_2] \\
 & + \zeta_3 \lambda_2 [f_k^{(3,0)} + f_k^{(3,1)} \rho_2 + f_k^{(3,2)} \eta_3 + f_k^{(3,3)} \eta_3 \rho_2],
 \end{aligned}$$

with the functions  $f_k^{(t,s)} = (-1)^{s+t} f_{-k}$  defined as

$$\begin{aligned}
 f_k^{(0,s)} &= [f_{k-q_2}^{(s)} + f_{k+q_2}^{(s)} + f_{k+3q_2}^{(s)} + f_{k-3q_2}^{(s)}] / 4, \\
 f_k^{(1,s)} &= [f_{k-q_2}^{(s)} - f_{k+q_2}^{(s)} + f_{k+3q_2}^{(s)} - f_{k-3q_2}^{(s)}] / 4, \\
 f_k^{(2,s)} &= [f_{k-q_2}^{(s)} + f_{k+q_2}^{(s)} - f_{k+3q_2}^{(s)} - f_{k-3q_2}^{(s)}] / 4, \\
 f_k^{(3,s)} &= [f_{k-q_2}^{(s)} - f_{k+q_2}^{(s)} - f_{k+3q_2}^{(s)} + f_{k-3q_2}^{(s)}] / 4.
 \end{aligned}$$

- 
- [1] M. Z. Hasan and C. L. Kane, Colloquium: Topological insulators, *Rev. Mod. Phys.* **82**, 3045 (2010).
- [2] X.-L. Qi and S.-C. Zhang, Topological insulators and superconductors, *Rev. Mod. Phys.* **83**, 1057 (2011).
- [3] J. Alicea, New directions in the pursuit of majorana fermions in solid state systems, *Rep. Prog. Phys.* **75**, 076501 (2012).
- [4] C. W. J. Beenakker, Search for majorana fermions in superconductors, *Annu. Rev. Condens. Matter Phys.* **4**, 113 (2013).
- [5] M. Leijnse and K. Flensberg, Introduction to topological superconductivity and majorana fermions, *Semicond. Sci. Technol.* **27**, 124003 (2012).
- [6] Y. Tanaka, M. Sato, and N. Nagaosa, Symmetry and topology in superconductors - odd-frequency pairing and edge states, *J. Phys. Soc. Jpn.* **81**, 011013 (2012).
- [7] Y. Ando and L. Fu, Topological crystalline insulators and topological superconductors: From concepts to materials, *Annu. Rev. Condens. Matter Phys.* **6**, 361 (2015).
- [8] S. R. Elliott and M. Franz, Colloquium: Majorana fermions in nuclear, particle, and solid-state physics, *Rev. Mod. Phys.* **87**, 137 (2015).
- [9] R. Aguado, Majorana quasiparticles in condensed matter, *Riv. Nuovo Cimento* **40**, 523 (2017).
- [10] M. Sato and Y. Ando, Topological superconductors: A review, *Rep. Prog. Phys.* **80**, 076501 (2017).
- [11] R. M. Lutchyn, E. P. A. M. Bakkers, L. P. Kouwenhoven, P. Krogstrup, C. M. Marcus, and Y. Oreg, Realizing majorana zero modes in superconductor-semiconductor heterostructures, *Nat. Rev. Mater.* **3**, 52 (2018).
- [12] R. Pawlak, S. Hoffman, J. Klinovaja, D. Loss, and E. Meyer, Majorana fermions in magnetic chains, *Prog. Part. Nucl. Phys.* **107**, 1 (2019).
- [13] E. Prada, P. San-Jose, M. W. A. de Moor, A. Geresdi, E. J. H. Lee, J. Klinovaja, D. Loss, J. Nygård, R. Aguado, and L. P. Kouwenhoven, From andreev to majorana bound states in hybrid superconductor-semiconductor nanowires, *Nat. Rev. Phys.* **2**, 575 (2020).
- [14] E. Majorana, Teoria simmetrica dell'Elettrone e del positrone, *Nuovo Cimento* **14**, 171 (1937).
- [15] F. Wilczek, Majorana returns, *Nat. Phys.* **5**, 614 (2009).
- [16] N. Read and D. Green, Paired states of fermions in two dimensions with breaking of parity and time-reversal symmetries, and the fractional quantum Hall effect, *Phys. Rev. B* **61**, 10267 (2000).
- [17] G. E. Volovik, Fermion zero modes on vortices in chiral superconductors, *Zh. Eksp. Teor. Fiz.* **70**, 601 (1999) [*JETP Lett.* **70**, 609 (1999)].
- [18] D. A. Ivanov, Non-Abelian Statistics of Half-Quantum Vortices in P-Wave Superconductors, *Phys. Rev. Lett.* **86**, 268 (2001).
- [19] A. Y. Kitaev, Unpaired Majorana fermions in quantum wires, *Phys. Usp.* **44**, 131 (2001).
- [20] G. E. Volovik, *The Universe in a Helium Droplet* (Oxford University Press, Oxford, 2003).
- [21] A. Altland and M. R. Zirnbauer, Nonstandard symmetry classes in mesoscopic normal-superconducting hybrid structures, *Phys. Rev. B* **55**, 1142 (1997).
- [22] A. P. Schnyder, S. Ryu, A. Furusaki, and A. W. W. Ludwig, Classification of topological insulators and superconductors in three spatial dimensions, *Phys. Rev. B* **78**, 195125 (2008).
- [23] A. Kitaev, *Periodic Table for Topological Insulators and Superconductors*, AIP Conference Proceedings Volume 1134 (AIP, Melville, NY, 2009), p. 22.

- [24] S. Ryu, A. P. Schnyder, A. Furusaki, and A. W. W. Ludwig, Topological insulators and superconductors: Ten-fold way and dimensional hierarchy, *New J. Phys.* **12**, 065010 (2010).
- [25] J. C. Y. Teo and C. L. Kane, Topological defects and gapless modes in insulators and superconductors, *Phys. Rev. B* **82**, 115120 (2010).
- [26] A. Y. Kitaev, Fault-tolerant quantum computation by anyons, *Ann. Phys.* **303**, 2 (2003).
- [27] C. Nayak, S. H. Simon, A. Stern, M. Freedman, and S. Das Sarma, Non-abelian anyons and topological quantum computation, *Rev. Mod. Phys.* **80**, 1083 (2008).
- [28] J. Alicea, Y. Oreg, G. Refael, F. von Oppen, and M. P. A. Fisher, Non-abelian statistics and topological quantum information processing in 1D wire networks, *Nat. Phys.* **7**, 412 (2011).
- [29] J. D. Sau, D. J. Clarke, and S. Tewari, Controlling non-abelian statistics of majorana fermions in semiconductor nanowires, *Phys. Rev. B* **84**, 094505 (2011).
- [30] B. Van Heck, A. Akhmerov, F. Hassler, M. Burrello, and C. W. J. Beenakker, Coulomb-assisted braiding of Majorana fermions in a Josephson junction array, *New J. Phys.* **14**, 035019 (2012).
- [31] D. Aasen, M. Hell, R. V. Mishmash, A. Higginbotham, J. Danon, M. Leijnse, T. S. Jespersen, J. A. Folk, C. M. Marcus, K. Flensberg, and J. Alicea, Milestones Toward Majorana-Based Quantum Computing, *Phys. Rev. X* **6**, 031016 (2016).
- [32] T. Karzig, C. Knapp, R. M. Lutchyn, P. Bonderson, M. B. Hastings, C. Nayak, J. Alicea, K. Flensberg, S. Plugge, Y. Oreg, C. M. Marcus, and M. H. Freedman, Scalable designs for quasiparticle-poisoning-protected topological quantum computation with majorana zero modes, *Phys. Rev. B* **95**, 235305 (2017).
- [33] T. Li, W. A. Coish, M. Hell, K. Flensberg, and M. Leijnse, Four-Majorana qubit with charge readout: Dynamics and decoherence, *Phys. Rev. B* **98**, 205403 (2018).
- [34] T. Karzig, Y. Oreg, G. Refael, and M. H. Freedman, Robust Majorana magic gates via measurements, *Phys. Rev. B* **99**, 144521 (2019).
- [35] M. Sato, Non-abelian statistics of axion strings, *Phys. Lett. B* **575**, 126 (2003).
- [36] L. Fu and C. L. Kane, Superconducting Proximity Effect and Majorana Fermions at the Surface of a Topological Insulator, *Phys. Rev. Lett.* **100**, 096407 (2008).
- [37] C. Zhang, S. Tewari, R. Lutchyn, and S. Das Sarma,  $p_x + ip_y$  Superfluid from s-Wave Interactions of Fermionic Cold Atoms, *Phys. Rev. Lett.* **101**, 160401 (2008).
- [38] M. Sato, Y. Takahashi, and S. Fujimoto, Non-Abelian Topological Order in s-Wave Superfluids of Ultracold Fermionic Atoms, *Phys. Rev. Lett.* **103**, 020401 (2009).
- [39] J. D. Sau, R. M. Lutchyn, S. Tewari, and S. Das Sarma, Generic New Platform for Topological Quantum Computation Using Semiconductor Heterostructures, *Phys. Rev. Lett.* **104**, 040502 (2010).
- [40] Z. Wang, P. Zhang, G. Xu, L. K. Zeng, H. Miao, X. Xu, T. Qian, H. Weng, P. Richard, A. V. Fedorov, H. Ding, X. Dai, and Z. Fang, Topological nature of the  $\text{FeSe}_{0.5}\text{Te}_{0.5}$  superconductor, *Phys. Rev. B* **92**, 115119 (2015).
- [41] G. Xu, B. Lian, P. Tang, X.-L. Qi, and S.-C. Zhang, Topological Superconductivity on the Surface of Fe-Based Superconductors, *Phys. Rev. Lett.* **117**, 047001 (2016).
- [42] C. Chan, L. Zhang, T. F. Jeffrey Poon, Y.-P. He, Y.-Q. Wang, and X.-J. Liu, A Generic Theory for Majorana Zero Modes in 2D Superconductors, *Phys. Rev. Lett.* **119**, 047001 (2017).
- [43] K. Jiang, X. Dai, and Z. Wang, Quantum Anomalous Vortex and Majorana Zero Mode in Iron-Based Superconductor  $\text{Fe}(\text{Te},\text{Se})$ , *Phys. Rev. X* **9**, 011033 (2019).
- [44] D. Steffensen, B. M. Andersen, and P. Kotetes, Trapping Majorana zero modes in vortices of magnetic texture crystals coupled to nodal superconductors, *Phys. Rev. B* **104**, 174502 (2021).
- [45] J. C. Y. Teo and T. L. Hughes, Existence of Majorana-Fermion Bound States on Disclinations and the Classification of Topological Crystalline Superconductors in Two Dimensions, *Phys. Rev. Lett.* **111**, 047006 (2013).
- [46] S. Rex, I. V. Gornyi, and A. D. Mirlin, Majorana modes in emergent-wire phases of helical and cycloidal magnet-superconductor hybrids, *Phys. Rev. B* **102**, 224501 (2020).
- [47] J. C. Y. Teo and C. L. Kane, Majorana Fermions and Non-Abelian Statistics in Three Dimensions, *Phys. Rev. Lett.* **104**, 046401 (2010).
- [48] M. Wimmer, A. R. Akhmerov, M. V. Medvedeva, J. Tworzydło, and C. W. J. Beenakker, Majorana Bound States without Vortices in Topological Superconductors with Electrostatic Defects, *Phys. Rev. Lett.* **105**, 046803 (2010).
- [49] S. S. Pershoguba, S. Nakosai, and A. V. Balatsky, Skymion-induced bound states in a superconductor, *Phys. Rev. B* **94**, 064513 (2016).
- [50] G. Yang, P. Stano, J. Klinovaja, and D. Loss, Majorana bound states in magnetic skyrmions, *Phys. Rev. B* **93**, 224505 (2016).
- [51] K. M. D. Hals, M. Schechter, and M. S. Rudner, Composite Topological Excitations in Ferromagnet-Superconductor Heterostructures, *Phys. Rev. Lett.* **117**, 017001 (2016).
- [52] S. Rex, I. V. Gornyi, and A. D. Mirlin, Majorana bound states in magnetic skyrmions imposed onto a superconductor, *Phys. Rev. B* **100**, 064504 (2019).
- [53] M. Garnier, A. Mesaros, and P. Simon, Topological superconductivity with orbital effects in magnetic skyrmion based heterostructures, [arXiv:1909.12671](https://arxiv.org/abs/1909.12671).
- [54] M. Garnier, A. Mesaros, and P. Simon, Topological superconductivity with deformable magnetic skyrmions, *Commun. Phys.* **2**, 126 (2019).
- [55] V. Mourik, K. Zuo, S. M. Frolov, S. R. Plissard, E. P. A. M. Bakkers, and L. P. Kouwenhoven, Signatures of Majorana fermions in hybrid superconductor-semiconductor nanowire devices, *Science* **336**, 1003 (2012).
- [56] M. T. Deng, C. L. Yu, G. Y. Huang, M. Larsson, P. Caroff, and H. Q. Xu, Observation of majorana fermions in a Nb-InSb nanowire-nb hybrid quantum device, *Nano Lett.* **12**, 6414 (2012).
- [57] A. Das, Y. Ronen, Y. Most, Y. Oreg, M. Heiblum, and H. Shtrikman, Evidence of Majorana fermions in an Al - InAs nanowire topological superconductor, *Nat. Phys.* **8**, 887 (2012).
- [58] S. Nadj-Perge, I. K. Drozdov, Jian Li, Hua Chen, S. Jeon, J. Seo, A. H. MacDonald, B. A. Bernevig, and A. Yazdani, Observation of Majorana fermions in ferromagnetic atomic chains on a superconductor, *Science* **346**, 602 (2014).
- [59] S. Hart, H. Ren, T. Wagner, P. Leubner, M. Mühlbauer, C. Brüne, H. Buhmann, L. W. Molenkamp, and A. Yacoby,

- Induced superconductivity in the quantum spin hall edge, *Nat. Phys.* **10**, 638 (2014).
- [60] M. Ruby, F. Pientka, Y. Peng, F. von Oppen, B. W. Heinrich, and K. J. Franke, End States and Subgap Structure in Proximity-Coupled Chains of Magnetic Adatoms, *Phys. Rev. Lett.* **115**, 197204 (2015).
- [61] R. Pawlak, M. Kisiel, J. Klinovaja, T. Meier, S. Kawai, T. Glatzel, D. Loss, and E. Meyer, Probing atomic structure and majorana wavefunctions in mono-atomic Fe-chains on superconducting Pb-Surface, *npj Quantum Inf.* **2**, 16035 (2016).
- [62] J. Wiedenmann, E. Bocquillon, R. S. Deacon, S. Hartinger, O. Herrmann, T. M. Klapwijk, L. Maier, C. Ames, C. Brüne, C. Gould, A. Oiwa, K. Ishibashi, S. Tarucha, H. Buhmann, and L. W. Molenkamp,  $4\pi$ -periodic josephson supercurrent in HgTe-based topological josephson junctions, *Nat. Commun.* **7**, 10303 (2016).
- [63] M. T. Deng, S. Vaitikienas, E. B. Hansen, J. Danon, M. Leijnse, K. Flensberg, P. Krogstrup, and C. M. Marcus, Majorana bound state in a coupled quantum-dot hybrid-nanowire system, *Science* **354**, 1557 (2016).
- [64] S. M. Albrecht, A. P. Higginbotham, M. Madsen, F. Kuemmeth, T. S. Jespersen, J. Nygård, P. Krogstrup, and C. M. Marcus, Exponential protection of zero modes in Majorana islands, *Nature (London)* **531**, 206 (2016).
- [65] F. Nichele, A. C. C. Drachmann, A. M. Whiticar, E. C. T. O'Farrell, H. J. Suominen, A. Fomieri, T. Wang, G. C. Gardner, C. Thomas, A. T. Hatke, P. Krogstrup, M. J. Manfra, K. Flensberg, and C. M. Marcus, Scaling of Majorana Zero-Bias Conductance Peaks, *Phys. Rev. Lett.* **119**, 136803 (2017).
- [66] S. Jeon, Y. Xie, J. Li, Z. Wang, B. A. Bernevig, and A. Yazdani, Distinguishing a Majorana zero mode using spin-resolved measurements, *Science* **358**, 772 (2017).
- [67] G. C. Ménard, S. Guissart, C. Brun, R. T. Leriche, M. Trif, F. Debontridder, D. Demaille, D. Roditchev, P. Simon, and T. Cren, Two-dimensional topological superconductivity in Pb/Co/Si(111), *Nat. Commun.* **8**, 2040 (2017).
- [68] H. Zhang, C.-X. Liu, S. Gazibegovic, D. Xu, J. A. Logan, G. Wang, N. van Loo, J. D. S. Bommer, M. W. A. de Moor, D. Car, R. L. M. Op het Veld, P. J. van Veldhoven, S. Koelling, M. A. Verheijen, M. Pendharkar, D. J. Pennachio, B. Shojaei, J. S. Lee, C. J. Palmstrom, E. P. A. M. Bakkers, S. D. Sarma *et al.*, RETRACTED ARTICLE: Quantized Majorana conductance, *Nature (London)* **556**, 74 (2018).
- [69] H. Kim, A. Palacio-Morales, T. Posske, L. Rózsa, K. Palotás, L. Szunyogh, M. Thorwart, and R. Wiesendanger, Toward tailoring Majorana bound states in artificially constructed magnetic atom chains on elemental superconductors, *Sci. Adv.* **4**, eaar5251 (2018).
- [70] D. Laroche, D. Bouman, D. J. van Woerkom, A. Proutski, C. Murthy, D. I. Pikulin, C. Nayak, R. J. J. van Gulik, J. Nygård, P. Krogstrup, L. P. Kouwenhoven, and A. Geresdi, Observation of the  $4\pi$ -periodic josephson effect in indium arsenide nanowires, *Nat. Commun.* **10**, 245 (2019).
- [71] G. C. Ménard, A. Mesaros, C. Brun, F. Debontridder, D. Roditchev, P. Simon, and T. Cren, Isolated pairs of Majorana zero modes in a disordered superconducting lead monolayer, *Nat. Commun.* **10**, 2587 (2019).
- [72] M. M. Desjardins, L. C. Contamin, M. R. Delbecq, M. C. Dartailh, L. E. Bruhat, T. Cubaynes, J. J. Viennot, F. Mallet, S. Rohart, A. Thiaville, A. Cottet, and T. Kontos, Synthetic spin orbit interaction for Majorana devices, *Nat. Mater.* **18**, 1060 (2019).
- [73] S. Manna, P. Wei, Y. Xie, K. T. Law, P. Lee, and J. Moodera, Signature of a pair of Majorana zero modes in superconducting gold surface states, *Proc. Natl. Acad. Sci. USA* **117**, 8775 (2020).
- [74] L. Schneider, S. Brinker, M. Steinbrecher, J. Hermenau, T. Posske, M. dos Santos Dias, S. Lounis, R. Wiesendanger, and J. Wiebe, Controlling in-gap end states by linking non-magnetic atoms and artificially-constructed spin chains on superconductors, *Nat. Commun.* **11**, 4707 (2020).
- [75] J. Alicea, Majorana fermions in a tunable semiconductor device, *Phys. Rev. B* **81**, 125318 (2010).
- [76] R. M. Lutchyn, J. D. Sau, and S. Das Sarma, Majorana Fermions and a Topological Phase Transition in Semiconductor-Superconductor Heterostructures, *Phys. Rev. Lett.* **105**, 077001 (2010).
- [77] Y. Oreg, G. Refael, and F. von Oppen, Helical Liquids and Majorana Bound States in Quantum Wires, *Phys. Rev. Lett.* **105**, 177002 (2010).
- [78] P. M. R. Brydon, S. Das Sarma, H.-Y. Hui, and J. D. Sau, Topological Yu-shiba-rusinov chain from spin-orbit coupling, *Phys. Rev. B* **91**, 064505 (2015).
- [79] J. Li, H. Chen, I. K. Drozdov, A. Yazdani, B. A. Bernevig, and A. H. MacDonald, Topological superconductivity induced by ferromagnetic metal chains, *Phys. Rev. B* **90**, 235433 (2014).
- [80] A. Heimes, D. Mandler, and P. Kotetes, Interplay of topological phases in magnetic adatom-chains on top of a rashba superconducting surface, *New J. Phys.* **17**, 023051 (2015).
- [81] T. Čadež and P. D. Sacramento, Zero energy modes in a superconductor with ferromagnetic adatom chains and quantum phase transitions, *J. Phys.: Condens. Matter* **28**, 495703 (2016).
- [82] T.-P. Choy, J. M. Edge, A. R. Akhmerov, and C. W. J. Beenakker, Majorana fermions emerging from magnetic nanoparticles on a superconductor without spin-orbit coupling, *Phys. Rev. B* **84**, 195442 (2011).
- [83] M. Kjaergaard, K. Wölms, and K. Flensberg, Majorana fermions in superconducting nanowires without spin-orbit coupling, *Phys. Rev. B* **85**, 020503(R) (2012).
- [84] I. Martin and A. F. Morpurgo, Majorana fermions in superconducting helical magnets, *Phys. Rev. B* **85**, 144505 (2012).
- [85] J. Klinovaja and D. Loss, Giant Spin-Orbit Interaction Due to Rotating Magnetic Fields in Graphene Nanoribbons, *Phys. Rev. X* **3**, 011008 (2013).
- [86] S. Nadj-Perge, I. K. Drozdov, B. A. Bernevig, and A. Yazdani, Proposal for realizing majorana fermions in chains of magnetic atoms on a superconductor, *Phys. Rev. B* **88**, 020407(R) (2013).
- [87] S. Nakosai, Y. Tanaka, and N. Nagaosa, Two-dimensional p-wave superconducting states with magnetic moments on a conventional S-wave superconductor, *Phys. Rev. B* **88**, 180503(R) (2013).
- [88] P. Kotetes, Classification of engineered topological superconductors, *New J. Phys.* **15**, 105027 (2013).
- [89] B. Braunecker and P. Simon, Interplay between Classical Magnetic Moments and Superconductivity in Quantum One-Dimensional Conductors: Toward a Self-Sustained Topological Majorana Phase, *Phys. Rev. Lett.* **111**, 147202 (2013);

- J. Klinovaja, P. Stano, A. Yazdani, and D. Loss, Topological Superconductivity and Majorana Fermions in RKKY Systems, *ibid.* **111**, 186805 (2013); M. M. Vazifeh and M. Franz, Self-Organized Topological State with Majorana Fermions, *ibid.* **111**, 206802 (2013).
- [90] F. Pientka, L. I. Glazman, and F. von Oppen, Topological Superconducting Phase in Helical Shiba Chains, Unconventional topological phase transitions in helical Shiba chains, *Phys. Rev. B* **88**, 155420 (2013); **89**, 180505(R) (2014).
- [91] K. Pöyhönen, A. Westström, J. Röntynen, and T. Ojanen, Majorana states in helical shiba chains and ladders, *Phys. Rev. B* **89**, 115109 (2014).
- [92] N. Sedlmayr, J. M. Aguiar-Hualde, and C. Bena, Flat Majorana bands in 2D lattices with inhomogeneous magnetic fields: Topology and stability, *Phys. Rev. B* **91**, 115415 (2015).
- [93] W. Chen and A. P. Schnyder, Majorana edge states in superconductor-noncollinear magnet interfaces, *Phys. Rev. B* **92**, 214502 (2015).
- [94] J. Xiao and J. An, Chiral symmetries and majorana fermions in coupled magnetic atomic chains on a superconductor, *New J. Phys.* **17**, 113034 (2015).
- [95] M. Schechter, K. Flensberg, M. H. Christensen, B. M. Andersen, and J. Paaske, Self-organized topological superconductivity in a Yu-Shiba-Rusinov chain, *Phys. Rev. B* **93**, 140503(R) (2016); M. H. Christensen, M. Schechter, K. Flensberg, B. M. Andersen, and J. Paaske, Spiral magnetic order and topological superconductivity in a chain of magnetic adatoms on a 2D superconductor, *ibid.* **94**, 144509 (2016).
- [96] G. L. Fatim, A. Matos-Abiague, B. Scharf, and I. Žutić, Wireless Majorana Bound States: From Magnetic Tunability to Braiding, *Phys. Rev. Lett.* **117**, 077002 (2016); T. Zhou, N. Mohanta, J. E. Han, A. Matos-Abiague, and I. Žutić, Tunable magnetic textures in spin valves: From spintronics to Majorana bound states, *Phys. Rev. B* **99**, 134505 (2019).
- [97] P. Marra and M. Cuoco, Controlling Majorana states in topologically inhomogeneous superconductors, *Phys. Rev. B* **95**, 140504(R) (2017).
- [98] N. Mohanta, T. Zhou, J.-W. Xu, J. E. Han, A. D. Kent, J. Shabani, I. Žutić, and A. Matos-Abiague, Electrical Control of Majorana Bound States Using Magnetic Stripes, *Phys. Rev. Appl.* **12**, 034048 (2019).
- [99] E. Mascot, J. Bedow, M. Graham, S. Rachel, and D. K. Morr, Topological Superconductivity in Skyrmion Lattices, *npj Quantum Mater.* **6**, 6 (2021).
- [100] J. Bedow, E. Mascot, T. Posske, G. S. Uhrig, R. Wiesendanger, S. Rachel, and D. K. Morr, Topological superconductivity induced by a triple-Q magnetic structure, *Phys. Rev. B* **102**, 180504(R) (2020).
- [101] G.-Y. Huang, B. Li, X.-F. Yi, J.-B. Fu, X. Fu, X.-G. Qiang, P. Xu, J.-J. Wu, C.-L. Yu, P. Kotetes, and M.-T. Deng, Field-programmable topological array: Framework and case-studies, [arXiv:2010.02130](https://arxiv.org/abs/2010.02130).
- [102] N. Mohanta, S. Okamoto, and E. Dagotto, Skyrmion control of Majorana states in planar josephson junctions, *Commun. Phys.* **4**, 163 (2021).
- [103] A. Heimes, P. Kotetes, and G. Schön, Majorana fermions from shiba states in an antiferromagnetic chain on top of a superconductor, *Phys. Rev. B* **90**, 060507(R) (2014).
- [104] G. Livanas, M. Sigrist, and G. Varelogiannis, Alternative paths to realize Majorana fermions in superconductor-ferromagnet heterostructures, *Sci. Rep.* **9**, 6259 (2019).
- [105] B. Braunecker, G. I. Japaridze, J. Klinovaja, and D. Loss, Spin-selective Peierls transition in interacting 1D conductors with spin-orbit interaction, *Phys. Rev. B* **82**, 045127 (2010).
- [106] A. Palacio-Morales, E. Mascot, S. Cocklin, H. Kim, S. Rachel, D. K. Morr, and R. Wiesendanger, Atomic-scale interface engineering of Majorana edge modes in a 2D magnet-superconductor hybrid system, *Sci. Adv.* **5**, eaav6600 (2019).
- [107] A. Kubetzka, J. M. Bürger, R. Wiesendanger, and K. von Bergmann, Towards skyrmion superconductor hybrid systems, *Phys. Rev. Mater.* **4**, 081401(R) (2020).
- [108] A. P. Petrović, M. Raju, X. Y. Tee, A. Louat, I. Maggio-Aprile, R. M. Menezes, M. J. Wyszyński, N. K. Duong, M. Reznikov, Ch. Renner, M. V. Milošević, and C. Panagopoulos, Skyrmion-(Anti)Vortex Coupling in a Chiral Magnet-Superconductor Heterostructure, *Phys. Rev. Lett.* **126**, 117205 (2021).
- [109] N. Ni, M. E. Tillman, J.-Q. Yan, A. Kracher, S. T. Hannahs, S. L. Bud'ko, and P. C. Canfield, Effects of Co substitution on thermodynamic and transport properties and anisotropic  $H_{c2}$  in  $\text{Ba}(\text{Fe}_{1-x}\text{Co}_x)_2\text{As}_2$  single crystals, *Phys. Rev. B* **78**, 214515 (2008).
- [110] S. Nandi, M. G. Kim, A. Kreyssig, R. M. Fernandes, D. K. Pratt, A. Thaler, N. Ni, S. L. Bud'ko, P. C. Canfield, J. Schmalian, R. J. McQueeney, and A. I. Goldman, Anomalous Suppression of the Orthorhombic Lattice Distortion in Superconducting  $\text{Ba}(\text{Fe}_{1-x}\text{Co}_x)_2\text{As}_2$  Single Crystals, *Phys. Rev. Lett.* **104**, 057006 (2010).
- [111] E. Wiesenmayer, H. Luetkens, G. Pascua, R. Khasanov, A. Amato, H. Potts, B. Banusch, H.-H. Klauss, and D. Johrendt, Microscopic Coexistence of Superconductivity and Magnetism in  $\text{Ba}_{1-x}\text{K}_x\text{Fe}_2\text{As}_2$ , *Phys. Rev. Lett.* **107**, 237001 (2011).
- [112] S. Avci, O. Chmaissem, E. A. Goremychkin, S. Rosenkranz, J.-P. Castellan, D. Y. Chung, I. S. Todorov, J. A. Schlueter, H. Claus, M. G. Kanatzidis, A. Daoud-Aladine, D. Khalyavin, and R. Osborn, Magnetoelastic coupling in the phase diagram of  $\text{Ba}_{1-x}\text{K}_x\text{Fe}_2\text{As}_2$  as seen via neutron diffraction, *Phys. Rev. B* **83**, 172503 (2011).
- [113] E. Hassinger, G. Gredat, F. Valade, S. R. de Cotret, A. Juneau-Fecteau, J.-P. Reid, H. Kim, M. A. Tanatar, R. Prozorov, B. Shen, H.-H. Wen, N. Doiron-Leyraud, and L. Taillefer, Pressure-induced Fermi-surface reconstruction in the iron-arsenide superconductor  $\text{Ba}_{1-x}\text{K}_x\text{Fe}_2\text{As}_2$ : Evidence of a phase transition inside the antiferromagnetic phase, *Phys. Rev. B* **86**, 140502(R) (2012).
- [114] S. Avci, O. Chmaissem, J. M. Allred, S. Rosenkranz, I. Eremin, A. V. Chubukov, D. E. Bugaris, D. Y. Chung, M. G. Kanatzidis, J.-P. Castellan, J. A. Schlueter, H. Claus, D. D. Khalyavin, P. Manuel, A. Daoud-Aladine, and R. Osborn, Magnetically driven suppression of nematic order in an iron-based superconductor, *Nat. Commun.* **5**, 3845 (2014).
- [115] A. E. Böhmer, F. Hardy, L. Wang, T. Wolf, P. Schweiss, and C. Meingast, Superconductivity-induced re-entrance of the orthorhombic distortion in  $\text{Ba}_{1-x}\text{K}_x\text{Fe}_2\text{As}_2$ , *Nat. Commun.* **6**, 7911 (2015).

- [116] F. Waßer, A. Schneidewind, Y. Sidis, S. Wurmehl, S. Aswartham, B. Büchner, and M. Braden, Spin reorientation in  $\text{Ba}_{0.65}\text{Na}_{0.35}\text{Fe}_2\text{As}_2$  studied by single-crystal neutron diffraction, *Phys. Rev. B* **91**, 060505(R) (2015).
- [117] J. M. Allred, S. Avcı, Y. Chung, H. Claus, D. D. Khalyavin, P. Manuel, K. M. Taddei, M. G. Kanatzidis, S. Rosenkranz, R. Osborn, and O. Chmaissem, Tetragonal magnetic phase in  $\text{Ba}_{1-x}\text{K}_x\text{Fe}_2\text{As}_2$  from x-ray and neutron diffraction, *Phys. Rev. B* **92**, 094515 (2015).
- [118] J. M. Allred, K. M. Taddei, D. E. Bugaris, M. J. Krogstad, S. H. Lapidus, D. Y. Chung, H. Claus, M. G. Kanatzidis, D. E. Brown, J. Kang, R. M. Fernandes, I. Eremin, S. Rosenkranz, O. Chmaissem, and R. Osborn, Double-Q spin-density wave in iron arsenide superconductors, *Nat. Phys.* **12**, 493 (2016).
- [119] B. P. P. Mallett, Y. G. Pashkevich, A. Gusev, T. Wolf, and C. Bernhard, Muon spin rotation study of the magnetic structure in the tetragonal antiferromagnetic state of weakly underdoped  $\text{Ba}_{1-x}\text{K}_x\text{Fe}_2\text{As}_2$ , *Europhys. Lett.* **111**, 57001 (2015).
- [120] P. Materne, S. Kamusella, R. Sarkar, T. Goltz, J. Spehling, H. Maeter, L. Harnagea, S. Wurmehl, B. Büchner, H. Luetkens, C. Timm, and H.-H. Klauss, Coexistence of superconductivity and magnetism in  $\text{Ca}_{1-x}\text{Na}_x\text{Fe}_2\text{As}_2$ : Universal suppression of the magnetic order parameter in 122 iron pnictides, *Phys. Rev. B* **92**, 134511 (2015).
- [121] B. P. P. Mallett, P. Marsik, M. Yazdi-Rizi, T. Wolf, A. E. Böhmer, F. Hardy, C. Meingast, D. Munzar, and C. Bernhard, Infrared Study of the Spin Reorientation Transition and Its Reversal in the Superconducting State in Underdoped  $\text{Ba}_{1-x}\text{K}_x\text{Fe}_2\text{As}_2$ , *Phys. Rev. Lett.* **115**, 027003 (2015).
- [122] L. Wang, F. Hardy, A. E. Böhmer, T. Wolf, P. Schweiss, and C. Meingast, Complex phase diagram of  $\text{Ba}_{1-x}\text{Na}_x\text{Fe}_2\text{As}_2$ : A multitude of phases striving for the electronic entropy, *Phys. Rev. B* **93**, 014514 (2016).
- [123] Y. Zheng, P. M. Tam, J. Hou, A. E. Böhmer, T. Wolf, C. Meingast, and R. Lortz, Absence of nematic order in the pressure-induced intermediate phase of the iron-based superconductor  $\text{Ba}_{0.85}\text{K}_{0.15}\text{Fe}_2\text{As}_2$ , *Phys. Rev. B* **93**, 104516 (2016).
- [124] W. R. Meier, Q.-P. Ding, A. Kreyssig, S. L. Bud'ko, A. Sapkota, K. Kothapalli, V. Borisov, R. Valentí, C. D. Batista, P. P. Orth, R. M. Fernandes, A. I. Goldman, Y. Furukawa, A. E. Böhmer, and P. C. Canfield, Hedgehog spin-vortex crystal stabilized in a hole-doped iron-based superconductor, *npj Quantum Mater.* **3**, 5 (2018).
- [125] J. Lorenzana, G. Seibold, C. Ortix, and M. Grilli, Competing Orders in FeAs Layers, *Phys. Rev. Lett.* **101**, 186402 (2008).
- [126] I. Eremin and A. V. Chubukov, Magnetic degeneracy and hidden metallicity of the spin-density-wave state in ferropnictides, *Phys. Rev. B* **81**, 024511 (2010).
- [127] P. M. R. Brydon, J. Schmiedt, and C. Timm, Microscopically derived Ginzburg-Landau theory for magnetic order in the iron pnictides, *Phys. Rev. B* **84**, 214510 (2011).
- [128] G. Giovannetti, C. Ortix, M. Marsman, M. Capone, J. van den Brink, and J. Lorenzana, Proximity of iron pnictide superconductors to a quantum tricritical point, *Nat. Commun.* **2**, 398 (2011).
- [129] M. N. Gastiasoro and B. M. Andersen, Competing magnetic double-Q phases and superconductivity-induced reentrance of  $C_2$  magnetic stripe order in iron pnictides, *Phys. Rev. B* **92**, 140506(R) (2015).
- [130] X. Wang, J. Kang, and R. M. Fernandes, Magnetic order without tetragonal-symmetry-breaking in iron arsenides: Microscopic mechanism and spin-wave spectrum, *Phys. Rev. B* **91**, 024401 (2015).
- [131] J. Kang, X. Wang, A. V. Chubukov, and R. M. Fernandes, Interplay between tetragonal magnetic order, stripe magnetism, and superconductivity in iron-based materials, *Phys. Rev. B* **91**, 121104(R) (2015).
- [132] M. H. Christensen, J. Kang, B. M. Andersen, I. Eremin, and R. M. Fernandes, Spin reorientation driven by the interplay between spin-orbit coupling and Hund's rule coupling in iron pnictides, *Phys. Rev. B* **92**, 214509 (2015).
- [133] M. H. Christensen, D. D. Scherer, P. Kotetes, and B. M. Andersen, Role of multiorbital effects in the magnetic phase diagram of iron-pnictides, *Phys. Rev. B* **96**, 014523 (2017).
- [134] M. H. Christensen, B. M. Andersen, and P. Kotetes, Unravelling Incommensurate Magnetism and Its Emergence in Iron-Based Superconductors, *Phys. Rev. X* **8**, 041022 (2018).
- [135] J.-X. Yin, Zheng Wu, J.-H. Wang, Z.-Y. Ye, Jing Gong, X.-Y. Hou, Lei Shan, Ang Li, X.-J. Liang, X.-X. Wu, Jian Li, C.-S. Ting, Z. Wang, J.-P. Hu, P.-H. Hor, H. Ding, and S. H. Pan, Observation of a robust zero-energy bound state in iron-based superconductor Fe(Te, Se), *Nat. Phys.* **11**, 543 (2015).
- [136] P. Zhang, K. Yaji, T. Hashimoto, Y. Ota, T. Kondo, K. Okazaki, Z. Wang, J. Wen, G. D. Gu, H. Ding, and S. Shin, Observation of topological superconductivity on the surface of iron-based superconductor, *Science* **360**, 182 (2018).
- [137] D. Wang, L. Kong, P. Fan, H. Chen, S. Zhu, W. Liu, L. Cao, Y. Sun, S. Du, J. Schneeloch, R. Zhong, G. Gu, L. Fu, H. Ding, and H.-J. Gao, Observation of pristine Majorana bound state in iron-based superconductor, *Science* **362**, 333 (2018).
- [138] L. Kong, S. Zhu, M. Papaj, L. Cao, H. Isobe, W. Liu, D. Wang, P. Fan, H. Chen, Y. Sun, S. Du, J. Schneeloch, R. Zhong, G. Gu, L. Fu, H.-J. Gao, and H. Ding, Observation of half-integer level shift of vortex bound states in an iron-based superconductor, *Nat. Phys.* **15**, 1181 (2019).
- [139] S. Zhu, L. Kong, L. Cao, H. Chen, M. Papaj, S. Du, Y. Xing, W. Liu, D. Wang, C. Shen, F. Yang, J. Schneeloch, R. Zhong, G. Gu, L. Fu, Y.-Y. Zhang, H. Ding, and H.-J. Gao, Nearly quantized conductance plateau of vortex zero mode in an iron-based superconductor, *Science* **367**, 189 (2020).
- [140] J. Cano, B. Bradlyn, and M. G. Vergniory, Multifold nodal points in magnetic materials *APL Mater.* **7**, 101125 (2019).
- [141] Y. Xu, L. Elcoro, Z. Song, B. J. Wieder, M. G. Vergniory, N. Regnault, Y. Chen, C. Felser, and B. Andrei Bernevig, High-throughput calculations of antiferromagnetic topological materials from magnetic topological quantum chemistry, *Nature (London)* **586**, 702 (2020).
- [142] L. Elcoro, B. J. Wieder, Z. Song, Y. Xu, B. Bradlyn, and B. A. Bernevig, Magnetic topological quantum chemistry, *Nat. Commun.* **12**, 5965 (2021).
- [143] A. Bouhon, G. F. Lange, and R.-J. Slager, Topological correspondence between magnetic space group representations, *Phys. Rev. B* **103**, 245127 (2021).
- [144] L. Fu, Topological Crystalline Insulators, *Phys. Rev. Lett.* **106**, 106802 (2011).
- [145] T. H. Hsieh, H. Lin, J. Liu, W. Duan, A. Bansil, and L. Fu, Topological crystalline insulators in the SnTe material class, *Nat. Commun.* **3**, 982 (2012); Y. Tanaka, Z. Ren, T. Sato, K. Nakayama, S. Souma, T. Takahashi, K. Segawa, and Y. Ando,

- Experimental realization of a topological crystalline insulator in SnTe, *Nat. Phys.* **8**, 800 (2012).
- [146] C.-K. Chiu, H. Yao, and S. Ryu, Classification of topological insulators and superconductors in the presence of reflection symmetry, *Phys. Rev. B* **88**, 075142 (2013).
- [147] T. Morimoto and A. Furusaki, Topological classification with additional symmetries from Clifford algebras, *Phys. Rev. B* **88**, 125129 (2013).
- [148] K. Shiozaki and M. Sato, Topology of crystalline insulators and superconductors, *Phys. Rev. B* **90**, 165114 (2014).
- [149] C.-K. Chiu and A. P. Schnyder, Classification of reflection symmetry protected topological semimetals and nodal superconductors, *Phys. Rev. B* **90**, 205136 (2014).
- [150] C. Fang, M. J. Gilbert, and A. B. Bernevig, New Class of Topological Superconductors Protected by Magnetic Group Symmetries, *Phys. Rev. Lett.* **112**, 106401 (2014).
- [151] R.-X. Zhang and C.-X. Liu, Topological magnetic crystalline insulators and corepresentation theory, *Phys. Rev. B* **91**, 115317 (2015).
- [152] D. Mendler, P. Kotetes, and G. Schön, Magnetic order on a topological insulator surface with warping and proximity-induced superconductivity, *Phys. Rev. B* **91**, 155405 (2015).
- [153] C.-K. Chiu, J. C. Y. Teo, A. P. Schnyder and S. Ryu, Classification of topological quantum matter with symmetries, *Rev. Mod. Phys.* **88**, 035005 (2016).
- [154] J. Kruthoff, J. de Boer, J. van Wezel, C. L. Kane, and R.-J. Slager, Topological Classification of Crystalline Insulators through Band Structure Combinatorics, *Phys. Rev. X* **7**, 041069 (2017).
- [155] E. J. König and P. Coleman, Crystalline Symmetry Protected Helical Majorana Modes in the Iron Pnictides, *Phys. Rev. Lett.* **122**, 207001 (2019).
- [156] J. Zou, Q. Xie, Z. Song, and G. Xu, New types of topological superconductors under local magnetic symmetries, *Nat. Sci. Rev.* **5**, nwaa169 (2021).
- [157] R. Ramazashvili, Kramers Degeneracy in a Magnetic Field and Zeeman Spin-Orbit Coupling in Antiferromagnetic Conductors, *Phys. Rev. Lett.* **101**, 137202 (2008).
- [158] R. S. K. Mong, A. M. Essin, and J. E. Moore, Antiferromagnetic topological insulators, *Phys. Rev. B* **81**, 245209 (2010).
- [159] R.-J. Slager, A. Mesaros, V. Juričić, and J. Zaanen, The space group classification of topological band-insulators, *Nat. Phys.* **9**, 98 (2013).
- [160] C. Fang, M. J. Gilbert, and B. A. Bernevig, Topological insulators with commensurate antiferromagnetism, *Phys. Rev. B* **88**, 085406 (2013).
- [161] Q.-Z. Wang and C.-X. Liu, Topological nonsymmorphic crystalline superconductors, *Phys. Rev. B* **93**, 020505 (2016).
- [162] K. Shiozaki, M. Sato, and K. Gomi, Topology of nonsymmorphic crystalline insulators and superconductors, *Phys. Rev. B* **93**, 195413 (2016).
- [163] Y. Yanase and K. Shiozaki, Möbius topological superconductivity in UPt<sub>3</sub>, *Phys. Rev. B* **95**, 224514 (2017); A. Daido, T. Yoshida, and Y. Yanase, Z<sub>4</sub> Topological Superconductivity in UCoGe, *Phys. Rev. Lett.* **122**, 227001 (2019).
- [164] R.-X. Zhang, W. S. Cole, X. Wu, and S. Das Sarma, Higher-Order Topology and Nodal Topological Superconductivity in Fe(Se, Te) Heterostructures, *Phys. Rev. Lett.* **123**, 167001 (2019).
- [165] G. Grüner, The dynamics of charge-density waves, *Rev. Mod. Phys.* **60**, 1129 (1988).
- [166] S. Raghu, X.-L. Qi, C.-X. Liu, D. J. Scalapino, and S.-C. Zhang, Minimal two-band model of the superconducting iron oxypnictides, *Phys. Rev. B* **77**, 220503(R) (2008).
- [167] H. Eschrig and K. Koepf, Tight-binding models for the iron-based superconductors, *Phys. Rev. B* **80**, 104503 (2009).
- [168] M. Daghofer, A. Nicholson, A. Moreo, and E. Dagotto, Three orbital model for the iron-based superconductors, *Phys. Rev. B* **81**, 014511 (2010).
- [169] H. Ikeda, R. Arita, and J. Kuneš, Phase diagram and gap anisotropy in iron-pnictide superconductors, *Phys. Rev. B* **81**, 054502 (2010).
- [170] S. Graser, A. F. Kemper, T. A. Maier, H.-P. Cheng, P. J. Hirschfeld, and D. J. Scalapino, Spin fluctuations and superconductivity in a three-dimensional tight-binding model for BaFe<sub>2</sub>As<sub>2</sub>, *Phys. Rev. B* **81**, 214503 (2010).
- [171] A. Aperis, P. Kotetes, G. Varelogiannis, and P. M. Oppeneer, Small-q phonon mediated unconventional superconductivity in the iron pnictides, *Phys. Rev. B* **83**, 092505 (2011).
- [172] V. Cvetkovic and O. Vafek, Space group symmetry, spin-orbit coupling, and the low-energy effective Hamiltonian for iron-based superconductors, *Phys. Rev. B* **88**, 134510 (2013).
- [173] N. Hao and J. Hu, Topological Phases in the Single-Layer FeSe, *Phys. Rev. X* **4**, 031053 (2014).
- [174] C. L. M. Wong, J. Liu, K. T. Law, and P. A. Lee, Majorana flat bands and unidirectional Majorana edge states in gapless topological superconductors, *Phys. Rev. B* **88**, 060504(R) (2013).
- [175] A. Daido and Y. Yanase, Majorana flat bands, chiral Majorana edge states, and unidirectional Majorana edge states in non-centrosymmetric superconductors, *Phys. Rev. B* **95**, 134507 (2017).
- [176] M. Biderang, H. Yavari, M.-H. Zare, P. Thalmeier, and A. Akbari, Edge currents as a probe of the strongly spin-polarized topological noncentrosymmetric superconductors, *Phys. Rev. B* **98**, 014524 (2018).
- [177] J. Klinovaja, P. Stano, and D. Loss, Transition from Fractional to Majorana Fermions in Rashba Nanowires, *Phys. Rev. Lett.* **109**, 236801 (2012).
- [178] D. Sticlet, L. Seabra, F. Pollmann, and J. Cayssol, From fractionally charged solitons to Majorana bound states in a one-dimensional interacting model, *Phys. Rev. B* **89**, 115430 (2014).
- [179] R. Wakatsuki, M. Ezawa, Y. Tanaka, and N. Nagaosa, Fermion fractionalization to Majorana fermions in dimerized kitaev superconductor, *Phys. Rev. B* **90**, 014505 (2014).
- [180] P. Marra and M. Nitta, Topologically nontrivial Andreev bound states, *Phys. Rev. B* **100**, 220502(R) (2019).
- [181] A. Zazunov, V. S. Shumeiko, E. N. Bratus', J. Lantz, and G. Wendin, Andreev Level Qubit, *Phys. Rev. Lett.* **90**, 087003 (2003).
- [182] A. P. Higginbotham, S. M. Albrecht, G. Kiršanskas, W. Chang, F. Kuemmeth, P. Krogstrup, T. S. Jespersen, J. Nygård, K. Flensberg, and C. M. Marcus, Parity lifetime of bound states in a proximitized semiconductor nanowire, *Nat. Phys.* **11**, 1017 (2015).
- [183] I. M. Lifshitz, Anomalies of electron characteristics of a metal in the high pressure region, *Zh. Eksp. Teor. Fiz.* **38**, 1569 (1960) [*Sov. Phys. JETP* **11**, 1130 (1960)].



- [184] G. E. Volovik, Exotic Lifshitz transitions in topological materials, *Phys. Usp.* **61**, 89 (2018).
- [185] S. Aubry and G. André, Analyticity breaking and Anderson localization in incommensurate lattices, *Ann. Israel Phys. Soc.* **3**, 133 (1980).
- [186] S. Tewari and J. D. Sau, Topological Invariants for Spin-Orbit Coupled Superconductor Nanowires, *Phys. Rev. Lett.* **109**, 150408 (2012).
- [187] K. Ishikawa and T. Matsuyama, A microscopic theory of the quantum Hall effect, *Nucl. Phys. B* **280**, 523 (1987).
- [188] X.-L. Qi, T. Hughes, and S.-C. Zhang, Topological field theory of time-reversal invariant insulators, *Phys. Rev. B* **78**, 195424 (2008).
- [189] C. L. Kane and E. J. Mele, Quantum Spin Hall Effect in Graphene, *Phys. Rev. Lett.* **95**, 226801 (2005).
- [190] D. N. Sheng, Z. Y. Weng, L. Sheng, and F. D. M. Haldane, Quantum Spin-Hall Effect and Topologically Invariant Chern Numbers, *Phys. Rev. Lett.* **97**, 036808 (2006).
- [191] B. A. Bernevig, T. L. Hughes, and S.-C. Zhang, Quantum spin Hall effect and topological phase transition in HgTe quantum wells, *Science* **314**, 1757 (2006).
- [192] L. Yu, Bound state in superconductors with paramagnetic impurities, *Acta Phys. Sin.* **21**, 75 (1965); H. Shiba, Classical spins in superconductors, *Prog. Theor. Phys.* **40**, 435 (1968); A. I. Rusinov, Theory of gapless superconductivity in alloys containing paramagnetic impurities, *Zh. Eksp. Teor. Fiz.* **56**, 2047 (1969) [*Sov. Phys. JETP* **29**, 1101 (1969)]; A. Sakurai, Comments on superconductors with magnetic impurities, *Prog. Theor. Phys.* **44**, 1472 (1970).
- [193] A. V. Balatsky, I. Vekhter, and J.-X. Zhu, Impurity-induced states in conventional and unconventional superconductors, *Rev. Mod. Phys.* **78**, 373 (2006).
- [194] D. Hsieh, Y. Xia, L. Wray, D. Qian, A. Pal, J. H. Dil, F. Meier, J. Osterwalder, G. Bihlmayer, C. L. Kane, Y. S. Hor, R. J. Cava, and M. Z. Hasan, First direct observation of Spin-textures in Topological Insulators: Spin-resolved ARPES as a probe of topological quantum spin Hall effect and Berry's phase, *Science* **323**, 919 (2009).
- [195] C. J. Bradley, and B. L. Davies, Magnetic groups and their corepresentations, *Rev. Mod. Phys.* **40**, 359 (1968).
- [196] C. J. Bradley and A. P. Cracknell, *The Mathematical Theory of Symmetry in Solids* (Clarendon, Oxford, 1972).
- [197] M. S. Dresselhaus, G. Dresselhaus, and A. Jorio, *Group Theory: Application to the Physics of Condensed Matter* (Springer, Berlin, 2008).
- [198] D. F. Agterberg, J. C. Séamus Davis, S. D. Ekins, E. Fradkin, D. J. Van Harlingen, S. A. Kivelson, P. A. Lee, L. Radzihovsky, J. M. Tranquada, and Y. Wang, The physics of pair density waves, *Annu. Rev. Condens. Matter Phys.* **11**, 231 (2020).
- [199] P. Fulde and R. A. Ferrell, Superconductivity in a strong spin-exchange field, *Phys. Rev.* **135**, A550 (1964).
- [200] A. I. Larkin and Yu. N. Ovchinnikov, Nonuniform state of superconductors, *Zh. Eksp. Teor. Fiz.* **47**, 1136 (1964) [*Sov. Phys. JETP* **20**, 762 (1965)].
- [201] L. Fu, C. L. Kane, and E. J. Mele, Topological Insulators in Three Dimensions, *Phys. Rev. Lett.* **98**, 106803 (2007).
- [202] Z. Ringel, Y. E. Kraus, and A. Stern, Strong side of weak topological insulators, *Phys. Rev. B* **86**, 045102 (2012).
- [203] S. Murakami, Phase transition between the quantum spin Hall and insulator phases in 3D: emergence of a topological gapless phase, *New J. Phys.* **9**, 356 (2007).
- [204] D. V. Chichinadze and A. V. Chubukov, Winding numbers of nodal points in Fe-based superconductors, *Phys. Rev. B* **97**, 094501 (2018).
- [205] T. Nakayama, T. Shishidou, and D. F. Agterberg, Nodal topology in *d*-wave superconducting monolayer FeSe, *Phys. Rev. B* **98**, 214503 (2018).
- [206] A. H. Castro Neto, F. Guinea, N. M. R. Peres, K. S. Novoselov, and A. K. Geim, The electronic properties of graphene, *Rev. Mod. Phys.* **81**, 109 (2009).
- [207] P. Kotetes, *Topological Insulators* (Morgan & Claypool, San Rafael, CA, 2019).
- [208] M. Sato, Y. Tanaka, K. Yada, and T. Yokoyama, Topology of Andreev bound states with flat dispersion, *Phys. Rev. B* **83**, 224511 (2011).
- [209] Y. X. Zhao, and Z. D. Wang, Topological Classification and Stability of Fermi Surfaces, *Phys. Rev. Lett.* **110**, 240404 (2013); Topological connection between the stability of Fermi surfaces and topological insulators and superconductors, *Phys. Rev. B* **89**, 075111 (2014).
- [210] S. Matsuura, P.-Y. Chang, A. P. Schnyder, and S. Ryu, Protected boundary states in gapless topological phases, *New J. Phys.* **15**, 065001 (2013).
- [211] M. Sato, Topological odd-parity superconductors, *Phys. Rev. B* **81**, 220504(R) (2010).
- [212] Y. Tanaka, T. Yokoyama, and N. Nagaosa, Manipulation of the Majorana Fermion, Andreev Reflection, and Josephson Current on Topological Insulators, *Phys. Rev. Lett.* **103**, 107002 (2009).
- [213] J. Linder, Y. Tanaka, T. Yokoyama, A. Sudbø, and N. Nagaosa, Unconventional Superconductivity on a Topological Insulator, *Phys. Rev. Lett.* **104**, 067001 (2010).
- [214] J. Röntynen and T. Ojanen, Topological Superconductivity and High Chern Numbers in 2D Ferromagnetic Shiba Lattices, *Phys. Rev. Lett.* **114**, 236803 (2015).
- [215] J. Li, T. Neupert, Z.-J. Wang, A. H. MacDonald, A. Yazdani, and B. A. Bernevig, A novel platform for two-dimensional chiral topological superconductivity, *Nat. Commun.* **7**, 12297 (2016).
- [216] J. L. Lado and M. Sigrist, Two-Dimensional Topological Superconductivity with Antiferromagnetic Insulators, *Phys. Rev. Lett.* **121**, 037002 (2018).
- [217] X.-L. Qi, T. L. Hughes, and S.-C. Zhang, Fermi surface topological invariants for time reversal invariant superconductors, *Phys. Rev. B* **81**, 134508 (2010).
- [218] J. C. Budich and E. Ardonne, Topological invariant for generic 1D time reversal symmetric superconductors in class DIII, *Phys. Rev. B* **88**, 134523 (2013).
- [219] C. L. M. Wong and K. T. Law, Majorana Kramers doublets in  $d_{x^2-y^2}$ -wave superconductors with rashba spin-orbit coupling, *Phys. Rev. B* **86**, 184516 (2012).
- [220] L. Fu, and C. L. Kane, Time reversal polarization and a  $Z_2$  adiabatic spin pump, *Phys. Rev. B* **74**, 195312 (2006).
- [221] M. J. A. Jardine, J. P. T. Stenger, Y. Jiang, E. J. de Jong, W. Wang, A. C. Bleszynski Jayich, and S. M. Frolov, Integrating micromagnets and hybrid nanowires for topological quantum computing, *SciPost Phys.* **11**, 090 (2021).

- [222] I. Dzyaloshinskii, A thermodynamic theory of weak ferromagnetism of antiferromagnetics, *J. Phys. Chem. Solids* **4**, 241 (1958); T. Moriya, Anisotropic superexchange interaction and weak ferromagnetism, *Phys. Rev.* **120**, 91 (1960).
- [223] N. Bogdanov and D. A. Yablonskii, Thermodynamically stable “vortices” in magnetically ordered crystals. the mixed state of magnets, *Zh. Eksp. Teor. Fiz.* **95**, 178 (1989) [*Sov. Phys. JETP* **68**, 101 (1989)].
- [224] A. Bogdanov and A. Hubert, Thermodynamically stable magnetic vortex states in magnetic crystals, *J. Magn. Magn. Mater.* **138**, 255 (1994).
- [225] N. Nagaosa and Y. Tokura, Topological properties and dynamics of magnetic skyrmions. *Nat. Nanotechnol.* **8**, 899 (2013).
- [226] A. N. Bogdanov and C. Panagopoulos, Physical foundations and basic properties of magnetic skyrmions, *Nat. Rev. Phys.* **2**, 492 (2020).
- [227] S. Mühlbauer, B. Binz, F. Jonietz, C. Pfleiderer, A. Rosch, A. Neubauer, R. Georgii, and P. Böni, Skyrmion lattice in a chiral magnet, *Science* **323**, 915 (2009).
- [228] X. Z. Yu, Y. Onose, N. Kanazawa, J. H. Park, J. H. Han, Y. Matsui, N. Nagaosa, and Y. Tokura, Real-space observation of a two-dimensional skyrmion crystal, *Nature (London)* **465**, 901 (2010); X. Z. Yu, N. Kanazawa, Y. Onose, K. Kimoto, W. Z. Zhang, S. Ishiwata, Y. Matsui, and Y. Tokura, Near room-temperature formation of a skyrmion crystal in thin-films of the helimagnet FeGe, *Nat. Mater.* **10**, 106 (2011).
- [229] S. Heinze, K. von Bergmann, M. Menzel, J. Brede, A. Kubetzka, R. Wiesendanger, G. Bihlmayer, and S. Blügel, Spontaneous atomic-scale magnetic skyrmion lattice in two dimensions, *Nat. Phys.* **7**, 713 (2011).
- [230] A. Soumyanarayanan, M. Raju, A. L. Gonzalez Oyarce, A. K. C. Tan, M.-Y. Im, A. P. Petrović, P. Ho, K. H. Khoo, M. Tran, C. K. Gan, F. Ernult, and C. Panagopoulos, Tunable room-temperature magnetic skyrmions in Ir/Fe/Co/Pt multilayers, *Nat. Mater.* **16**, 898 (2017).
- [231] M. Hervé, B. Dupé, R. Lopes, M. Böttcher, M. D. Martins, T. Balashov, L. Gerhard, J. Sinova, and W. Wulfhekkel, Stabilizing spin spirals and isolated skyrmions at low magnetic field exploiting vanishing magnetic anisotropy, *Nat. Commun.* **9**, 2198 (2018).
- [232] J. Spethmann, S. Meyer, K. von Bergmann, R. Wiesendanger, S. Heinze, and A. Kubetzka, Discovery of Magnetic Single- and Triple- $q$  States in Mn/Re(0001), *Phys. Rev. Lett.* **124**, 227203 (2020).
- [233] U. K. Rössler, A. N. Bogdanov, and C. Pfleiderer, Spontaneous skyrmion ground states in magnetic metals *Nature (London)* **442**, 797 (2006).
- [234] T. Okubo, S. Chung, and H. Kawamura, Multiple- $q$  States and Skyrmion Lattice of the Triangular-Lattice Heisenberg Antiferromagnet Under Magnetic Fields, *Phys. Rev. Lett.* **108**, 017206 (2012); T. Shimokawa, T. Okubo, and H. Kawamura, Multiple- $q$  states of the J1-J2 classical honeycomb-lattice Heisenberg antiferromagnet under magnetic fields, *Phys. Rev. B* **100**, 224404 (2019).
- [235] A. O. Leonov and M. Mostovoy, Multiply periodic states and isolated skyrmions in an anisotropic frustrated magnet, *Nat. Commun.* **6**, 8275 (2015).
- [236] M. A. Ruderman and C. Kittel, Indirect exchange coupling of nuclear magnetic moments by conduction electrons, *Phys. Rev.* **96**, 99 (1954); T. Kasuya, A Theory of metallic ferro- and antiferromagnetism on zener’s model, *Prog. Theor. Phys.* **16**, 45 (1956); K. Yosida, Magnetic properties of Cu-Mn alloys, *Phys. Rev.* **106**, 893 (1957).
- [237] I. Martin and C. D. Batista, Itinerant Electron-Driven Chiral Magnetic Ordering and Spontaneous Quantum Hall Effect in Triangular Lattice Models, *Phys. Rev. Lett.* **101**, 156402 (2008).
- [238] M. Azhar and M. Mostovoy, Incommensurate Spiral Order from Double-Exchange Interactions, *Phys. Rev. Lett.* **118**, 027203 (2017).
- [239] S. Hayami, R. Ozawa, and Y. Motome, Effective bilinear-biquadratic model for noncoplanar ordering in itinerant magnets, *Phys. Rev. B* **95**, 224424 (2017); **98**, 019903 (2018).
- [240] S. Hayami and Y. Motome, Topological spin crystals by itinerant frustration, *J. Phys.: Condens. Matter* **33**, 443001 (2021).
- [241] J. Neuhaus-Steinmetz, E. Y. Vedmedenko, T. Posske, and R. Wiesendanger, Complex magnetic ground states and topological electronic phases of atomic spin chains on superconductors, *arXiv:2109.13140*.
- [242] M. Sigrist and K. Ueda, Phenomenological theory of unconventional superconductivity, *Rev. Mod. Phys.* **63**, 239 (1991).
- [243] B. van Heck, S. Mi, and A. R. Akhmerov, Single fermion manipulation via superconducting phase differences in multiterminal Josephson junctions, *Phys. Rev. B* **90**, 155450 (2014).
- [244] T. Yokoyama and Y. V. Nazarov, Singularities of andreev spectrum in multi-terminal josephson junction, *Phys. Rev. B* **92**, 155437 (2015).
- [245] E. Strambini, S. D’Ambrosio, F. Vischi, F. S. Bergeret, Yu. V. Nazarov, and F. Giazotto, The  $\omega$ -SQUIPT: Phase-engineering of Josephson topological materials, *Nat. Nanotechnol.* **11**, 1055 (2016).
- [246] R.-P. Riwar, M. Houzet, J. S. Meyer, and Y. V. Nazarov, Multi-terminal Josephson junctions as topological materials, *Nat. Commun.* **7**, 11167 (2016).
- [247] E. Eriksson, R.-P. Riwar, M. Houzet, J. S. Meyer, and Y. V. Nazarov, Topological transconductance quantization in a four-terminal Josephson junction, *Phys. Rev. B* **95**, 075417 (2017).
- [248] J. S. Meyer and M. Houzet, Non-trivial Chern numbers in three-terminal Josephson junctions, *Phys. Rev. Lett.* **119**, 136807 (2017).
- [249] H. Y. Xie, M. G. Vavilov, and A. Levchenko, Topological Andreev bands in three-terminal Josephson junctions, *Phys. Rev. B* **96**, 161406 (2017).
- [250] M. Houzet and J. S. Meyer, Majorana-Weyl crossings in topological multiterminal junctions, *Phys. Rev. B* **100**, 014521 (2019).
- [251] H.-Y. Xie and A. Levchenko, Topological supercurrents interaction and fluctuations in the multiterminal Josephson effect, *Phys. Rev. B* **99**, 094519 (2019).
- [252] L. P. Gavensky, G. Usaj, and C. A. Balseiro, Topological phase diagram of a three-terminal Josephson junction: From the conventional to the Majorana regime, *Phys. Rev. B* **100**, 014514 (2019).
- [253] P. Kotetes, M. T. Mercaldo, and M. Cuoco, Synthetic Weyl Points and Chiral Anomaly in Majorana Devices with Non-standard Andreev-Bound-State Spectra, *Phys. Rev. Lett.* **123**, 126802 (2019).

- [254] M. T. Mercaldo, P. Kotetes, and M. Cuoco, Magnetoelectrically-tunable andreev-bound-state spectra and spin polarization in P-wave josephson junctions, *Phys. Rev. B* **100**, 104519 (2019).
- [255] K. Sakurai, M. T. Mercaldo, S. Kobayashi, A. Yamakage, S. Ikegaya, T. Habe, P. Kotetes, M. Cuoco, and Y. Asano, Nodal Andreev spectra in multi-majorana three-terminal josephson junctions, *Phys. Rev. B* **101**, 174506 (2020).
- [256] J. S. Meyer and M. Houzet, Conductance quantization in topological Josephson trijunctions, *Phys. Rev. B* **103**, 174504 (2021).
- [257] H. Weisbrich, R. L. Klees, G. Rastelli, and W. Belzig, Second Chern number and non-Abelian Berry phase in topological superconducting systems, *PRX Quantum* **2**, 010310 (2021); R. L. Klees, J. C. Cuevas, W. Belzig, and G. Rastelli, Ground-state quantum geometry in superconductor-quantum dot chains, *Phys. Rev. B* **103**, 014516 (2021).
- [258] N. Pankratova, H. Lee, R. Kuzmin, M. Vavilov, K. Wickramasinghe, W. Mayer, J. Yuan, J. Shabani, and V. E. Manucharyan, Multiterminal Josephson Effect, *Phys. Rev. X* **10**, 031051 (2020).
- [259] Y. Gallais and I. Paul, Charge nematicity and electronic Raman scattering in iron-based superconductors, *C. R. Phys.* **17**, 113 (2016); A. Kreisel, P. J. Hirschfeld, and B. M. Andersen, On the remarkable superconductivity of FeSe and its close cousins, *Symmetry* **12**, 1402 (2020).
- [260] A. A. Burkov, Weyl metals, *Annu. Rev. Condens. Matter Phys.* **9**, 359 (2018).
- [261] C. Fang, H. Weng, X. Dai, and Z. Fang, Topological nodal line semimetals, *Chin. Phys. B* **25**, 117106 (2016).
- [262] K. T. Law, P. A. Lee, and T. K. Ng, Majorana Fermion Induced Resonant Andreev Reflection, *Phys. Rev. Lett.* **103**, 237001 (2009).
- [263] J. D. Sau, S. Tewari, R. Lutchyn, T. Stanescu, and S. Das Sarma, Non-Abelian quantum order in spin-orbit-coupled semiconductors: The search for topological Majorana particles in solid state systems, *Phys. Rev. B* **82**, 214509 (2010).
- [264] K. Flensberg, Tunneling characteristic of a chain of Majorana bound states, *Phys. Rev. B* **82**, 180516(R) (2010).
- [265] J. J. He, T. K. Ng, P. A. Lee, and K. T. Law, Selective Equal-Spin Andreev Reflections Induced by Majorana Fermions, *Phys. Rev. Lett.* **112**, 037001 (2014).
- [266] P. Kotetes, D. Mendler, A. Heimes, and G. Schön, Majorana fermion fingerprints in spin-polarised scanning tunneling microscopy, *Phys. E* **74**, 614 (2015).
- [267] D. Sticlet, C. Bena, and P. Simon, Spin and Majorana Polarization in Topological Superconducting Wires, *Phys. Rev. Lett.* **108**, 096802 (2012).
- [268] T. Mizushima, M. Sato, and K. Machida, Symmetry Protected Topological Order and Spin Susceptibility in Superfluid  $^3\text{He-B}$ , *Phys. Rev. Lett.* **109**, 165301 (2012).
- [269] Z. Wang, X.-L. Qi, and S.-C. Zhang, Topological field theory and thermal responses of interacting topological superconductors, *Phys. Rev. B* **84**, 014527 (2011).
- [270] S. Ryu, J. E. Moore, and A. W. W. Ludwig, Electromagnetic and gravitational responses and anomalies in topological insulators and superconductors, *Phys. Rev. B* **85**, 045104 (2012).
- [271] A. Furusaki, N. Nagaosa, K. Nomura, S. Ryu, and T. Takayanagi, Electromagnetic and thermal responses in topological matter: Topological terms, quantum anomalies and D-branes, *C. R. Phys.* **14**, 871 (2013).
- [272] D. Bulmash, P. Hosur, S.-C. Zhang, and X.-L. Qi, Unified Topological Response Theory For Gapped and Gapless Free Fermions, *Phys. Rev. X* **5**, 021018 (2015).
- [273] Y. Imai, K. Wakabayashi, and M. Sgrist, Thermal Hall conductivity in the spin-triplet superconductor with broken time-reversal symmetry, *Phys. Rev. B* **95**, 024516 (2017).
- [274] S. M. Young and C. L. Kane, Dirac Semimetals in Two Dimensions, *Phys. Rev. Lett.* **115**, 126803 (2015).
- [275] Y. X. Zhao and A. P. Schnyder, Nonsymmorphic symmetry-required band crossings in topological semimetals, *Phys. Rev. B* **94**, 195109 (2016).
- [276] C. Fang, Y. Chen, H.-Y. Kee, and L. Fu, Topological nodal line semimetals with and without spin-orbital coupling, *Phys. Rev. B* **92**, 081201 (2015).
- [277] B.-J. Yang, T. A. Bojesen, T. Morimoto, and A. Furusaki, Topological semimetals protected by off-centered symmetries in nonsymmorphic crystals, *Phys. Rev. B* **95**, 075135 (2017).
- [278] J. Zhang, Y.-H. Chan, C.-K. Chiu, M. G. Vergniory, L. M. Schoop, and A. P. Schnyder, Topological band crossings in hexagonal materials, *Phys. Rev. Mater.* **2**, 074201 (2018).
- [279] M. Malard, P. E. de Brito, S. Östlund, and H. Johannesson, Movable but not removable band degeneracies in a symmmorphic crystal, *Phys. Rev. B* **98**, 165127 (2018).